FEDERAL UNIVERSITY OF UBERLANDIA

FACULTY OF CHEMICAL ENGINEERING

GRADUATE PROGRAM IN CHEMICAL ENGINEERING

NAIARA DA COSTA TELIS

EVALUATING NIOBIA-SUPPORTED NI-FE CATALYST FOR HYDRODEOXYGENATION (HDO) OF LIGNIN-DERIVED PYROLYSIS OILS.

UBERLÂNDIA – MINAS GERAIS

2025

NAIARA DA COSTA TELIS

EVALUATING NIOBIA-SUPPORTED NI-FE CATALYST FOR HYDRODEOXYGENATION (HDO) OF LIGNIN-DERIVED PYROLYSIS OILS.

Thesis presented to the Federal University of Uberlandia as part of the requirements of the Graduate Program in Chemical Engineering for obtaining the degree *Doctor Scientiae*.

Advisor: Prof. Dr. Ricardo Reis Soares

UBERLÂNIDA – MINAS GERAIS

2025

Ficha Catalográfica Online do Sistema de Bibliotecas da UFU
com dados informados pelo(a) próprio(a) autor(a).

T272
2025

Telis, Naiara da Costa, 1989-
Evaluating Niobia-Supported Ni-Fe Catalyst for Hydrodeoxygenation (HDO) of lignin-derived pyrolysis oils. [recurso eletrônico] / Naiara da Costa Telis. - 2025.

Orientador: Ricardo Reis Soares.
Tese (Doutorado) - Universidade Federal de Uberlândia, Pós-graduação em Engenharia Química.
Modo de acesso: Internet.
Disponível em: http://doi.org/10.14393/ufu.te.2025.249
Inclui bibliografia.

1. Engenharia química. I. Soares, Ricardo Reis,1965-, (Orient.). II. Universidade Federal de Uberlândia. Pós-graduação em Engenharia Química. III. Título.

CDU: 66.0

Bibliotecários responsáveis pela estrutura de acordo com o AACR2:

Gizele Cristine Nunes do Couto - CRB6/2091
Nelson Marcos Ferreira - CRB6/3074

UNIVERSIDADE FEDERAL DE UBERLÂNDIA
Coordenação do Programa de Pós-Graduação em Engenharia Química
Av. João Naves de Ávila, 2121, Bloco 1K, Sala 206 - Bairro Santa Mônica, Uberlândia-MG, CEP 38400-902
Telefone: (34)3239-4249 - www.ppgeq.feq.ufu.br - secppgeq@feq.ufu.br

ATA DE DEFESA - PÓS-GRADUAÇÃO

Programa de Pós-graduação em:	Engenharia Química				
Defesa de:	Tese de Doutorado, 5/2025, PPGEQ				
Data:	27 de março de 2025	Hora de início:	8:30	Hora de encerramento:	12:15
Matrícula da Discente:	12013EQU007				
Nome da Discente:	Naiara da Costa Telis				
Título do Trabalho:	Evaluating Niobia-Supported Ni-Fe Catalyst for Hydrodeoxygenation (HDO) of lignin-derived pyrolysis oils				
Área de concentração:	Desenvolvimento de Processos Químicos				
Linha de pesquisa:	Termodinâmica, cinética química e reatores				
Projeto de Pesquisa de vinculação:	CNPq Nº 12/2020- Programa MAI-DAI: Estudo de Processo Catalítico de Hidro-Desoxigenação (HDO) de Moléculas oriundas da Pirólise de Resíduos de Pinus e/ou Eucalipto				
ODS-ONU:	ODS 7 – Energia Limpa e Acessível, ODS 9 – Indústria, Inovação e Infraestrutura e ODS 13 – Ação contra a mudança global do clima				

Reuniu-se por meio de webconferência, a Banca Examinadora designada pelo Colegiado do Programa de Pós-graduação em Engenharia Química, assim composta: Doutores: Klaus Raffelt - KIT/Alemanha e Fabio Bellot Noronha - DICAP/INT, e Professores Doutores: Osmando Ferreira Lopes - IQ/UFU, Luis

Claudio Oliveira Lopes - PPGEQ/UFU e Ricardo Reis Soares - PPGEQ/UFU, orientador da candidata.

Iniciando os trabalhos o presidente da mesa, Prof. Dr. Ricardo Reis Soares, apresentou a Comissão Examinadora e a candidata, agradeceu a presença do público, e concedeu à discente a palavra para a exposição do seu trabalho. A duração da apresentação da discente e o tempo de arguição e resposta foram conforme as normas do Programa.

A seguir, o presidente concedeu a palavra, pela ordem sucessivamente aos examinadores, que passaram a arguir a candidata. Ultimada a arguição, que se desenvolveu dentro dos termos regimentais, a Banca, em sessão secreta, atribuiu o resultado final considerando a candidata:

Aprovada

Esta defesa faz parte dos requisitos necessários à obtenção do título de Doutor.

O competente diploma será expedido após cumprimento dos demais requisitos, conforme as normas do Programa, a legislação pertinente e a regulamentação interna da UFU.

Nada mais havendo a tratar foram encerrados os trabalhos. Foi lavrada a presente ata que após lida e achada conforme foi assinada pela Banca Examinadora.

Documento assinado eletronicamente por **Ricardo Reis Soares**, **Professor(a) do Magistério Superior**, em 31/03/2025, às 09:40, conforme horário oficial de Brasília, com fundamento no art. 6º, § 1º, do Decreto nº 8.539, de 8 de outubro de 2015.

Documento assinado eletronicamente por **Osmando Ferreira Lopes**, **Professor(a) do Magistério Superior**, em 31/03/2025, às 10:03, conforme horário oficial de Brasília, com fundamento no art. 6º, § 1º, do Decreto nº 8.539, de 8 de outubro de 2015.

Documento assinado eletronicamente por **Luis Claudio Oliveira Lopes**, **Professor(a) do Magistério Superior**, em 31/03/2025, às 11:02, conforme horário oficial de Brasília, com fundamento no art. 6º, § 1º, do Decreto nº 8.539, de 8 de outubro de 2015.

Documento assinado eletronicamente por **Klaus Raffelt**, **Usuário Externo**, em 02/04/2025, às 07:40, conforme horário oficial de Brasília, com fundamento no art. 6º, § 1º, do Decreto nº 8.539, de 8 de outubro de 2015.

Documento assinado eletronicamente por **Fabio Bellot Noronha**, **Usuário Externo**, em 10/04/2025, às 03:29, conforme horário oficial de Brasília, com fundamento no art. 6º, § 1º, do Decreto nº 8.539, de 8 de outubro de 2015.

A autenticidade deste documento pode ser conferida no site https://www.sei.ufu.br/sei/controlador_externo.php?acao=documento_conferir&id_orgao_acesso_externo=0, informando o código verificador **6210734** e o código CRC **1A5E663E**.

ACKNOWLEDGMENTS

First and foremost, I would like to thank God for granting me health, life, and the strength to reach this moment.

I am deeply grateful to my husband, Gerardo Telis, for being the best companion throughout these years. Your unconditional friendship and love have made me stronger. This achievement is yours as well.

I extend my gratitude to my mother, Brigitti, for giving me life and for all the teachings and dedication she has given me. Your life is a source of inspiration to me. To my sister, Naiane, for her unwavering friendship and constant encouragement, ensuring that I never gave up. To my nephew, Will, who, despite being so young, already gives me strength. Your smile brightens my days. To my brother-in-law, for taking such good care of them when I am not around.

I am thankful for all my childhood friends, who, despite the distance, never failed to support me. Always understanding, they sent me positive energy throughout these years.

I am also grateful to the friends I made in Uberlandia, MG, especially those from the gym and CrossFit. You played an important role in making my days more enjoyable and helping me become stronger every day.

To all my friends from the GPCATT laboratory, especially Ivan Pedro Arêdes, Rondinele Alberto dos Reis Ferreira, Hídila Souza Teixeira da Silva, Diogo Pimentel de Sá da Silva, Ana Laura Medeiros, Ana Gabriela, and Gabriel Garcia—thank you for always standing by my side, sharing countless moments of joy and laughter. Your friendship made me stronger and made this journey lighter.

I extend my gratitude to all the technicians and staff at UFU, especially my dear friend José Henrique Faleiro, the "glassblower." Your friendship was essential in keeping me from giving up, both inside and outside of UFU.

I am grateful to all UFU professors for their dedication and the invaluable knowledge they shared with me over the past four years.

A special thanks to my advisor and now friend, Dr. Ricardo Reis Soares, for his wise guidance, patience, and continuous support throughout this journey. Your dedication was fundamental to the completion of this work. Thank you for trusting me and believing in my potential.

I also appreciate the friends I made during my international research stay at KIT, Germany. With you, I learned much more than catalysis—I learned patience and resilience. A special thank you to my friend Klaus, also known as "Claudinho," who trusted me, was patient, and provided me with an incredible experience at KIT. To Frederico and Ana, thank you for the many joyful moments and laughter.

I am grateful to the Karlsruhe Institute of Technology (KIT) and Professor Nicolaus Dahmen for welcoming me and allowing me to carry out my research exchange.

I acknowledge the financial support from CNPq (MAI-DAI Program), KLABIN (Mr. Rodrigo Oliveira), DAAD, and Brisk2.

Lastly, I thank CAPES for the Graduate Program infrastructure and Pamela, Lana, Benjamin, Ayr, Celio, and Thomas Zevaco for their technical assistance services.

ABSTRACT

TELIS, Naiara da Costa, D.Sc., Federal University of Uberlandia, March 2025. **Evaluating Niobia-Supported Ni-Fe Catalyst for Hydrodeoxygenation (HDO) of Lignin-Derived Pyrolysis Oils.** Advisor: Ricardo Reis Soares.

Hydrodeoxygenation (HDO) of lignin-derived pyrolysis oils presents a promising pathway for producing renewable, low-carbon liquid fuels. This thesis evaluates the performance of niobium oxide (Nb_2O_5)-supported catalysts in both batch and continuous HDO processes, comparing them with silica-supported catalysts to assess the role of the support in catalytic performance. The study focused on Ni-Fe bimetallic catalysts, investigating the interaction between the two metals and the support to optimize deoxygenation efficiency. In the batch HDO of guaiacol, the 5Ni1Fe/Nb_2O_5 catalyst exhibited the best performance, achieving high selectivity towards cyclohexanol and cyclohexane, emphasizing the synergistic effect between Ni and Fe and the role of Nb_2O_5 acidity in promoting hydrogenation and deoxygenation. In contrast, the 5Ru/Nb_2O_5 catalyst showed the highest conversion rate (55%), but with a preference for hydrogenation rather than complete deoxygenation. For bio-oil HDO, the 5Ni5Fe/Nb_2O_5 catalyst emerged as the most effective, demonstrating moderate hydrogen consumption, low CO_2 production, and efficient deoxygenation. Its ability to balance oxygen removal while retaining carbon makes it a strong candidate for practical bio-oil upgrading. In the continuous reactor HDO tests, the 5Ni1Fe/Nb_2O_5 and 5Ru/Nb_2O_5 catalysts were synthesized using Nb_2O_5 in pellet form to enhance mechanical stability for scale-up. Both catalysts exhibited a tendency toward hydrogenation, with 5Ni1Fe/Nb_2O_5 confirming its superior performance in deoxygenation, validating findings from batch studies and reinforcing its potential for industrial application in sustainable biofuel production.

Keywords: Hydrodeoxygenation, Lignin-derived Pyrolysis Oils, Niobium Oxide (Nb_2O_5) Supported Catalysts, Batch and Continuous Processes, Guaiacol, Bio-oil, Ni-Fe Bimetallic Catalysts, Ru/Nb2O5 Catalyst, Carbon Efficiency, Industrial Application

LIST OF FIGURES

LIST OF TABLES

SUMMARY

CHAPTER 1

INTRODUCTION

The increasing demand for energy, driven by global population growth and improvements in living standards, has long been met by burning fossil fuels, leading to the alarming release of greenhouse gases such as carbon dioxide (CO_2), sulfur dioxide (SO_2), and nitrogen oxides (NO_x). These emissions contribute to phenomena like the greenhouse effect, triggering an increase in planetary temperature that threatens both global ecosystems and human survival [1,2].

Unlike fossil fuels, the combustion of biomass can be considered carbon-neutral since the CO_2 emitted was initially absorbed during plant growth, thereby providing a more sustainable alternative with significantly lower emissions of NO_x and SO_2. Biomass, particularly lignocellulosic materials like agricultural residues, wood waste, bagasse, rice husk, and forest debris, offers a viable source of alternative energy, especially for challenging sectors such as transportation fuels [3]. This not only provides an alternative to traditional fuels but also empowers farming communities by offering a secondary source of income and reducing the customary burning of agricultural waste [4].

Among the thermochemical conversion methods for biomass, fast pyrolysis is widely recognized for its efficiency in producing bio-oil, a liquid fuel that retains significant energy content. Pyrolysis, carried out at temperatures between 400 and 800 °C in an inert atmosphere, generates solid, liquid, and gaseous products. However, the resulting bio-oil presents high oxygen and water content, as well as elevated acidity and viscosity, which lead to instability and reduce its heating value to nearly half that of conventional fuels [5,6]. These properties limit its direct application as a transportation fuel. Therefore, upgrading processes that remove oxygen and separate water are essential to improve bio-oil quality and enable its integration into existing refinery infrastructure [7].

A promising approach in processing bio-oil is the use of catalytic hydrotreating technology, also known as hydrodeoxygenation (HDO). In this method, bio-oil constituents undergo decarboxylation, decarbonylation, cracking, and hydrogenation processes, resulting in an increased hydrocarbon content [7]. In the case of bio-oil derived from fast pyrolysis of plant biomass, about 40% of the content consists of phenolics and their derivatives, which function as building blocks derived from lignin. Among these components, guaiacol is identified as a representative example for the evaluation of catalysts in hydrodeoxygenation (HDO), due to the presence of two types of C-O bonds in its structure (hydroxyl and methoxy), representing key functional groups in pyrolysis-derived phenolics [8,9].

The hydrodeoxygenation (HDO) reaction typically proceeds through three main pathways: (i) hydrogenation followed by C–O bond cleavage (HYD), (ii) direct deoxygenation (DDO) via hydrogenolysis, and (iii) tautomerization followed by hydrogenation or dehydration, depending on the substrate and catalyst properties [10–12]. The selection of an appropriate catalyst is important for improving HDO efficiency. Conventional HDO catalysts include sulfided Mo-based materials ($NiMo/Al_2O_3$, $CoMo/Al_2O_3$), noble metals (Rh, Ru, Pt, Pd), and transition metal oxides (Ni, Co, Fe). Sulfide-based catalysts have shown loss of sulfur from metallic sulfides and phase changes from metallic oxides resulting in low HDO activity. Catalysts based on noble metals exhibit excellent catalytic activities; however, their high cost limits their use for commercial purposes. In this context, catalysts based on transition metals emerge as a competitive option for application in HDO reactions [13,14].

Considering that the HDO process is a predominantly combination of hydrogenation and deoxygenation reactions, these processes preferably require a bifunctional catalyst that has active metal sites for hydrogenation and an acid function for deoxygenation through dehydration. Researchers observed that the synergism between Lewis acid sites and metal nanoparticles is the primary factor to potentiate catalyst activity in two-step hydrogenolysis of phenolic compounds [15,16]. Bimetallic catalysts have gained attention due to synergistic effects between two metals, leading to improved hydrogenation and C–O bond cleavage properties. In particular, Ni-Fe catalysts have been reported to enhance HDO selectivity, as Fe can modify the electronic structure of Ni, improving catalytic activity and stability [17–28]

The choice of catalyst support is crucial in HDO performance, as it influences metal dispersion, stability, and acid-base properties. Niobium pentoxide (Nb_2O_5) has gained attention as an efficient support due to its oxophilic nature, Lewis acidity, and ability to promote selective deoxygenation reactions [29]. Mäkelä et al. (2020) [30] reported that the oxophilic strength of active sites in Nb_2O_5 and TiO_2 supports was significantly higher than that of ZrO_2. Previous studies conducted by our group [31–33] further demonstrated that the incorporation of Nb into catalysts enhanced phenol yield, whereas Pt/Al_2O_3 predominantly produced catechol. This effect was attributed to the interaction between Pt and NbOx species, which likely generated oxophilic sites that promoted the direct deoxygenation (DDO) pathway, leading to phenol formation while minimizing catalyst deactivation, even under low hydrogen conditions. This finding underscores the beneficial synergy between niobia and platinum in HDO reactions [32].

In this sense, the main objective of this work was to investigate the catalytic performance of Ni-Fe catalysts supported on niobium pentoxide (Nb_2O_5) in the hydrodeoxygenation (HDO) process of guaiacol and bio-oil in the liquid phase. This study aims to understand how metal interactions and support properties influence the selectivity and efficiency of oxygen removal. The research involves the synthesis and characterization of Ni-Fe/Nb_2O_5 catalysts to assess their structural and physicochemical properties, followed by an evaluation of their catalytic performance in the HDO of guaiacol to understand metal interactions, support effects, and reaction pathways. Furthermore, the investigation extends to the HDO of real fast pyrolysis bio-oil to examine the scalability and industrial potential of these catalysts. Additionally, the role of Nb_2O_5 as a catalyst support is explored, highlighting its ability to enhance deoxygenation efficiency and hydrocarbon yield in liquid-phase HDO reactions.

Thesis Structure

Chapter 2: Literature Review

Chapter in which a small overview of the pyrolysis process, HDO processes and catalysts will be provided.

Chapter 3: Synthesis of Catalyst Preparation, characterization, and catalytic tests

Chapter in which the methodology used in the preparation of catalysts, methodology used in characterizations and methodology used in catalytic tests will be discussed.

Chapter 4: HDO of Guaiacol

Chapter in which the HDO process of guaiacol will be discussed.

Chapter 5: HDO in Liquid Phase

Chapter in which the HDO process in the liquid phase of Fast Pyrolysis Bio-oil will be discussed.

Chapter 6: Evaluation of Niobium-Based Performance Catalysts in a Continuous Liquid-Phase HDO

Chapter discussing the HDO process using pellet catalysts for scale-up applications.

Chapter 7: Conclusion

Chapter providing the final conclusions of this study and recommendations for future research.

CHAPTER 2

LITERATURE REVIEW

2.1. BIOMASS BIOFUELS

The increase in demand for energy as a result of population growth and technological advancement poses an environmental threat. That threat lies in global warming, which comes from excessive consumption of fossil fuels, releasing carbon dioxide (CO_2), causing acid rain and contributing to climate change. The combustion of fossil fuels is estimated to produce about 21.3 billion tons of carbon dioxide (CO_2) [34] and other greenhouse gases. In addition, research indicates that global oil reserves will be completely depleted by 2060. Given this perspective, it is crucial to foster the development of renewable sources capable of supplying energy and biofuels [35,36].

Thus, processes that involve the conversion of biomass into high-quality liquid fuels have emerged as great potential for mitigating greenhouse gas emissions, due to their almost carbon neutrality and great power to contribute to energy independence without using oil. Extensive research is underway in this area to quantify global biomass technologies [37].

It is understood that biomass is any source of heat or chemicals that are biogenic in nature and is commonly used to refer to non-fossil raw materials such as wood, animal or plant waste, and municipal waste. This potential can be converted directly into energy for cooking, heating, or generating motion and electricity, but it can also be chemically converted into biofuels, which include the following: Compressed Natural Gas (CNG), Bio gasoline, biobutanol, Hydrotreated Vegetable Oil (HVO), Fatty Acid Methyl Ester (FAME), methanol, isobutanol, hydrogen, and Syngas among others [4,38,39].

In 2022, biofuels from biomass accounted for more than 3.5% of global energy demand in transport, predominantly in road transport. The use of biofuels has been steadily expanding, with an average growth of almost 6% per year over the last five years (Figure 1) with a temporary decline in 2020 due to the impacts of the COVID-19 pandemic. Despite advances in the use of higher production sources such as coal, oil, nuclear and hydroelectric power, biofuels maintain their relevance as a significant

energy source. According to data from the International Energy Agency (IEA), demand for biofuels increased by 6% in 2022, sustaining the recent pace of growth [40,41].

FIGURE 1. Global Demand for Biofuel in Transportation (EJ/year)

Source: International Energy Agency 2023 [42]

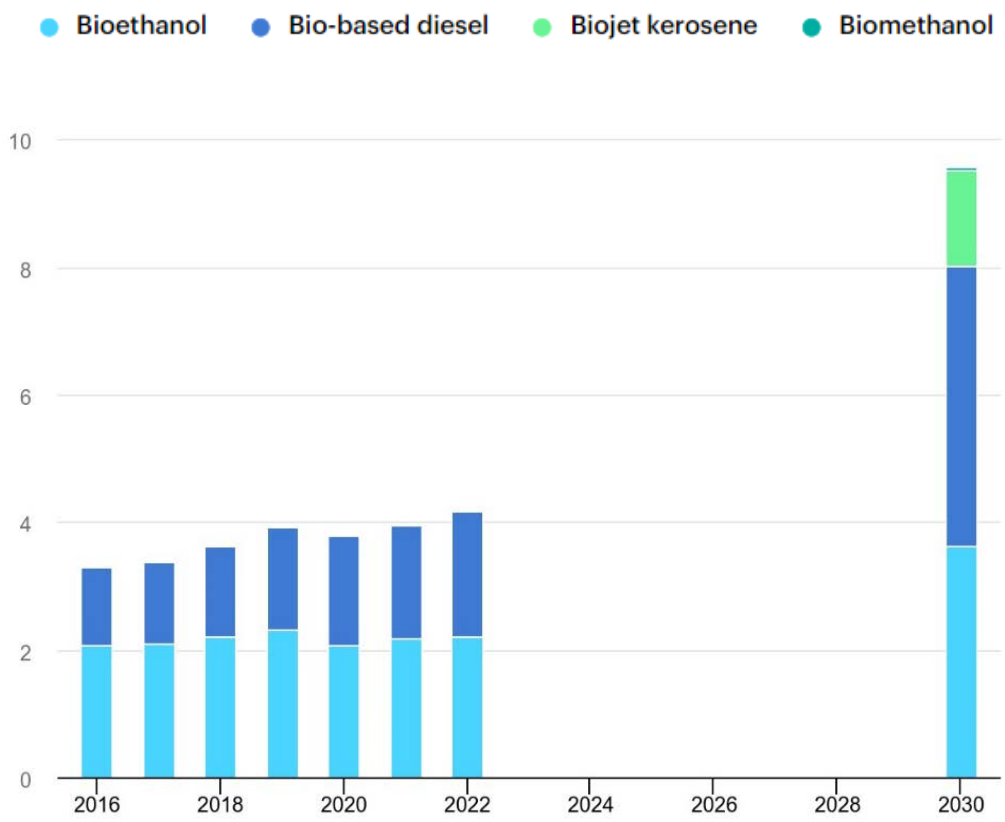

According to the latest forecast in the latest CO_2 emissions report, a critical innovation gap persists in the conversion of woody and herbaceous biomass, including agricultural and forestry residues, into liquid biofuels. Thermochemical routes such as biomass gasification, bio-FT synthesis (biomass-based Fischer-Tropsch), hydrothermal liquefaction, and fast pyrolysis with upgrade offer the potential to exploit biomass waste and waste resources that are more abundant than traditional routes by aligning with the quantities envisaged in the net-zero emissions (NZE) scenario [41].

Pyrolysis, known for its flexibility in optimizing different yields of products such as coal and liquid condensate, is considered to be one of the most robust and well-

developed technologies among them. The resulting biomass liquefaction products are energy-dense, storable, and easily transportable [43].

2.1.1. Biomass Fast Pyrolysis

Fast pyrolysis is a high-temperature procedure that heats biomass quickly and without oxygen. Therefore, its decomposition occurs, resulting mainly in vapors, aerosols, and a certain amount of coal. This method often favors the formation of net income, which can represent up to 75% of the total products. During pyrolysis, dry biomass undergoes thermal decomposition in an inert atmosphere to prevent combustion, although autothermal pyrolysis is also exploited for partial combustion. The mechanism of decomposition is complex, involving parallel and consecutive reactions at different temperatures for hemicellulose, cellulose, and lignin. The decomposition of lignocellulosic biomass during pyrolysis occurs at varying temperatures. Hemicellulose begins decomposition at the lowest temperatures (200-350 °C), producing products such as acetic acid. Cellulose undergoes decomposition at medium temperatures (300-390 °C), resulting in levoglucosan, anhydrocellulose, and other by-products. Lignin decomposes at the highest temperatures (200-450 °C) and contributes more significantly to the formation of coal compared to cellulose and hemicellulose. Pyrolysis involves a complex series of reactions, including dehydration, decarboxylation, isomerization, depolymerization, and carbonization. [1,44–46]

The presence of small particles in the biomass feedstock makes it easier to achieve a high heating rate and a short residence time. This characterizes the fast pyrolysis process. In fast pyrolysis reactors, high heating rates are employed to increase the production of condensable (liquid) components and reduce the coal yield. The efficient transport of heat within the biomass poses a challenge for the effective performance of pyrolysis, especially during fast pyrolysis, which demands high heating rates. The biomass needs to be reduced in size or ground before it is introduced into the reactor, due to its low thermal conductivity. Fast pyrolysis techniques predominantly result in the generation of bio-oil, the performance of which is linked to biomass, process temperature, gas dwell time in the reactor, mineral content, particle size, and heating rate [47–49].

Large net product yields can be recovered, often termed Fast Pyrolysis Bio-Oil (FPBO), if collected as a single product. The non-condensable gas fraction consists mainly of CO_2, CO, methane, ethane and other light hydrocarbons. The solid product includes coal with a carbon content in the range of 61-93% by weight, contributing to its high energy value [50] minimizes the water content in the liquid product, a common strategy involves the use of fractional condensation methods, in which a water-rich fraction (80-85% by weight) is often recovered at lower condensation temperatures, called an aqueous condensate, featuring a significant fraction of organic acids, leading to a product with a pH value of around 3. This condensate is formed when ash-rich materials or biomass with higher moisture content are used. [45,46,51]

2.1.2. Bio-oil

FPBO is a characteristic dark brown liquid with high viscosity and offers significant environmental advantages. It produces almost half the NO_x generated by diesel and very low amounts of SO_x. In terms of chemical composition, FPBO is a mixture of more than 300 mostly oxygenated compounds, including carboxylic acids, ketones, aldehydes, alcohols, furans, sugars, phenolics, guaiacols, water, ash components, and partially depolymerized lignin, often referred to as pyrolytic lignin [51,52].

However, its high oxygen content (28% by weight), leads to a lower and higher calorific value when compared to petroleum-based fuels, as well as a low miscibility with conventional fuels. A high viscosity reduces its pumpability and fluidity and further impairs its direct use. All these characteristics can be compared to conventional diesel and heavy fuel oil in the Table 1. Traces of ash, alkali, chlorine and sulfur may also be present in the bio-oil [44,50,53,54].

Currently, the direct application of FPBO is limited to boiler fuel for heat and power. For many other uses, an additional upgrade step is required. Other FPBO-related issues, such as changing properties over time, i.e., higher viscosity and phase separation during storage, also motivate the development and/or selection of upgrade technologies [6,45,55]. Many researchers have successfully improved the desirable characteristics of bio-oil by reducing its oxygen content through various upgrade techniques, with methods including co-pyrolysis and hydrodeoxygenation (HDO). Co-pyrolysis involves

using multiple raw materials to produce pyrolytic oil, resulting in higher yield and better quality without significant modifications to the process. This approach offers a higher calorific value and addresses environmental issues related to plastic waste disposal. On the other hand, HDO has emerged as a promising technique for turning pyrolytic oils into transportation fuels. This method represents an adaptation or extension of the conventional processes employed in oil refineries [56–58].

TABLE 1. Physicochemical properties and elemental composition of oils from wheat straw (FPBO from Biomass Technology Group, the Netherlands– BTG), diesel and heavy fuel oil.

Source: Adapted from [53,54,59]

Property	FPBO (Pine Beech wood-BTG)	Diesel	Heavy Fuel Oil
Water [wt. %]	22.3	0.0	0.1
Ash [wt. %]	0	0.0	0.1
Carbon [wt. %]	44.4	58.0	86.0
Hydrogen [wt. %]	5.2	7.2	13.0
Nitrogen [wt. %]	0.2	0.2	0.3
Oxygen [wt. %]	27.9	0.0	0.0
Brennisteinn [wt.ppm]	0.0	10.0	21.0
Stability	Unstable	Stable	Stable
Viscosity (40-50 °C) [cSt]	13.0	4.5	1.9 - 3.4
Density (15-40°C) [kg/L]	1.1	0.8	0.8
Flashpoint [°C]	50.0	65	100.0
HHV [MJ/kg]	16.6	38.0	41.0
pH	4.0	3.2	-

2.2. HYDRODEOXYGENATION (HDO)

Hydrodeoxygenation, or also known as HDO, is a chemical process used primarily in the petroleum refining industry and in the production of biofuels. This process involves removing oxygen from organic compounds, such as vegetable oils or bio-oils, through hydrogenation reactions [60].

In hydrodeoxygenation (HDO), oxygenated compounds present in bio-oils undergo processing under controlled temperature and pressure conditions in the presence of a catalyst. Hydrogen facilitates the removal of oxygen atoms, converting these compounds into refined hydrocarbons that are more suitable for high-value fuels and chemical applications. This process is essential in upgrading biofuels derived from renewable sources, enhancing their stability, energy content, and compatibility with existing fuel infrastructure [61,62].

Generally, HDO reactions take place at temperatures ranging from 250 to 450 °C. Since the reaction is exothermic and equilibrium predictions suggest that complete conversion of model compounds is possible at temperatures up to 600 °C, the choice of operating temperature should be guided primarily by reaction kinetics rather than thermodynamic limits [61].

2.2.1. HDO Molecule Model: Guaiacol

Bio-oil is a blend of diverse organic compounds, encompassing simple oxygenates such as acids, esters, alcohols, ketones, and aldehydes, as well as containing sugars, furans (such as furfural and hydroxymethylfurfural), and phenolic compounds, including phenols, guaiacols, and syringols. The complexity of this composition makes it difficult to anticipate the reaction mechanism of hydrodeoxygenation, to understand the kinetics, to identify the active sites and to establish the structure-function relationships of the catalysts. Due to this complexity, fundamental studies are being conducted using model molecules that represent the different families of compounds derived from biomass [30,63–65].

Guaiacol (2-methoxyphenol, $C_7H_8O_2$) has emerged as a particularly valuable representative of the lignin fraction in bio-oil, representing a proportion of up to 20 wt.% in bio-oils, being characterized as compounds resistant to deoxygenation. In this sense, guaiacol is recognized as a representative compound for the evaluation of HDO, thanks to the existence of two types of C-O bonds (Csp_2 OCH_3 (hydroxy) and Csp_2 OH (methoxy)) in its structure [60]. Early research with guaiacol revealed a sequence of changes that resulted in the formation of catechol, methylated derivatives and deoxygenated compounds such as benzene and cyclohexane [9,66].

The reaction mechanism of guaiacol HDO is complex, and two trajectories are commonly suggested. The first consists of hydrogenolysis of the O–CH_3 bond, which leads to the formation of catechol and methane, and the other is demethoxylation, which occurs by the cleavage of the aromatic C–OCH_3 bond, leading to phenol and methanol [67,68]. However, the reaction pathways are highly dependent on the catalyst composition and operating conditions, such as temperature and pressure. A thermodynamic equilibrium analysis of 27 commonly reported guaiacol HDO reactions in the gas phase identified the most stable pathways, highlighting bimolecular transalkylation (TRA) as the dominant route at 573 K, forming anisole and catechol. Additionally, the demethylation (DME) and direct deoxygenation (DDO) pathways exhibited higher equilibrium constant values than the demethoxylation (BMD) route, indicating a preference for methane over methanol formation, the latter being susceptible to decomposition into CO and H_2 [31]

Experimental studies have provided valuable insights into how different catalysts influence the reaction pathways of guaiacol HDO. Gao et al. (2015) [69] investigated Pt supported on activated carbon, proposing a reaction network that identified cyclopentanone as an intermediate and confirming that the reaction kinetics followed a power-law model. Silva et al. (2020) [70] examined Pt/Nb_2O_5-Al_2O_3 catalysts and demonstrated that increasing niobia loading enhanced phenol selectivity due to the formation of oxophilic NbOx species. These species facilitated direct deoxygenation (DDO), reduced catalyst deactivation, and improved overall oxygen removal. Similarly, Xu et al. (2022) [71] highlighted the role of Nb_2O_5 modification in CoMoS/Nb_2O_5-Al_2O_3, showing that it increased the number of MoS_2 edge sites and Brønsted acid sites, both of which contributed to a higher selectivity for DDO, reduced hydrogen consumption, and an increased yield of hydrocarbons. These studies emphasize the significant role of metal-support interactions in optimizing the efficiency of guaiacol HDO by modulating reaction selectivity and catalyst stability.

Other studies further illustrate the impact of catalyst choice and operating conditions on guaiacol HDO performance. He et al. (2019) [72] reported near-complete guaiacol deoxygenation over Rh/ZrO_2 in liquid-phase HDO, achieving an 87.7 mol% cyclohexane yield at 300 °C and 7 MPa. The study also identified key reaction steps, where hydrogenation dominated at lower temperatures, while complete deoxygenation

became more favorable at higher temperatures. Meanwhile, Li et al. (2020) [73] demonstrated that hierarchical ZSM-5 zeolites played a crucial role in directing reaction pathways by promoting mesopore-induced DDO and hydrogenation, thereby increasing the production of fully deoxygenated products. The presence of mesopores facilitated both oxygen removal and aromatic ring hydrogenation, suggesting that catalyst structure strongly influences the preferred reaction mechanism. Collectively, these studies reinforce the critical role of catalyst composition, support properties, and reaction conditions in shaping guaiacol HDO performance, guiding the development of more effective catalytic systems for bio-oil upgrading.

2.2.2. Bio-oil HDO

Several research have addressed the HDO of bio-oils and their oxygenated models. However, it is observable that most of the existing studies have focused predominantly on the HDO of isolated model compounds, highlighting phenol, anisole, guaiacol, hydroxymethylfurfural, among others. It is worth mentioning that bio-oils are composed of more than 300 substances, including aromatic oxygenates derived from lignin and C_{1-5} oxygenates from carbohydrates. Therefore, studies on HDO in single model compounds neglect the molecular interactions that occur during the HDO of these complex mixtures. In addition to the distinct adsorption-desorption characteristics of these oxygenates at different active catalytic sites, the formation of several reactive intermediates and their cross-reactive products play a significant role in influencing the HDO rate [60,74]

The HDO of bio-oil occurs in hydrogen environment with the presence of a catalyst at temperatures between 300 and 600 °C to eliminate oxygen in the form of water. The process involves several reactions, including dehydration, decarbonylation, decarboxylation, dealkylation, dealkylation, hydrogenation, hydrocracking, cracking, and transalkylation [58,75,76].

- Dehydration caused by condensation polymerization reactions.
- Decarbonylation (eliminates oxygen as CO).
- Decarboxylation (eliminates oxygen as CO_2).

• Dealkylation derived from cleavage of the C aromatic–O–CH_3 bond.

• Demethylation (DME) through the elimination of methane.

• Dealkoxylation eliminates oxygen in the form of alcohol, in which demethoxylation is frequent and releases methanol.

• Hydrogenation (saturation of unsaturated components).

• Hydrocracking and cracking, in which high molecular weight components are broken down into smaller molecules.

• Transalkylation (transfer of methyl groups).

• Hydrogenolysis, as a general nomenclature, is related to the disruption of C–O bonds.

While hydrodeoxygenation offers potential benefits, it presents challenges such as coke, decreased catalyst efficiency, polymerization, and high hydrogen and solvent consumption. Among the various methods studied, pyrolysis and liquid-phase hydrogenation have received significant attention. Liquid-phase hydrogenation involves subjecting lignin to a high-pressure treatment (50–100 bar) in a solvent such as an aliphatic alcohol, water, or phenol, under H_2 and/or a hydrogen donor. However, this approach has drawbacks, including solvent consumption, expensive high-pressure equipment, and difficulties in separating catalyst, coal, products, solvent, and lignin that has not reacted [9,77–81].

Research into lignin model compounds, derived from the depolymerization of lignin polymer, holds significant promise for advancing lignin valorization in high-value chemicals. The study of these model compounds offers several advantages, including aiding in the development of effective lignin conversion strategies and simplifying the analytical challenges associated with reaction networks and catalytic performance, particularly when compared to the more complex lignin polymer. [82]

2.2.3. Catalysts

2.2.3.1. Active Phase

Catalyst selection is critical in the HDO process. The most commonly used catalysts for HDO reactions generally include noble metals (Rh, Ru, Pt and Pd), transition metals (Ni, Co, Fe) and metal Molybdenum ((NiMo/Al_2O_3, CoMo/Al_2O_3), supported by metal oxides (TiO_2, Nb_2O_5). Sulfide-based catalysts indicated sulfur loss of metal sulfides and phase changes of metal oxides resulting in low HDO activity. Catalysts based on noble metals have excellent catalytic activities, however, their excessive cost limits their use for commercial purposes. In this sense, catalysts based on transition metals appear as a competitive option for application in HDO reactions [13,14,68].

In recent studies, Ni-based catalysts from non-noble metals have emerged as promising alternatives for hydrogenation due to their cost-effectiveness and efficient H_2 activation. However, Ni-based monometallic catalysts often require severe reaction conditions for effective hydrogenation/hydrodeoxygenation [81,83–86]. To overcome this limitation, several Ni-based bimetallic catalysts, including Ni-Fe, Ni-Co, Ni-Mo, and Ni-Zr, have been developed to increase activity through geometric or electronic effects López et al., (2020); Shu et al., (2017) [21]. For example, Ni-Fe bimetallic catalysts have been applied in upgrading.

According to Huang et al. 2022 [24], the synergistic effect between Ni-Fe alloy and basic sites on catalysts has been identified as a key factor increasing guaiacol conversion. A series of catalysts with Ni-Fe alloy nanoparticles in $MgAlO_x$ support demonstrated high efficiency in the conversion of guaiacol to cyclohexanol (32.1% yield) in liquid phase hydrodeoxygenation. The formation of the Ni-Fe alloy in bimetallic Ni-Fe catalysts has significantly improved the yield of non-oxygenated products such as cyclohexane.

Han et al. 2019 [18] observed a synergy between the Ni metal sites and the active sites of the Ni-Fe alloy facilitating the activation of H_2, allowing the efficient hydrogenolysis of cyclohexanol, identified as the rate-determining step for the hydrodeoxygenation of phenol with $20Ni_3$-Fe_1/MCSs, presenting a Ni/Fe ratio of 3/1, achieving the highest cyclohexane yield at 93.8%.

Bimetallic NiFe catalysts supported by (Si/Al = 12.5, Zeolite) were investigated for cyclohexane production through the hydrodeoxygenation (HDO) of

guaiacol [20], with the authors noting that different impregnation sequences can result in varied guaiacol conversion and cyclohexane yield. Specifically, when Fe was first impregnated and with a higher concentration of Ni sites contributed to the formation of Ni-Fe species, resulting in high rates of cyclohexane formation and guaiacol conversion. On the other hand, the first sample impregnated with Ni showed a reduced number of Ni atoms involved in the formation of Ni-Fe species, leading to the lower conversion rate of guaiacol.

These findings highlight the critical role of metal composition and distribution in determining catalytic performance. Similarly, the proportion between Ni and Fe has been shown to significantly influence product selectivity. In a related study conducted by Fang et al. (2017) [87], the investigation of Ni-Fe/CNT catalysts for guaiacol HDO demonstrated an adjustable product distribution based on Ni/Fe atomic ratios (5/1), achieving a 99.8% yield for cyclohexane and 83.7% yield for phenol. Xin et al. (2020) [88] further identified the formation of a $FeNi_3$ alloy, influenced by Fe-Ni interactions and the support material, which favored the HDO pathway in palmitic acid conversion. The optimal Ni and Fe charge balance, as exemplified by the 10% Ni-5% Fe/γ-Al2O3 and 10% Ni-5% Fe/HZSM-5 catalysts, resulted in complete palmitic acid conversion with high selectivity toward pentadecane and hexadecane, respectively, offering valuable insights for the design of highly active and selective catalysts.

Bimetallic catalysts, such as Ni-Fe, exhibit enhanced hydrogenolysis capabilities due to their unique specific configuration. The catalytic behavior can be tuned by modifying the Ni/Fe ratio, where Ni atoms play a role in hydrogen activation, while Ni-Fe sites influence hydrogenolysis [82,89]. Thus, achieving an optimal balance between hydrogenation and hydrogenolysis is essential for efficient HDO performance. An ideal catalyst should provide a high Ni content to ensure sufficient hydrogen activation while maintaining an appropriate Fe concentration to regulate hydrogenolysis. Therefore, further investigation into the role of Ni and Ni-Fe surface sites on HDO activity is necessary, particularly by varying the Ni/Fe atomic ratio and analyzing its impact on catalytic surface properties.

2.2.3.2. SUPPORT NIOBIA

Catalyst supports are essential for dispersing and stabilizing active metals while also providing catalytic deoxygenation sites, such as Brønsted and Lewis acid sites, as well as oxygen vacancies. However, they can also interact with active metals to generate new catalytic sites, as they are able to improve diffusion between materials. The molecular sieves HZSM-5, SBA-15, MCM-41 and γ-Al appear as common acid scaffolds widely used in the preparation of HDO catalysts. However, hydrothermal reaction conditions often affect the stability of catalysts, which mainly depends on acidity to maintain high deoxygenation efficiency. That is, desilication or dealumination can lead to the destruction of the molecular sieve structure and cause the catalyst to be deactivated. Some studies have reported that water molecules competitively adsorbed on the active sites of γ-Al_2O_3 and induced their recrystallization and the severe coking of the reactants caused by the strong acidity covered the active metals. In this sense, metal oxides that mainly provided oxygen vacancies and had certain acidic properties have been considered as advantageous alternative supports, such as Nb_2O_5, ZrO_2, TiO_2, CeO_2 and CrO_2 [90–95].

Niobium pentoxide (Nb_2O_5) exhibits numerous polymorphic crystalline phases, including amorphous structures, each possessing distinct physical properties. Nomenclature systems for these polymorphs have been subject to complexity and variation, with Schäfer et al. (1966) [96] proposing a comprehensive system based on temperature-related classifications (TT, T, M, and H) and shape-based distinctions (B, N, and R). Ko and Weissman [97] further contributed to the understanding of the crystalline phases resulting from the heating of amorphous Nb, emphasizing the impact of factors such as impurities, starting material, and catalyst preparation methods on the final structure

Niobic acid ($Nb_2O_5 \cdot nH_2O$), the amorphous hydrated form of Nb_2O_5, known for its high acid strength, exhibits unique characteristics, including a composition composed primarily of distorted NbO_6 octahedra and NbO_4 tetrahedra. The proposed nomenclature systems assist in distinguishing common phases obtained through various calcination temperatures, such as the pseudo-hexagonal TT phase (400–500 °C), orthorhombic T-phase (600–800 °C), and tetragonal M-phase (around 800 °C). The most stable thermodynamic phase, the monoclinic H-phase, is formed at temperatures above 1000 °C [96,98].

In addition, the discussion extends to the polymorphs TT-Nb_2O_5, T-Nb_2O_5, M-Nb_2O_5, B-Nb_2O_5, and H-Nb_2O_5, each characterized by distinct crystal structures and properties. Notably, the TT phase has generated debates regarding its crystal structure, with recent studies proposing a disordered pseudo-hexagonal unit cell converging into a monoclinic system [99]. In addition, the amorphous Nb_2O_5 hydrate, niobic acid, is distinguished by the presence of strong Brønsted and Lewis acid sites, offering advantages over zeolites in terms of acidity and water tolerance. The crystalline phases, such as T and TT, have orthorhombic and pseudo-hexagonal structures, respectively, while the M phase adopts a tetragonal structure. Phase B, formed at intermediate temperatures, has a monoclinic structure characterized by laminated crystalline habits. The H phase, obtained at elevated temperatures, appears as the most stable polymorph, but with reduced acidity due to the removal of acidic sites during the phase transition [96,98]

To explore the impact of the Nb_2O_5 structure on the hydrodeoxygenation ratio, several crystal structures of the support were investigated. In a study conducted by several Ni/Nb_2O_5 catalysts with distinct crystal structures - pseudohexagonal (Ni/TT-Nb_2O_5), orthorhombic (Ni/T-Nb_2O_5) and monoclinic (Ni/M-Nb_2O_5) - were synthesized by adjusting calcination temperatures [100]. The catalytic performance in the hydrodeoxygenation of vanillin was examined, revealing that physicochemical properties such as oxygen vacancies, acidic sites, metal-support interaction and valence states significantly influenced the catalytic activity. Among the catalysts, Ni/T-Nb_2O_5 showed excellent performance, achieving 96.1% conversion of vanillin and 79.2% Yield for 4-methoxyphenol under specific conditions. The abundant oxygen waves in Ni/T-Nb_2O_5 facilitated the HDO of vanillin by adsorbing and activating oxygen functional groups, promoting vanillin hydrogenation and 4-methoxyphenol hydrogenolysis. In addition, water contributed to a stronger transition state with 4-methoxyphenol by reducing the dissociation energy of the C–OH bonds. The synergistic effect between oxygen waves and water improved the efficient hydrodeoxygenation of vanillin in an aqueous environment.

In a related study conducted by Campos Fraga et al. (2023) [99], catalysts named based on the obtained polymorphs (Pd/A- Nb_2O_5, Pd/TT&A- Nb_2O_5, Pd/T&TT-Nb_2O_5, Pd/M&T- Nb_2O_5) and nanostructured Nb_2O_5 (Pd/NS- TT- Nb_2O_5) were

prepared and tested for the enhancement of the light phase of beech wood fast pyrolysis oil. The experiments, conducted at 250 °C and 80 bar H_2, demonstrated that Pd/NS-TT-Nb_2O_5, due to its abundant acidic sites and larger surface area, exhibited the highest H_2 uptake and, consequently, the highest hydrogenation and hydrogenolysis during the reaction. Pd/NS-TT-Nb_2O_5 achieved the highest removal of oxygen as water (36% by weight of the initial organic oxygen) and showed the lowest tendency for coking and oil viscosity due to the high hydrogen content in the updated products. The study highlights the influence of Nb_2O_5 structure on catalytic performance in HDO reactions, emphasizing the importance of crystalline phases and nanostructure in the design of efficient catalysts for biomass improvement.

Ma et al. (2019) [101] compared the source and structure of commercial niobium-based catalyst for HDO of cresol. Utilizing niobic acid (HY-340), niobium phosphate (NbPO-CBMM), and laboratory-prepared layered niobium oxide (Nb_2O_5-Layer) as carriers. The study revealed that the Lewis acid sites of the support, rather than the Brönsted acid sites facilitated the C–O breakage of phenolic compounds. The Ru/Nb_2O_5-Layer catalyst, characterized by a high quantity of Lewis acid sites, a large specific surface area, and good Ru dispersion, demonstrated a mole yield of 99.1% for C_{7-9} hydrocarbons and a Yield of 88.1% for C_{7-9} aromatic hydrocarbons in the enzymatic lignin conversion. It has been observed that the acidity of Nb_2O_5 increases hydrogenolysis and hydrogenation reactions during HDO upgrade of FPBO, resulting in a less viscous oil with higher hydrogen (H_2) absorption.

In a study led by Campos Fraga et al. (2022) [102], the performance of Pd/Nb_2O_5 was compared to the Pd/SiO_2 catalyst. The results revealed that the upgraded oil produced by Pd/Nb_2O_5 exhibited higher fluidity and lower average molecular weight compared to the Pd/SiO_2 catalyst. In gas-phase HDO of guaiacol.

In conclusion, the selection of Nb_2O_5 as a catalyst support in this thesis is founded due to its attributes, including water resistance, stability, appropriate acidity, and effective C–O bond cleavage capabilities. Moreover, the catalytic performance of Nb_2O_5 has been demonstrated in various hydrodeoxygenation (HDO) studies, particularly in the selective removal of oxygenated compounds from bio-oils, making it a promising material for biomass valorization. Additionally, the interactions between Ni and Fe in bimetallic catalysts have proven to significantly influence the efficiency of

HDO reactions, with optimized metal ratios leading to enhanced hydrogenation and hydrogenolysis activity. The findings from previous studies suggest that controlling the Ni/Fe ratio, impregnation sequence, and catalyst support properties are important factors to achieving high conversion rates and selectivity.

Furthermore, Brazil holds approximately 98% of the world's known niobium reserves, solidifying its position as the global leader in niobium production [103]. The strategic utilization of Nb_2O_5 not only aligns with the country’s abundant niobium resources but also reinforces the sustainability and economic feasibility of employing niobium-based catalysts in biomass conversion technologies. Understanding the structure-activity relationships of these materials will be critical for developing more efficient and sustainable catalytic systems for biofuel and chemical production.

CHAPTER 3

MEDODOLOGY

The following chapter describes the materials and methodologies used in the experimental development of this thesis. For better understanding, it has been divided into two sections: the first presents the preparation of catalysts and their physicochemical characterizations, and then, in the second part, the conditions employed in the catalytic tests are described.

3.1. CATALYST PREPARATION

Initially, the support, niobic acid ($Nb_2O_5.nH_2O$, HY-340), provided by CBMM, Brazil, was subjected to a calcination at 500 °C for 4 hours in an air atmosphere, with a heating ramp of 10 °C, aiming to obtain TT-Nb_2O_5. Silica 50 (Aerosil^R OX 50) provided by Evonik, Germany with a specific area of 50 m^2/g was also calcined under the same conditions to remove the present water. Subsequently, nickel (Ni) and iron (Fe) precursors, sourced from Sigma Aldrich, St. Louis, MO, USA, namely Nickel (II) nitrate hexahydrate ($Ni(NO_3)_2 \cdot 6H_2O$) for Ni and Iron (III) nitrate nonahydrate ($Fe(NO_3)_3 \cdot 9H_2O$) for Fe, were added in stoichiometric quantities to a flask, along with the calcined support, for wet impregnation. Wet impregnation was performed in a rotary evaporator, where the solution was stirred for 8 hours. Afterwards, the water was evaporated under specific conditions of 45 mbar and 35 °C, with a rotation speed of 200 rpm, continuing until complete water evaporation was achieved. The resulting solid was then dried at 100 °C for at least 12 hours.

Following drying, the solid underwent a further calcination step at 350 °C for 3 hours. The ruthenium catalyst followed a similar methodology, using Ruthenium (III) chloride hydrate ($RuCl_3 \cdot xH_2O$), sourced from Sigma Aldrich, St. Louis, MO, USA, as the precursor. The drying, calcination conditions were maintained the same as the Ni-Fe catalysts.

FIGURE 2. Representative scheme of the catalyst preparation procedure

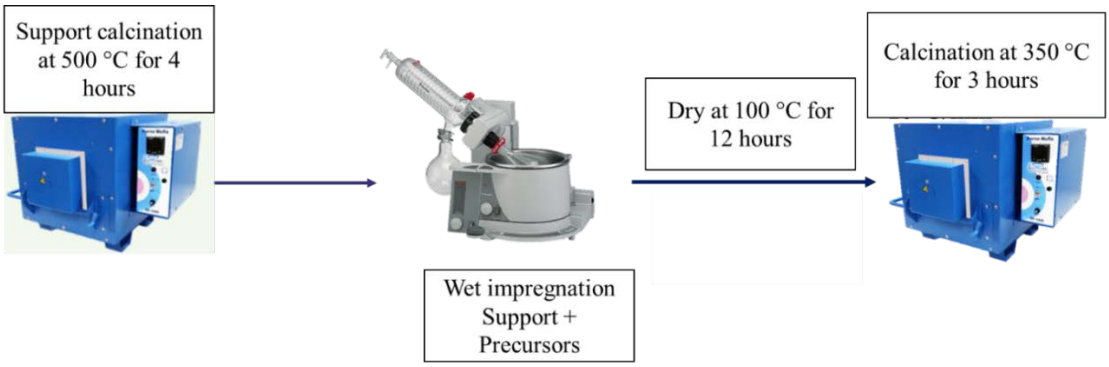

In addition to the preparation of catalysts in powder form, catalysts in pellet form were also prepared using the same method. However, niobic acid pellets (Nb_2O_5) from CBMM, Brazil, of the same grade (HY-340) were used as the support material instead of powder. The impregnation of the pellet support with the active metal precursors (Ni and Fe or Ru) followed the same procedure previously described for the powder catalysts. After impregnation, the pellets were dried and calcined using identical conditions to those for the powder catalysts. The results are presented in Figure 3.

FIGURE 3. Nb_2O_5 Pellets Impregnated with 5%Ru.

The mass of the metal precursor was estimated according to the desired mass concentration of metal relative to the support mass (on a dry basis), as represented in Equation (1)

$$m_{\text{Metal Precursor}} = \left(\frac{\%\text{Metal}}{100}\right) \cdot \frac{m_{Support} \cdot \text{MM}_{\text{Metal Precursor}}}{MM_{\text{Metal}} \cdot \text{p}_{\text{Metal Precursor}}} \quad (1)$$

Where $m_{\text{Metal Precursor}}$ is the mass of the metal precursor (g), % Metal is the mass concentration of the metallic phase to be deposited on the support, $m_{Support}$ is the mass of the support (g), $\text{MM}_{\text{Metal Precursor}}$ and MM_{Metal} are the molar masses of the metal precursor and the monoatomic, respectively, and $\text{p}_{\text{Metal Precursor}}$ is the purity grade of the metal precursor.

Thus, six catalysts were produced with nominal loading of metals in different percentages by weight described in below. In this case, the Ni loading was kept constant at 5.0 wt.% on all samples, while the Fe loading was varied from 1.0 and 5.0 wt.%.

TABLE 2. Percentage by weight of metal impregnated in niobium supports (Nb_2O_5) and silica (SiO_2).

	Catalyst	Ni (wt. %)	Fe (wt. %)	Ru (wt. %)
Powder	Ni/ Nb_2O_5	5	0	0
	Ni/SiO_2	5	0	0
	Fe/ Nb_2O_5	0	5	0
	Fe/SiO_2	0	5	0
	Ni-Fe/ Nb_2O_5	5	5	0
	Ni-Fe/ Nb_2O_5	5	1	0
	Ni-Fe/SiO_2	5	1	0
	Ni-Fe/SiO_2	5	5	0
	Ru/ Nb_2O_5	-	-	5
Pellet	Ru/ Nb_2O_5	-	-	5
	Ni-Fe/Nb_2O_5	5	1	-

3.2. CATALYST CHARACTERIZATION

3.2.1. Inductively Coupled Plasma Optical Emission Spectroscopy (ICP-OES):

The elemental composition of both the fresh and spent catalysts was measured for the metal content was performed using inductively coupled plasma optical emission spectroscopy (ICP-OES) on an Agilent 725 spectrometer. Prior to analysis, a pre-digestion step was conducted to digest the catalyst, especially Nb. The pre-digestion involved treating the catalyst with a mixture of HNO_3 (65%), HCl (37%), HF (40%), and H_2O_2 (35%) in a microwave oven at 240 °C for 45 minutes. Subsequently, the material was analyzed in an Agilent 725 ICP-OES spectrometer with argon as the plasma gas (15 L . min^{-1}, 40MHz, 20 kW). This analysis was carried out at the Karlsruhe Institute of Technology (KIT) in Germany.

3.2.2. BET Area:

Nitrogen adsorption-desorption measurements for determining the textural properties of the support and calcined catalysts were performed on a Micromeritics Belsorp Mini II equipment at 77 K, within a P/P_0 range of 0.01 to 0.99. Before each analysis, approximately 0.3 g of sample was thermally pre-treated in situ at 200 °C under vacuum (2 μmHg) for 12 hours, a process aimed at removing moisture from the sample's surface. The specific surface area (S_{BET}) was calculated using the BET method (named after researchers Brunauer, Emmett, and Teller). This analysis was carried out at the Karlsruhe Institute of Technology (KIT) in Germany.

3.2.3. X-ray Diffraction (XRD)

The crystal structure of the catalysts before and after reduction, was determined using X-ray diffraction (XRD) analysis. An X'Pert PRO MPD instrument from PANalytical GmbH equipped with a copper anode (Cu Kα 1.5406 Å) was employed for the XRD measurements. This analysis was carried out at the Karlsruhe Institute of Technology (KIT) in Germany.

The measurements were conducted in the 2θ range from 10° to 80° for 60 minutes with a step size of 0.017°. The Scherrer Equation (2) was utilized to estimate the average crystal size (τ), considering a shape factor (K) of 0.9. This calculation involved correction for instrumental line broadening and, if necessary, subtraction of

the contribution of the support signal [104]. The software X'Pert High score Plus was utilized for data analysis.

$$\tau = \frac{K\lambda}{\beta\cos(\theta)} \quad (2)$$

Where τ is the average crystal size, K is the shape factor (assumed as 0.9), λ is the X-ray wavelength, β is the line broadening at half the maximum intensity, given by $\beta=\Delta(2\theta)$, and θ is the Bragg angle.

3.2.4. Temperature-Programmed Reduction (TPR)

The Temperature-Programmed Reduction (TPR) analysis was performed using the AMI-300 chemisorption analyzer from Altamira Instruments, a fully automated system equipped with a thermal conductivity detector (TCD). This instrument allows for the quantification of hydrogen uptake by the samples and the acquisition of reduction profiles, making it highly suitable for investigating the interactions between metal phases and supports in heterogeneous catalysts. The system is controlled by LabVIEW-based software, enabling precise programming of temperature ramps, gas flow rates, and data acquisition.

The calcined samples were weighed (0.03 g) and placed in a fixed-bed quartz reactor. To remove moisture and adsorbed impurities, an in-situ pre-treatment was conducted under argon flow (30 mL·min^{-1}) at 200°C for 30 minutes. After cooling the system to 30°C, the gas atmosphere was switched to a 10% H_2 in Ar mixture with a total flow rate of 50 mL·min^{-1}, controlled by a mass flow controller (MFC). The sample was then heated from 30°C to 850°C at a rate of 5°C·min^{-1}, while the TCD continuously monitored thermal conductivity variations due to hydrogen uptake during the reduction of metallic species.

FIGURE 4 Interface of the AMI-300 software from Altamira Instruments, used TPR and TPD analysis.

The image illustrates the software's functionality, including pulse calibration selection, analytical area determination, and the applied calculations. The data shown in this image

are for illustrative purposes only and do not correspond to any analysis conducted in this thesis.

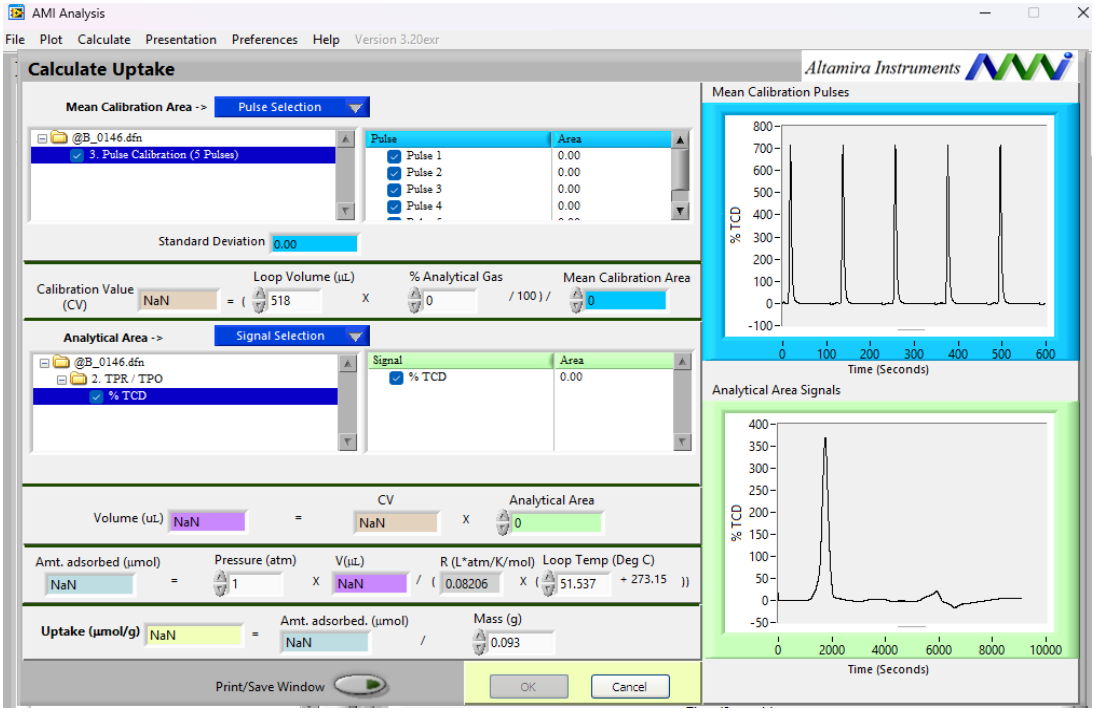

The hydrogen consumption by the samples was calculated based on the reduction peak area using the internal calibration of the AMI-300 software, which integrates the area under the reduction peaks and correlates it with the volume of gas consumed. The equation used for the calculation (3) of hydrogen uptake (n_{H_2}) is given by:

$$n_{H_2} = \frac{P \cdot V}{R \cdot T} \tag{3}$$

where P is the gas pressure (1 atm), V is the volume of hydrogen consumed (in µL), R is the gas constant (0.08206 L·atm·K^{-1}·mol^{-1}), and T is the absolute temperature (in Kelvin).

The degree of reduction (DOR) of metallic catalysts was calculated according to Equation (4), assuming that the calcined materials were in the NiO oxide form and that reduction during TPR-H_2 analyses occurred completely to form Ni^0, where MM_{Ni}

is the molar mass of metallic nickel (58.6934 g·mol^{-1}), m_{cat} is the mass of the catalyst (g), and X_{Ni} is the nickel content in the catalyst obtained through ICP analysis.

$$\text{DOR (\%)} = \frac{MM_{Ni} \times n_{H_2}cat}{m_{cat} \times X_{Ni}} \times 10 \quad (4)$$

3.2.5. Hydrogen Temperature-Programmed Desorption (H_2-TPD)

The metallic dispersion (Dp) and nickel particle size (dp) (equations 1 and 2) [105] were measured via temperature-programmed hydrogen desorption (H_2-TPD). Before the tests, approximately 100 mg of the sample was reduced in situ under a flow of H_2 (30 mL·min^{-1}, ramp 5 K·min^{-1}) at 500 °C for 1 hour. Following this reduction, the samples were cooled to 50 °C under an argon flow (ramp 10 K·min^{-1}) and further rinsed for 10 min. The samples were then exposed to 33 vol% H_2 in argon for 30 min (10 mL·min^{-1} H_2 + 30 mL·min^{-1} Ar). Excess H_2 was then removed by flushing the sample with pure argon for ca. 90 minutes. The actual H_2-TPD analysis was performed by heating from ambient temperature to 900°C at a rate of 10 K·min-1 and holding at that temperature for 30 min.

$$\text{Dp}(\%) = \frac{\text{Ns}}{\text{Nt}} \times 100 \quad (5)$$

$$d_p = \frac{f}{Dp} \quad (6)$$

where Ns is the number of active sites (the number of chemisorbed molecules multiplied by n, the stoichiometric factor) and Nt is the number of total atoms. For the nickel particle size, factor f depends on the geometry according to Schmal et al. (2016) [105] for nickel, which is 101.2 Å^2.

3.2.6. Ammonia Temperature-Programmed Desorption (TPD)

The relative number of acidic sites present in the catalysts was determined by NH_3 temperature-programmed desorption (NH_3-TPD) using an Altamira chemisorption analyzer (AMI-300). The analyzer is equipped with a thermal conductivity detector (rhenium-tungsten) and three mass flow controllers (Hastings Company). The chemisorption equipment was piloted via software ("AMI 300") from the Altamira software package. The samples were first reduced under a H_2/Ar stream (20 ml·min^{-1} H_2 + 20 ml·min-1 Ar) from 40 °C to 500 °C with a 5 K·min^{-1} ramp holding at 500°C for 1 hour (conditions similar to those used in the testing reactor). Afterwards, the samples were flushed with helium while the temperature was decreased to 100 °C (ramp 10 K·min^{-1}). The adsorption of ammonia was subsequently performed for 60 min with a flow of 30 ml/min 5 % NH_3/He (air-liquid crystal gas mixture). The samples were subsequently flushed for 60 min at 100 °C with 30 ml/min pure helium. TPD analysis was carried out from 100 °C to 700 °C at a heating rate of 5 K·min^{-1} in a 30 ml·min^{-1} pure helium flow. The composition of the exit gas was monitored online via an internal thermal conductivity detector (TCD). The TCD detector was calibrated after the TPD measurement using the same 5 % NH_3/He mixture (5 pulses, volume of the loop 518 ul).

3.2.7. Scanning Electron Microscopy

Scanning electron microscopy (SEM) coupled with energy-dispersive X-ray spectroscopy (EDS), was utilized to assess the morphology and elemental distribution of the fresh catalysts. The measurements were conducted using a DSM 982 Gemini instrument equipped with secondary ion, backscatter, and transmission detectors from Carl Zeiss Ltd. For EDS analysis, a Si (Li) X-ray detector (Inca Pent FET, 30 mm² crystal size, Oxford Instrument, Abingdon, UK) coupled to the SEM equipment was employed, performed at the Karlsruhe Institute of Technology (KIT) in Germany.

Although these techniques offer detailed insights into the elemental composition on the surface of the catalysts, the figures generated by SEM provided limited information regarding the morphology of the essentially non-crystalline materials, and thus, they were not the primary focus of this investigation.

3.2.8. X-ray photoelectron spectroscopy (XPS)

X-ray photoelectron spectroscopy (XPS) was utilized to assess the surface composition of reduced Ru catalysts. The analysis was performed using a VersaProbe II instrument, equipped with Al Kα (1486.7 eV) monochromatic X-ray for excitation. Reduced samples were transferred to the instrument's introduction chamber under an argon atmosphere from an anoxic glovebox, ensuring anoxic conditions were maintained throughout the procedure. The PHI MultiPak software version 9.9 was employed for the analysis. This included a charge referencing technique that calibrated the C 1s peak for the Nb_2O_5 support at 284.8 eV, and the binding energies for elemental lines were charge-referenced to the O 1s of hydroxide at 531.4 eV.

X-ray photoelectron spectroscopy operates by directing an X-ray beam at a sample, aiming to eject electrons from the surface atomic layers. When an X-ray photon hits the sample, it has sufficient energy (E = hν) to remove electrons from the k-shell, imparting them with kinetic energy Ek. The binding energy of the photoelectron from the atom (EB) is deduced from the values of hν and Ek according to the Equation (7)

$$EB = h\nu - Ek - \Phi \quad (7)$$

Here, Φ symbolizes the work function, the energy required for an electron to escape from the material's surface.

3.3. CATALYST TESTING

3.3.1. HDO OF GUAIACOL

The hydrodeoxygenation (HDO) reaction was conducted in a 200 mL autoclave made of Inconel alloy 625, designed for operation at a maximum pressure of 36 MPa and a maximum temperature of 400 °C, depicted in Figure 5. The autoclave features cartridge heaters in a brass jacket for temperature control, managed through LabView and a group of three sensors: internal and external temperature sensors, and a pressure sensor. Additionally, it is equipped with a magnetically coupled gas injection stirrer (80 N·cm of torque, Premex, Lyss, Switzerland). The introduction of H_2 via the stirrer is intended to enhance gas contact with the oil, increasing the availability of hydrogen thereby reducing polymerization [106].

FIGURE 5. Batch Autoclave scheme for the HDO Reaction, built in-house at IKFT, KIT

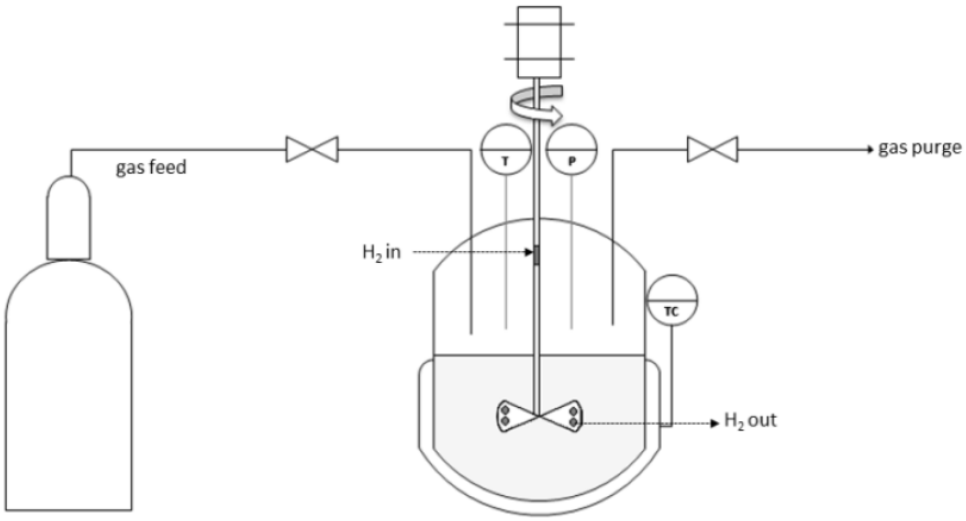

FIGURE 6. Batch autoclave image for the HDO reaction, built in-house at IKFT, KIT.

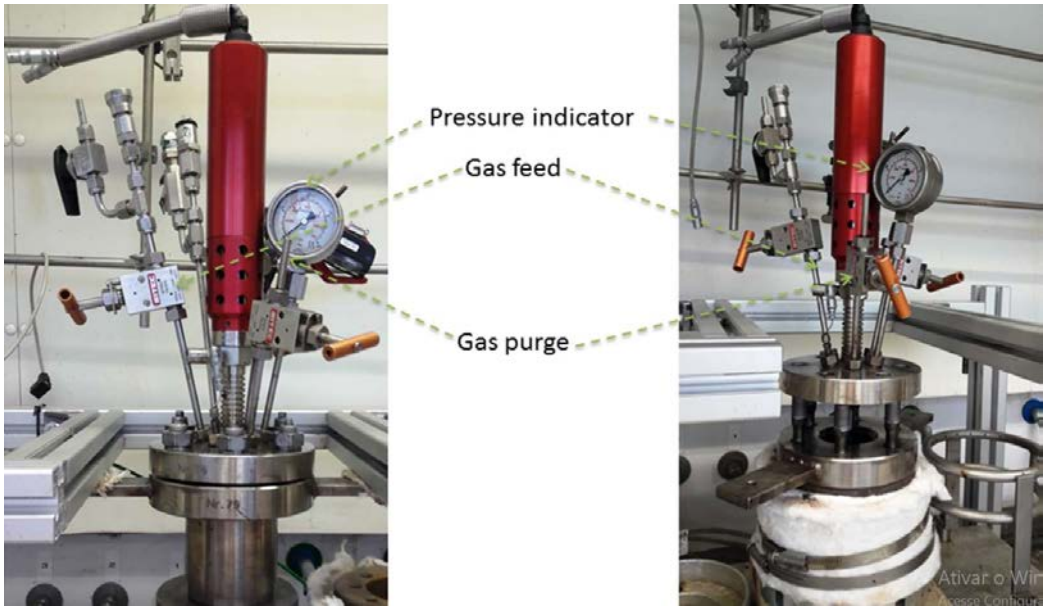

Prior to hydrodeoxygenation (HDO) reaction, the catalyst underwent reduction and passivation in a reduction oven. The reduction process was carried out under an atmosphere consisting of a constant 10 vol.% H_2 in N_2, with a flow rate of 2.7 L . min^{-1}. For Ru catalysts, the reduction temperature was maintained at 350 °C for 2 hours,

while for Ni catalysts, a higher temperature of 500 °C was applied for 2 hours. The heating ramp for both reductions was set at 5 °C . min^{-1}. The elevated reduction temperature for the Ni catalysts was chosen to ensure the complete conversion of NiO to elemental Ni (C. Li & Chen, 1995a). Following the reduction, passivation was carried out to stabilize the reduced phases. After cooling the catalysts in an ice bath to a temperature between 0 and 5 °C, they were exposed to a 5% O_2/N_2 atmosphere for 30 minutes

The performance of the catalysts was assessed through triplicate testing. For each experiment, 25 g of guaiacol and an adjusted amount of catalyst were added to the reactor to ensure a consistent absolute quantity of active metal phase (NiFe) across all reactions. The catalysts contained either 10%, 5%, or 6% of active metal, so the total catalyst mass was selected to provide the same active metal content in each reaction. This adjustment ensured a fair comparison of catalytic performance.

The catalyst mass used for each reaction was determined as follows:

$$m_{catalyst} = \frac{m_{active\ metal}}{Metal\ loading\ (\%)} \tag{8}$$

Decalin was chosen as the solvent for the mixture due to its stability against hydrodeoxygenation and its recognition as an effective solvent in related research [108]. The autoclave was then sealed and purged with argon before pressurization to 8 MPa at room temperature with H_2 (Air Liquide 6.0, Paris, France). The stirrer rotation speed was set to 800 rpm, and the reactor was heated to achieve the required temperature with a total reaction time of 2 hours, including the heating ramp. Subsequently, the reaction was quenched by cooling with compressed air until the reactor's internal temperature dropped below 40 °C. After cooling, a gas sample was extracted for analysis via gas chromatography. The non-gaseous upgraded products were collected and weighed.

The chemical compositions of the samples were analyzed quantitatively and qualitatively using gas chromatography (GC-FID/MS). For both cases, the samples were diluted with tetrahydrofuran (THF) with a ratio 1:10 being afterwards filtrated. Quantitative analysis employed an Agilent 7820A gas chromatograph with an Rxi®5Sil MS capillary column (0.25µm×0.25µm×30 m) and a flame ionization detector. External

calibration was performed for each compound. The specific analytical data and results for these compounds are detailed in Appendix 1.

For qualitative analysis, an Agilent 6890N coupled with Agilent 5973N mass spectrometer (MS) and flame ionization detector (FID) was used, with a column-type RTX-5MS (0.25μm×0.25μm×30 m). The injection temperature was set at 280 ℃, and helium served as the carrier gas at a flow rate of 1.5 mL . min^{-1}. The oven temperature started at 35 ℃ for 2 minutes, followed by a heating ramp of 8 ℃ . min^{-1} to 240 ℃, then reduced to 4 ℃ . min-1 until reaching 280 ℃. After a 15-minute holding time, the analysis concluded **Figure 7** Qualitative assessments were made by comparing the spectra to the NIST database.

Figure 7. Heating Ramp for Analysis of the liquid samples in GC-MS and GC-FID

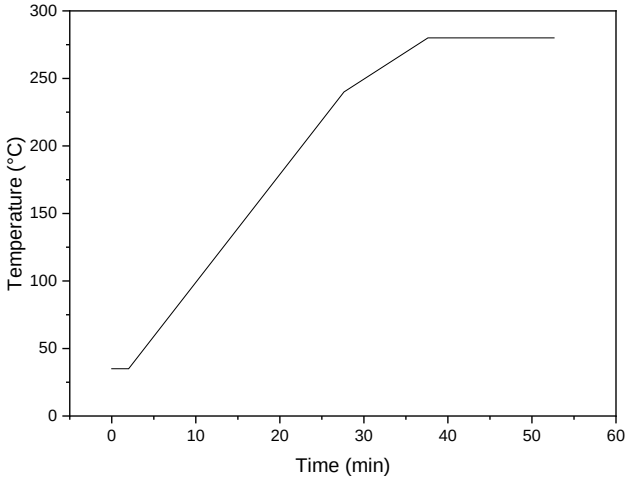

FIGURE 8. Heating Ramp for Analysis of the gas samples in GC-TCD and GC-FID

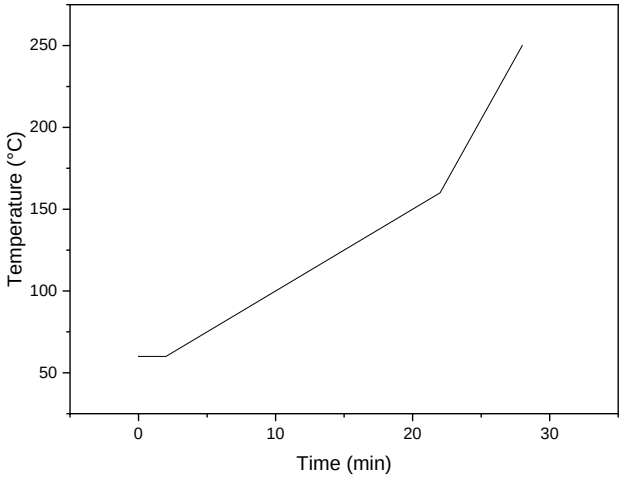

For gas samples, 100 µL was injected into the Agilent 6890 gas chromatograph using helium as the carrier gas. The injection temperature was consistently maintained at 250 ℃ throughout the analysis. The initial oven temperature was set at 60 ℃ for 2 minutes, followed by a heating ramp of 5 ℃ . min^{-1} until reaching 160 ℃. Subsequently, the oven was further heated to 250 ℃ with a ramp of 15 ℃ . min^{-1}. Two distinct columns, Restek 57096 Hayesep Q and Restek Molsieve 5A, were employed alongside a valve switching system. Detection of components utilized both the thermal conductivity detector (TCD) and the flame ionization detector (FID). External

calibration was performed for each compound. The specific analytical data and results for these compounds are detailed in Appendix 1.

The conversion and selectivity for each product were calculated as follows:

$$X\ GUA\ (\%) = \frac{mol\ of\ GUA\ in\ the\ product}{mol\ of\ GUA\ consumed} \times 100 \quad (9)$$

$$Selectivity\ (\%) = \frac{mol\ of\ the\ molecule\ in\ the\ product}{mol\ of\ GUA\ consumed} \quad (10)$$

3.3.3. HDO OF BIO-OIL

The experiments were made utilizing the light phase of beech wood fast pyrolysis oil (BTG Biomass Technology Group BV, Enschede, The Netherlands). Choosing the light phase over the whole oil offered several advantages. Moreover, owing to its high-water content (32 wt. %) and consequent low heating value, the light phase lacked value as a fuel precursor without appropriate upgrading. Additionally, the low viscosity of the light phase facilitated easier handling and minimized losses of the upgraded product.

To separate the light and heavy phases before hydrotreatment, the bio-oil underwent intentional aging at 80 °C for 24 hours [109]. The denser heavy phase, rich in organic compounds, settled at the bottom, while the lighter phase, abundant in water, occupied the upper part. This method is also good to separate the solids that could negatively influence the catalysts performance.

The HDO reaction was executed in the same reactor used for the guaiacol reaction and each reaction was performed in triplicate. The reaction conditions were previously stablished by Campos Fraga et al. (2022) and Boscagli et al. (2015) [102,109], using the same feedstock. In each HDO experiment, the batch reactor was charged with 50 g of light phase beech wood pyrolytic oil (feed) and 2 g of pre-reduced catalyst. The stirrer rotation speed was set to 800 rpm, and the reactor was heated to 250°C (heating ramp of 3.33 °C·min^{-1}), with a total reaction time of 2 hours, including the heating ramp. Subsequently, the reaction was quenched by cooling with compressed air until the reactor's internal temperature dropped below 40°C and a gas sample was

extracted for analysis via gas chromatography. Subsequently, non-gaseous upgraded products were collected, weighed, and subjected to centrifugation for 40 minutes at 9,000 rpm using a Thermo Scientific Heräus Biofuge Stratos fixed-angle rotor 26 (No. 75003014, Thermo Fisher Scientific, Waltham, MA, USA).

Post-centrifugation Figure 9, the aqueous phase (AP) at the top primarily comprised water and polar compounds, while the bottom oil phase, referred to as upgraded oil (UO), consisted of a rich organic mixture with high viscosity. The solids, predominantly comprising recovered catalyst and any carbon compounds resulting from coking reactions, underwent washing with acetone and ethanol to eliminate all soluble organic products. Following separation, the aqueous phase and recovered solids were weighed.

FIGURE 9. Recovered Products after Centrifugation

FIGURE 10. Product separation due to Centrifugation. Light Aqueous Phase on the left, oil phase on the right and in the bottom is the solid Residue.

The recovery of upgraded oil and theoretical recoveries were calculated as described in the Equation (11). The recovered products (*RP*) were weighed together. After separation by centrifugation, the aqueous phase (*AP*) and recovered solids (*S*) were weighed, and the mass of the upgraded oil (*UO*) was calculated as follows.

$$mUO = mRP - mAP - mS \quad (11)$$

Since there are small losses when removing the product from the batch reactor, theoretical mass values (*mth*) of the liquid products are related by considering equal relative losses of both phases. That is:

$$\frac{(mAPth)}{(mUOth)} = \frac{mAP}{mUO} \quad (12)$$

Various techniques were employed to characterize the feedstock and liquid products as Water Content Measurement that is measured through Karl Fischer titration with the Titrando 841 system (Metrohm), using iodine, sulfur dioxide, and imidazole as titrant. Elemental Analysis to determination of carbon, hydrogen, and nitrogen contents. The analysis was performed using elemental analysis on Leco True Spec Macro, LECO Europe, Software version 2.53 Corporation Copyright® 2001–2010. Oxygen content was determined by assuming samples comprised only carbon, nitrogen, hydrogen, and oxygen using the Equation (13).

$$O\ wt.\% = 100\ wt.\% - C\ wt.\% - H\ wt.\% - N\ wt.\% \quad (13)$$

One indicator to regard the HDO process is degree of deoxygenation (DOD). It showed, in which extend oxygen has been removed from the bio-oil through the HDO process. The Equation (**14**) to calculate the DOD value is as the following.

$$DOD\ wt.\% = 100 - \frac{(O_{product\ wt}.\%)}{(O_{feed\ wt.}\%)} \quad (14)$$

The higher heating value was calculated using the Channiwalla-Parikh equation [110] with values from elemental analysis. It was estimated through the following Equation (**13**):

$$HHV(MJ\ /\ kg) = 0.3491 \cdot C\ wt.\% + 1.1783 \cdot H\ wt.\% - 0.1034 \cdot O\ wt.\% - 0.0151 \cdot N\ wt.\% + 0.1005 \cdot S\ wt.\% - 0.0211 \cdot ash\ wt. \quad (15)$$

The chemical compositions of the samples were analyzed quantitatively and qualitatively using gas chromatography (GC-FID/MS). The method, equipment and column were the same as the used for HDO of guaiacol analyze reported in the previous section.

A semi-quantitative analysis was carried out by evaluating the peak areas of compounds identified in the GC-MS results using Agilent MassHunter software. This analysis was restricted to compounds that exhibited a significance level above 80%. The selected compounds' peak areas were aggregated, and the semi-quantitative value for each compound was calculated by comparing its peak area to the total of all measured peak areas. It is important to note that the semi-quantitative analysis with GC-MS is limited to volatile components; non-volatile substances, such as heavy tars or polymers that may form during hydrodeoxygenation (HDO) processes, are not detected and thus not represented in the analysis.

The hydrogen consumption was determined by calculating the initial and final amounts of hydrogen gas in the reactor using the ideal gas law equation (equation 17). The initial moles of H_2 were calculated based on the reactor volume, initial pressure, and temperature, considering the 99% purity of H_2 gas. The final moles of H_2 were determined using the same equation but incorporating the final pressure and temperature along with the H_2 concentration obtained from gas chromatography (GC) analysis of the outlet gas. The hydrogen consumption was then obtained by subtracting the final amount of hydrogen from the initial value, providing the total moles of H_2 consumed during the reaction (Equation (**16**)):

$$nH_2, consumed \; = \; nH_2, start - \; nH_2, end \tag{16}$$

The number of moles of gas N is determined using the ideal gas law equation (**17**) using the pressure at room temperature:

$$nH_2 = \frac{PV}{RT} \tag{17}$$

where: *n* is the number of moles of gas, *P* is the pressure indicated in the reactor in bar, *V* is the volume of the reactor (0.16 L), *R* is the universal gas constant (0.0831

$L \cdot bar \cdot K^{-1} \cdot mol^{-1}$), and *T* is the temperature at which the data is collected, measured in Kelvin (K).

The distribution of functional groups in the products as well as in the feedstock were obtained by ^{1}H-NMR. ^{1}H-NMR analysis was performed using a Bruker Biospin spectrometer operating at 250 MHz (5.47 T magnet). Approximately 100 mg of each sample was dissolved in 1 mL of CD_3OD, containing TMSP-d_4 (sodium 3-trimethylsilyl-2,2',3,3-tetradeutero-propionate, ~2 g/L) (Sigma Aldrich, 99.8 at.% D) as an internal standard. The samples were then centrifuged and analyzed at 25 °C.

^{1}H-NMR data processing was conducted using MestReNova (version 9.0). Spectra were recorded using a 90° pulse program (4.95 μs) with the following acquisition parameters: acquisition time 10 s, relaxation delay 1.0 s, number of scans 24, spectral width 3255.2 Hz, and time domain 32k.

The use of an internal standard allowed the conversion of integrated signals into moles of protons [111], enabling direct comparison between samples with varying hydrogen content. Spectral integration was performed for different regions characteristic of specific functional groups [112], as summarized in Table 3.

TABLE 3 Integration regions of ^{1}H-NMR spectra and proton assignments to functional groups

Integration Range (ppm)	Proton Assignment
10.1 – 9.5	Aldehydes
8.5 – 6.0	(Hetero-)aromatic compounds
6.0 – 4.3	Carbohydrates, water, O–H exchanging groups
4.3 – 3.0	Alcohols, ethers, alkenes
3.0 – 1.5	α-protons adjacent to carboxylic acids, keto groups, or unsaturated systems
1.5 – 0.5	Alkanes

3.3.4. HDO OF GUAIACOL IN LIQUID CONTINUOUS PHASE

The continuous trickle bed reactor system is depicted in Figure 10, with a simplified flow diagram presented in Figure 11.Figure 11. The reactor setup is designed to process up to 2.4 L/h of pyrolysis oil (feedstock) and accommodate a hydrogen flow rate of up to 1000 L/h. The feedstock, stored in the EH01 reservoir, is heated to between 40 and 60 °C before being pumped for circulation. Nitrogen is used to purge oxygen from the system, ensuring a thorough purge by flushing compressor dead spaces with low-pressure nitrogen for 2 to 3 minutes. The system can handle approximately 800 L/h of scrubbing gas.

FIGURE 11. HDO Continuous Reactor and all the Components. a) Pilot HDO Plant b) Continuous Reactor Assembled c) Catalyst bed

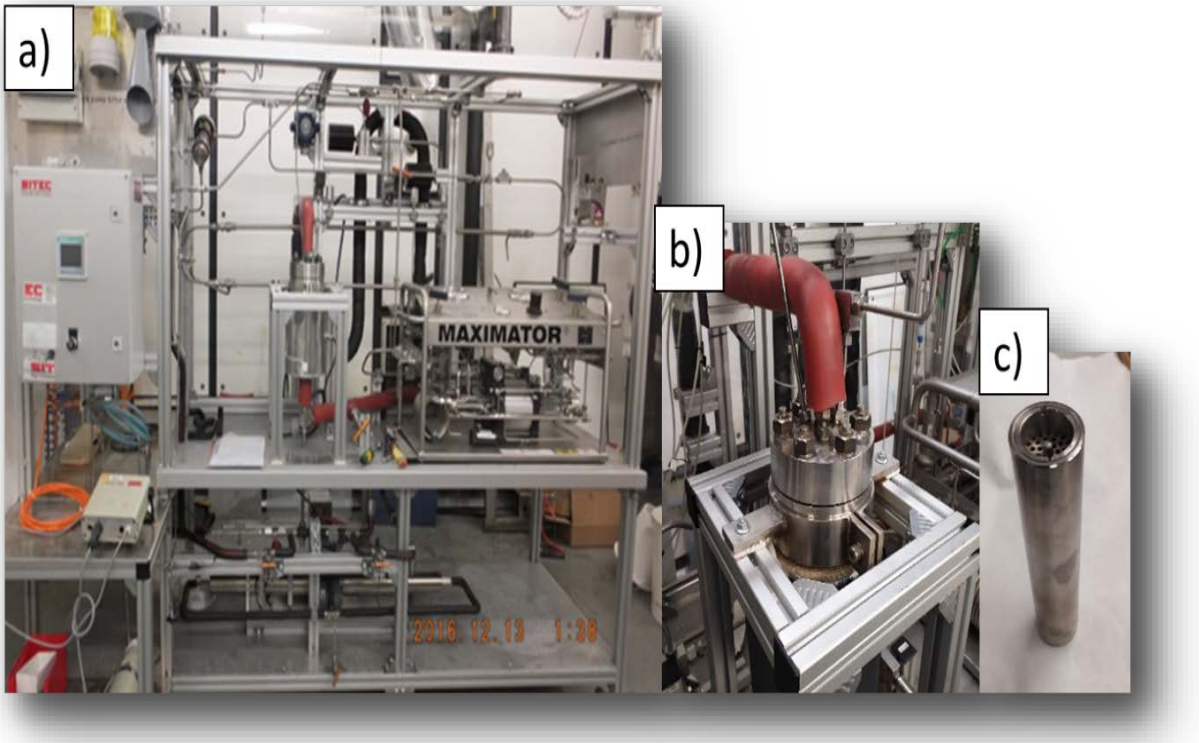

Electric heaters are employed to introduce heat into the preheater EH02 and reactor EH01. The temperature increase is carefully controlled by a temperature controller utilizing a ramp function, ensuring it does not exceed 100 °C/h. Once the system is sealed at the desired operating pressure and reaches the specified operating temperature, nitrogen is replaced by hydrogen. The feedstock is then mixed (MX) into the hydrogen before reaching the preheater.

Within the PC 01 trickle bed reactor, the feedstock reacts over the catalyst bed. The temperature across the bed is monitored to manage the exothermic hydrodeoxygenation reactions effectively. If the reaction temperature rises, the heat input from the preheater is reduced. The reaction mixture, cooled to between 30 and 80 °C, exits through the WT02 twin-tube cooler and then moves to an expansion vessel and a product receiver for separation. It then passes through an expansion vessel into the product receiver, separating the liquid hydrogenation product from the reaction gases. The treated product is collected in a reservoir, available for withdrawal post-test, while

gases are vented through a roofline. Gas emissions are quantified, and a gas mouse connection is used for storing the gas for analysis.

FIGURE 12. Gas mouse used to store the gases collected post reaction.

Process control is managed through both local and remote sensors, with a straightforward control system in place for monitoring and recording measurements, setting control targets, establishing alarm thresholds, and activating interlocks.

The reactor's conditions were specifically set for a feedstock flow rate of 300 mL/h (using a 10% GUA solution consisting of guaiacol and decalin) and a hydrogen flow rate of 0.4 mol/h, maintaining an optimal H_2/GUA ratio of 2. The catalyst bed in the reactor was prepared with 8 g of catalyst dispersed in silica pellets (sourced from Alfa-Aesar), filling a 200 mL volume. The weight hourly space velocity (WHSV) was set at 3 h^{-1}, with the operating temperature maintained at 300°C and under a hydrogen pressure of 30 MPa. To prevent overheating and ensure efficient hydrodeoxygenation, the reaction temperatures were continuously monitored.

Before injecting guaiacol, the catalyst underwent a reduction process — Ruthenium catalysts at 350 °C and Ni-Fe catalysts at 500 °C — for 3 hours under a hydrogen pressure of 200 bar. The initial 100 mL of feed was employed to purge the system and was subsequently discarded.

FIGURE 13. Schematic of plant Pilot at KIT, IKFT

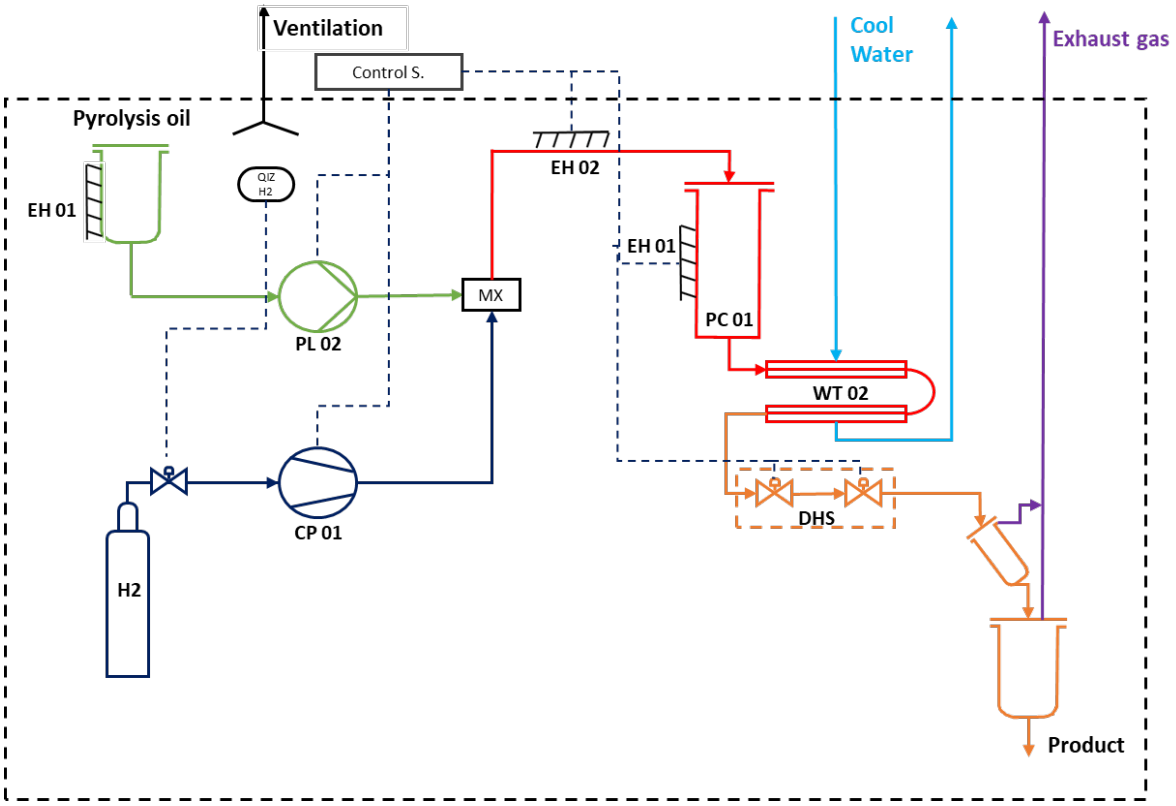

To conclude, the characterization of the products using GC-MS for liquid (condensed) products and GC-FID/TCD for gases was consistent with the methods employed in our previous topic on the hydrodeoxygenation (HDO) reaction of guaiacol.

CHAPTER 4

STUDY OF Ni-Fe CATALYSTS SUPPORTED ON Nb_2O_5 FOR ENHANCED HYDRODEOXYGENATION

4.1. MOTIVATION

This chapter explores the role of Nb_2O_5 as a catalyst support in the hydrodeoxygenation (HDO) of guaiacol, building upon prior investigations conducted in both gas and liquid phases. Our research group at Federal University of Uberlandia (UFU) has extensively studied the gas-phase HDO of guaiacol, evaluating the effects of key operating parameters—such as hydrogen partial pressure, temperature, and space velocity—on catalytic activity and product selectivity. One of the major findings was the direct correlation between the niobia content in Nb_2O_5-Al_2O_3 mixed supports and an enhanced yield of phenol, emphasizing the strong influence of the support material on deoxygenation pathways [32]. Notably, in the gas-phase studies, Pt/Nb_2O_5 exhibited superior performance due to the effective interaction between Pt and NbOx species at the metal-support interface, underscoring the oxophilic nature of niobia in promoting selective deoxygenation [32].

While the gas-phase findings provided valuable insights into support effects and metal-support interactions, the transition to liquid-phase HDO introduces new challenges and opportunities, particularly in understanding the behavior of non-noble metal catalysts under different reaction environments. At Karlsruhe Institute of Technology (KIT), this study builds upon the fundamental knowledge acquired in gas-phase HDO to investigate the performance of Ni–Fe catalysts supported on Nb_2O_5 in the liquid phase, aiming for more cost-effective alternatives to noble metal catalysts while maintaining high activity, selectivity, and stability. Nickel-based catalysts were chosen for their well-documented hydrogenation activity and affordability, while iron was incorporated for its potential to enhance deoxygenation selectivity and overall catalyst performance [113]. In this context, Nb_2O_5 was evaluated as a support for the Ni–Fe system, with SiO_2 included for comparison, allowing a deeper understanding of how these supports influence catalytic behavior.

Given the versatile properties of Nb_2O_5 and its emerging role in catalysis, this work seeks to establish correlations between its physicochemical characteristics and catalytic performance in HDO. The study first conducted catalyst screening at 300°C to identify the most promising formulation, according to the literature [18,20,24,114], the optimal temperature range for Ni–Fe catalysts in HDO reactions is between 250°C and 350°C. Followed by a detailed evaluation at 250°C, 300°C, and 350°C with the best-performing catalyst to determine optimal operating conditions. By integrating knowledge from gas-phase studies at UFU with liquid-phase investigations at KIT, this chapter contributes to the ongoing advancement of Nb_2O_5-supported catalysts for HDO applications, bridging fundamental research with practical catalytic developments.

4.2 EXPERIMENTAL METHODS (Summary)

The synthesis, characterization, and catalytic evaluation of Ni-Fe catalysts supported on Nb_2O_5 and SiO_2 were conducted following the detailed procedures outlined in Chapter 3. Analytical techniques were employed to assess the physicochemical properties of the catalysts, including elemental analysis via ICP–OES, textural properties via N_2 adsorption-desorption (BET method), crystallinity via XRD, and metal dispersion via H_2-TPD. Additionally, temperature-programmed reduction (TPR) and NH_3-TPD were utilized to evaluate the reducibility and acidity of the catalysts, respectively. Surface composition was analyzed via X-ray photoelectron spectroscopy (XPS) to understand metal oxidation states and interactions with the support.

For the hydrodeoxygenation (HDO) tests, guaiacol was used as a model compound in a 200 mL batch reactor under liquid-phase conditions. Each experiment involved 25 g of guaiacol and 1–2 g of pre-reduced catalyst, conducted at 300°C for 3 hours under 5 MPa of H_2 with vigorous stirring (800 rpm). The upgraded liquid products were collected and analyzed via gas chromatography (GC-FID), with conversion and selectivity calculated accordingly. A temperature variation study was also performed at 250, 300, and 350°C to assess the impact of temperature on catalyst performance.

4.3. RESULTS AND DICUSSION

4.3.1. CATALYST CHARACTERIZATION

N2 Physisorption

The N_2 physisorption isotherms (75 K) of the supports are shown in Figure 14, with surface area, pore volume, and average pore diameter values provided in Table 4. According to the classification by the International Union of Pure and Applied Chemistry (IUPAC) [115], all the catalysts, except for SiO_2, exhibited standard type IV isotherms. These type IV isotherms, which are commonly found in heterogeneous catalysts, are indicative of multilayer adsorption and capillary condensation within mesoporous materials, as described by Schmal et al. (2016) [[105]. This behavior is typically associated with materials possessing cylindrical pores formed by agglomerates of spheroidal particles with varying sizes and shapes [116]. The isotherms also feature a narrow hysteresis loop extending to very high relative pressures, close to 0.99, which suggests the presence of large mesopores between the particles. In contrast, the SiO_2 support displayed a type III isotherm, characteristic of weaker gas–solid interactions, as noted in earlier studies [116].

Among the supports, niobium oxide (Nb_2O_5) calcined at 500 °C had the lowest specific surface area (33.2 m^2/g), see in Table 4. Elemental composition (determined by ICP-OES), textural properties (as determined by N_2 physisorption)Table 4, similar to that reported by Zhang et al. and Campos Fraga et al. [117,118]. In contrast, the calcined SiO_2 support had a specific surface area of 45.2 m^2/g, which was slightly smaller than the surface area of SiO_2 before calcination (50 m^2/g) provided by the supplier. Notably, niobic acid (HY-340, $Nb_2O_5.nH_2O$), i.e., the Nb_2O_5 precursor, had a significantly greater specific surface area of approximately 160 m^2/g, but calcination at 500°C led to a substantial reduction in the surface area. Furthermore, the incorporation of metallic phases into the supports decreased the BET surface area due to the partial blockage of pores by the metallic particles, particularly in the Nb_2O_5-supported catalysts.

TABLE 4. Elemental composition (determined by ICP-OES), textural properties (as determined by N_2 physisorption).

	Composition by ICP (wt. %)			
Samples	**Ni (wt. %)**	**Fe (wt. %)**	**S_{BET} ($m^2 \cdot g^{-1}$)**	**V_p ($cm^3 \cdot g^{-1}$)**
Nb_2O_5 (500°C)	0	0	33.2	0.15
$5Fe/Nb_2O_5$	0	4.9	32.8	0.1
$5Ni/Nb_2O_5$	4.9	0	24.5	0.09
$5Ni1Fe/Nb_2O_5$	5	1.0	42.9	0.12
$5Ni5Fe/Nb_2O_5$	4.9	4.9	41.9	0.12
SiO_2 (500°C)	0	0	45.2	0.1
$5Fe/SiO_2$	0	4.7	42.1	0.12
$5Ni/SiO_2$	4.3	0	36.9	0.1
$5Ni1Fe/SiO_2$	4.4	0.9	44.5	0.1
$5Ni5Fe/SiO_2$	4.5	4.9	42.5	0.12

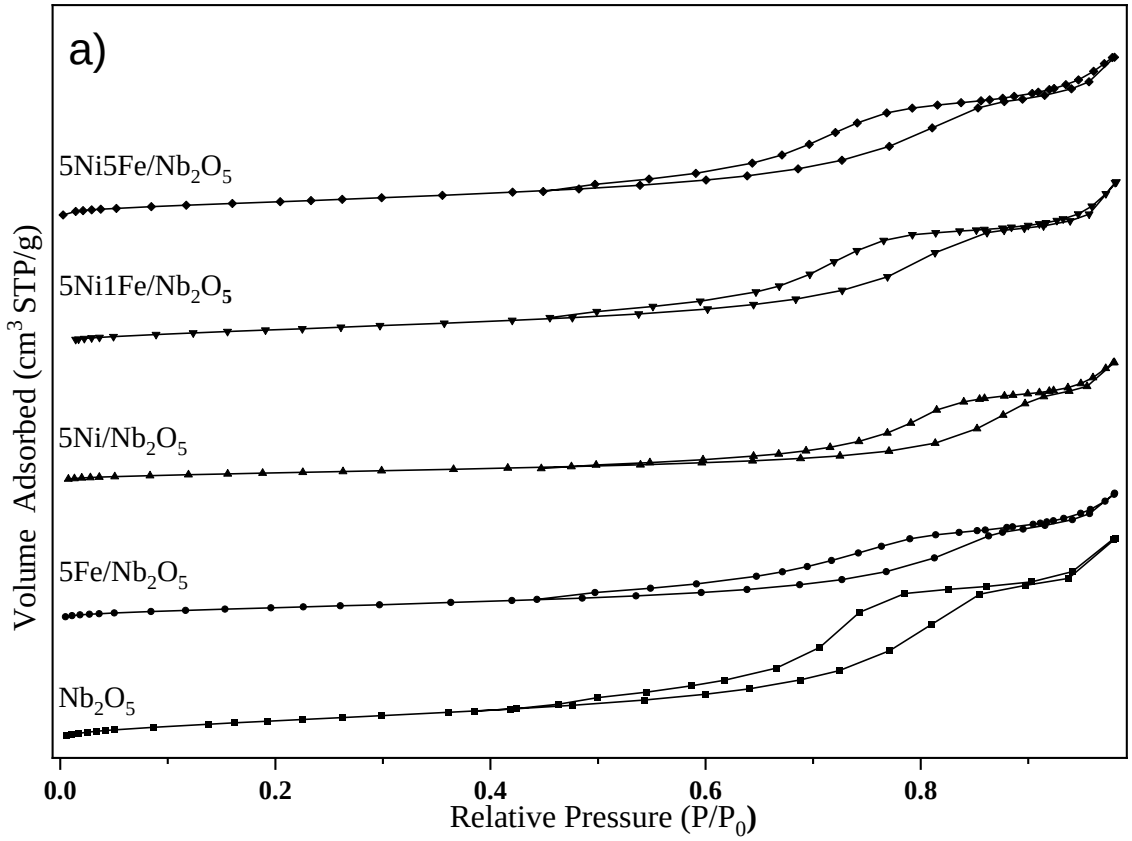
a)
5Ni5Fe/Nb2O5
5Ni1Fe/Nb2O5
5Ni/Nb2O5
5Fe/Nb2O5
Nb2O5
Volume Adsorbed (cm3 STP/g)
0.0
0.2
0.4
0.6
0.8
Relative Pressure (P/P0)

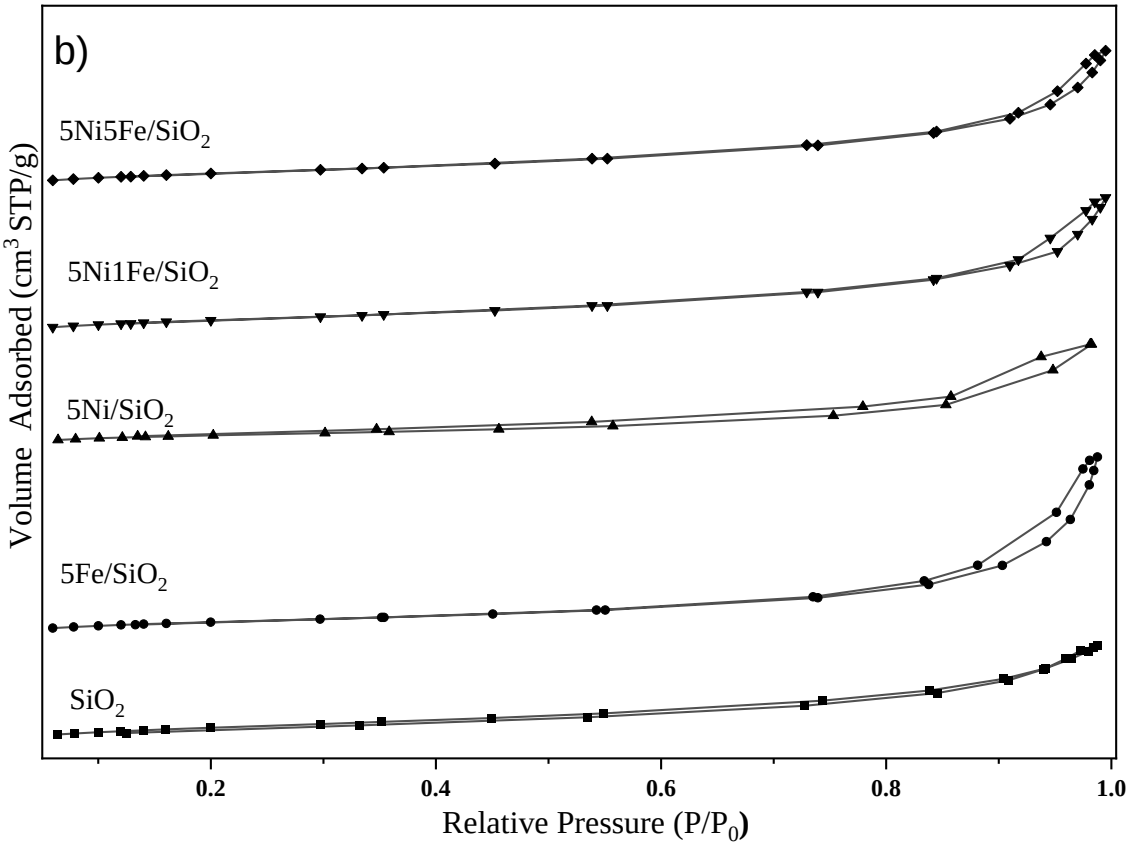
b)
5Ni5Fe/SiO2
5Ni1Fe/SiO2
5Ni/SiO2
5Fe/SiO2
SiO2
Volume Adsorbed (cm3 STP/g)
0.2
0.4
0.6
0.8
1.0
Relative Pressure (P/P0)

FIGURE 14 Textural properties of the SiO_2 and Nb_2O_5 supports and the Ni–Fe-supported catalysts.

X-ray Diffraction

The X-ray diffraction (XRD) patterns for the reduced and passivated catalysts are shown in Figure 15. Silica can exist in either crystalline or amorphous forms, depending on its treatment [119]. In this study, even after the reduction and passivation processes, the support remained amorphous, as indicated by the broad, diffuse band observed at 2θ of approximately 22°, which is characteristic of amorphous silica and consistent with the standard pattern ICSD 176.

With respect to Nb_2O_5, the observed primary structure after calcination was TT-Nb2O5, characterized by a hexagonal lattice, with a prominent peak at 2θ = 28.6°, which is consistent with ICSD 1840. The TT-Nb_2O_5 structure, wherein niobium atoms are arranged to create a symmetrical atomic site within an open unit cell, points to a nonstoichiometric composition, specifically $Nb_{16}O_{42}$ [120]. This nonstoichiometric, indicative of an open and adaptable atomic structure, is crucial for the effective impregnation of metal species and their interaction with reactant molecules. The successful formation of the TT-Nb_2O_5 structure, as corroborated by the literature [117,120,121], underscores the importance of controlling the calcination temperature in the preparation of niobia-supported catalysts.

For the calcined monometallic samples containing Ni on both supports, a distinct NiO peak was detected at 2θ = 43.3° (ICSD 9866). After the reduction process, the presence of metallic Ni was confirmed by peaks at 2θ = 44.49°, corresponding to the (111) and (200) planes, as referenced by ICSD 043397. This phase was observed on both supports. Peaks corresponding to NiFe (111) and NiFe (110) appeared at 2θ = 43.7° and 50.9°, respectively, in the reduced bimetallic catalysts. Progressive shift in the NiFe(111) peak towards lower 2θ values was observed as the Fe content increased. Specifically, the 5Ni1Fe catalyst (1% Fe) exhibited its NiFe(111) peak at a slightly higher 2θ value compared to 5Ni5Fe (5% Fe), which showed a further shift toward lower 2θ values. This trend is consistent with previous studies on NiFe alloys, where increasing Fe incorporation into the Ni lattice leads to a decrease in 2θ values and an expansion of the lattice parameter due to the slightly larger atomic radius of Fe

compared to Ni. Similar behavior has been observed in NiFe/TiO_2 catalysts, where the Ni (111) peak shifted from 2θ = 44.43° (0% Fe) to 44.29° (5% Fe) as Fe content increased [122].

The analysis of Fe species reveals that the presence of Ni significantly enhances the reduction of iron, as demonstrated by the XRD patterns of the 5Ni5Fe/Nb_2O_5 catalyst, which show the formation of metallic iron (Fe^0) at 2θ = 44.67° (ICSD 64998). In contrast, for the monometallic samples, the reduction conditions were only sufficient to convert Fe^{3+} to Fe^{2+}. This indicates that Ni facilitated the complete reduction of Fe_2O_3 to Fe_3O_4 and subsequently to Fe^0. The promoting effect of Ni on Fe reduction can be attributed to the hydrogen spillover effect, whereby hydrogen atoms are transferred from Ni to adjacent iron oxide species, accelerating the overall reduction process

TABLE 5 Crystallite Size (τ) (nm) of the catalyst

	Crystallite size (τ) (nm)					
Sample	NiO	Fe_3O_4	Fe_2O_3	NiFe	Ni	Fe
5Fe/Nb_2O_5	-	117	-	-	-	-
5Ni/Nb_2O_5	-	-	-	-	116	-
5Ni1Fe/Nb_2O_5	-	-	-	21.8	-	-
5Ni5Fe/Nb_2O_5	-	-	-	37.8	-	38
5Fe/SiO_2	-	49.4	36.3	-	-	-
5Ni/SiO_2	77.8	-	-	-	32	-
5Ni1Fe/SiO_2	-	-	-	68.1	-	-
5Ni5Fe/SiO_2	-	-	-	66.2	-	33

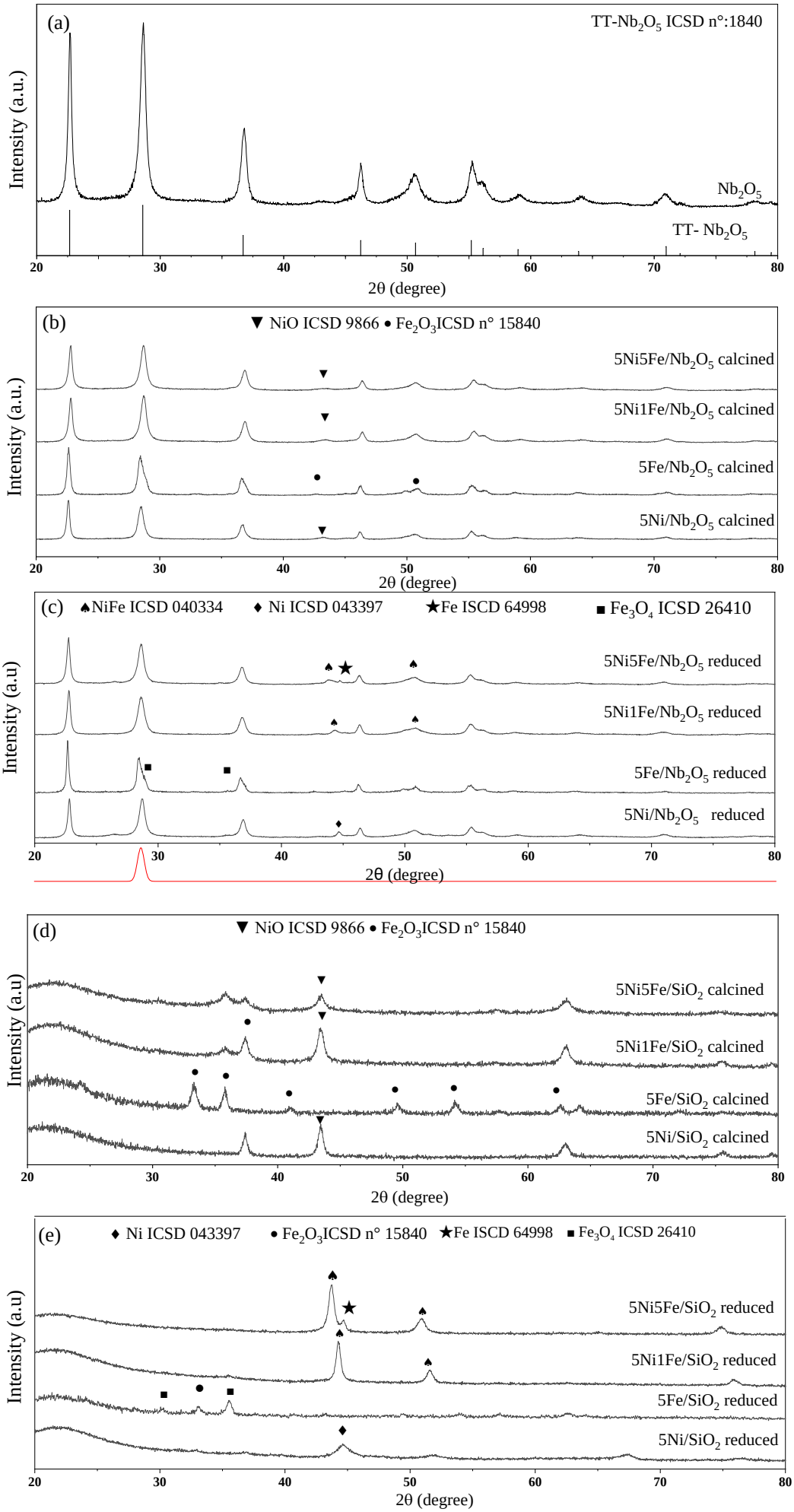
(a)
TT-Nb2O5 ICSD n°:1840
Intensity (a.u.)
Nb2O5
TT- Nb2O5
20
30
40
50
60
70
80
2θ (degree)
(b)
▼ NiO ICSD 9866 • Fe2O3ICSD n° 15840
5Ni5Fe/Nb2O5 calcined
5Ni1Fe/Nb2O5 calcined
5Fe/Nb2O5 calcined
5Ni/Nb2O5 calcined
Intensity (a.u.)
2θ (degree)
(c)
♠NiFe ICSD 040334
♦ Ni ICSD 043397
★Fe ISCD 64998
■ Fe3O4 ICSD 26410
5Ni5Fe/Nb2O5 reduced
5Ni1Fe/Nb2O5 reduced
5Fe/Nb2O5 reduced
5Ni/Nb2O5 reduced
Intensity (a.u)
2θ (degree)
(d)
▼ NiO ICSD 9866 • Fe2O3ICSD n° 15840
5Ni5Fe/SiO2 calcined
5Ni1Fe/SiO2 calcined
5Fe/SiO2 calcined
5Ni/SiO2 calcined
Intensity (a.u)
2θ (degree)
(e)
♦ Ni ICSD 043397
• Fe2O3ICSD n° 15840
★Fe ISCD 64998
■ Fe3O4 ICSD 26410
5Ni5Fe/SiO2 reduced
5Ni1Fe/SiO2 reduced
5Fe/SiO2 reduced
5Ni/SiO2 reduced
Intensity (a.u)
2θ (degree)

FIGURE 15 XRD patterns of the xNi-yFe catalysts with varying metal loadings. (a) Nb_2O_5 support, (b) calcined Nb_2O_5-supported catalysts, (c) reduced Nb_2O_5-supported catalysts, (d) calcined SiO_2-supported catalysts, and (e) reduced SiO_2-supported catalysts.

Temperature-programmed reduction (TPR)

The reducibility profiles of the catalysts, as shown in Figure 16, revealed distinct behaviors for the two different supports. For the $5Fe/Nb_2O_5$ catalyst, the initial peak at approximately 277 °C corresponded to the reduction of Fe_2O_3 (Fe^{3+}) to Fe_3O_4 (Fe^{2+}, Fe^{3+}). A subsequent peak at approximately 485 °C indicates the reduction of Fe_3O_4 to metallic Fe (Fe^0) through hydrogen absorption [123]. In contrast, the $5Fe/SiO_2$ catalyst exhibited a different reduction pattern (see Figure 16 b), in which Fe_2O_3 had a higher reduction temperature. This suggests that iron is more easily reduced on Nb_2O_5 than on SiO_2. For comparison, a TPR was also performed with a physical mixture of Fe_2O_3 and Nb_2O_5, and in this case, iron reduction occurred between 330 °C and 770 °C. As shown in Figure 16–c, two distinct reduction peaks were detected: one at 383°C, corresponding to the reduction of Fe_2O_3 to Fe_3O_4, and the other at 638°C, representing the conversion of Fe_3O_4 to metallic Fe (Fe°). This reduction profile is consistent with findings reported in the literature for iron reduction [122,124,125].

For the $5Ni/Nb_2O_5$ catalyst, two reduction peaks were observed. The first peak near 464 °C was attributed to the reduction of bulk NiO, whereas the second peak at 670 °C corresponded to the reduction of larger NiO particles and nickel niobate ($NiNb_2O_6$), which are compounds formed during the calcination of the catalysts. Fang et al. (2017) [87] reported that the shoulder peak in the reduction of Ni-based catalysts is associated with the reduction of larger, less dispersed NiO particles. The interaction between nickel and Nb_2O_5 increased the reduction temperature of Ni, as reported in previous studies [121]. In agreement, the shift in the reduction peak observed for the catalyst compared with the TPR of a physical mixture of NiO and Nb_2O_5 points to the presence of a stronger metal–support interaction (SMSI) between the nickel particles and Nb_2O_5 [126]. This shift indicates the presence of Ni^{2+} species that can be easily reduced owing to the presence of oxygen vacancies on the bimetallic catalyst.

Additionally, beyond the interaction between the support and the metals, interactions between Ni and Fe were observed in the 5Ni5Fe/Nb_2O_5 and 5Ni1Fe/Nb_2O_5 catalysts. These bimetallic catalysts demonstrated lower reduction temperatures than their monometallic counterparts and exhibited two distinct reduction peaks. This behavior suggests the formation of a Ni_xFe_y alloy, whose properties are significantly influenced by the Ni/Fe ratio and perform optimally within a specific compositional range, as supported by previous studies [27,125]. Conversely, when SiO_2 was used as the support, the addition of iron induced a shift toward higher Ni reduction temperatures, reflecting the characteristics of the Fe reduction profile. This trend was evident in both the 5Ni1Fe and 5Ni5Fe/SiO_2 catalysts and can be attributed to the reduction of FeO, facilitated by the Ni–Fe alloy structure. This behavior aligns with the reduction profile of NiO-FeO_x /$MgAlO_x$-1 reported by Huang et al. in (2022) [24].

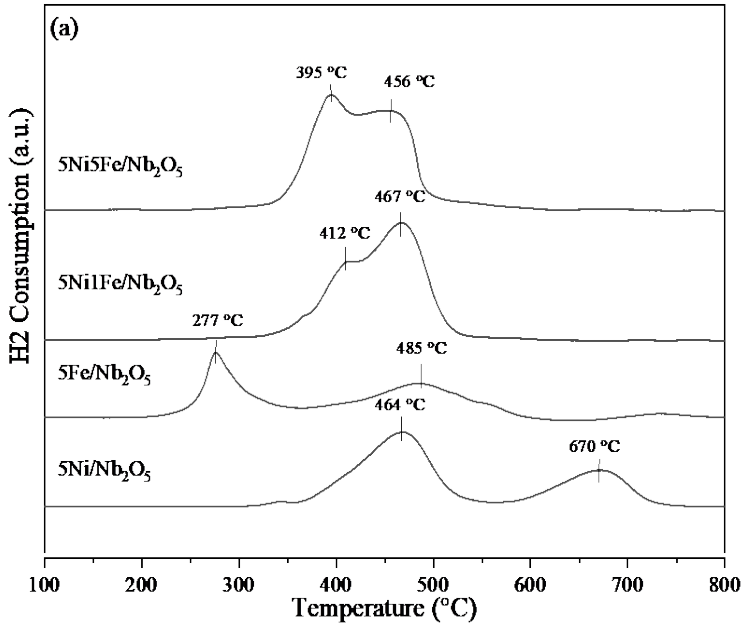
(a)
395 °C
456 °C
5Ni5Fe/Nb2O5
467 °C
412 °C
5Ni1Fe/Nb2O5
277 °C
485 °C
5Fe/Nb2O5
464 °C
670 °C
5Ni/Nb2O5
H2 Consumption (a.u.)
100
200
300
400
500
600
700
800
Temperature (°C)

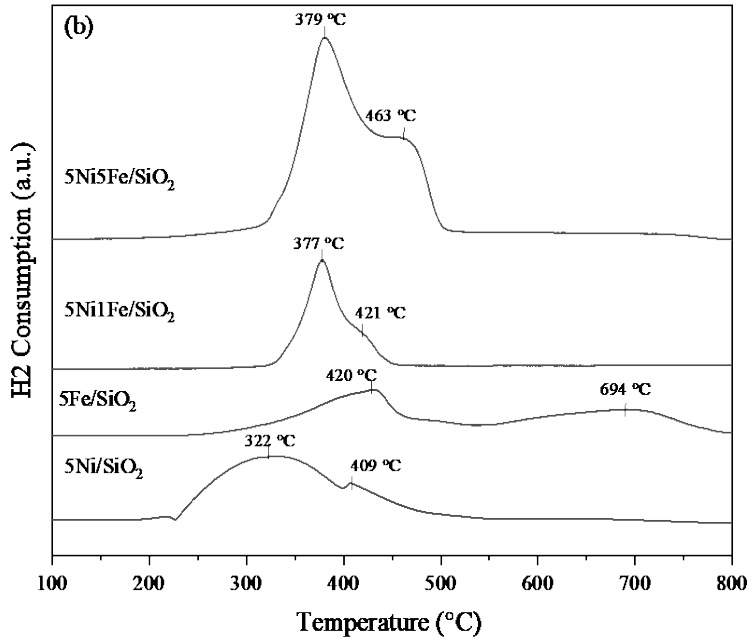
(b)
379 °C
463 °C
5Ni5Fe/SiO2
377 °C
421 °C
5Ni1Fe/SiO2
420 °C
694 °C
5Fe/SiO2
322 °C
409 °C
5Ni/SiO2
H2 Consumption (a.u.)
100
200
300
400
500
600
700
800
Temperature (°C)

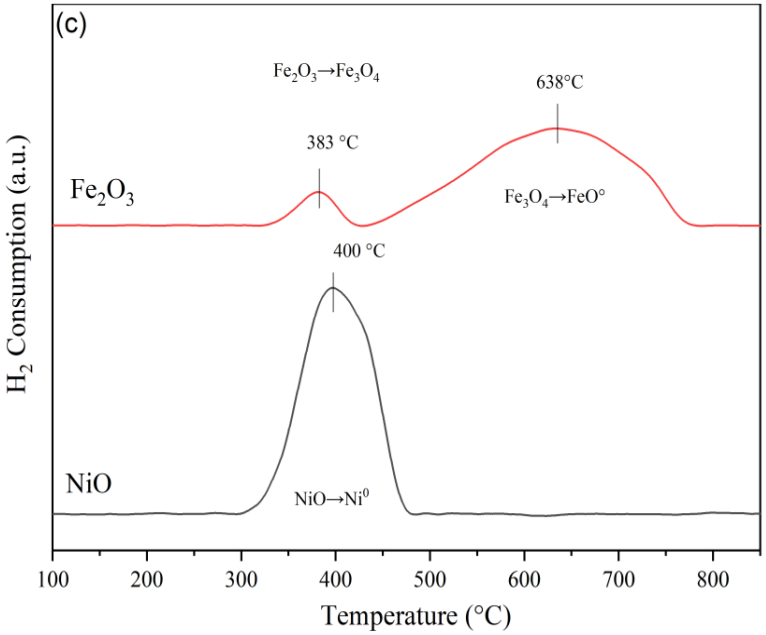
(c)
Fe2O3→Fe3O4
638°C
383 °C
Fe2O3
Fe3O4→FeO°
400 °C
NiO
NiO→Ni0
H2 Consumption (a.u.)
100
200
300
400
500
600
700
800
Temperature (°C)

FIGURE 16 TPR patterns for the xNi-yFe passivated catalysts with different metal loadings: (a) with the Nb_2O_5 support, (b) with the SiO_2 support and (c) physical mixtures of metal oxides and Nb_2O_5.

The H_2 consumption during catalyst reduction is summarized in Table 6. The monometallic catalysts resulted in constant H_2 uptake, whereas the differences were more pronounced between the bimetallic catalysts. Specifically, the 5Ni1Fe/Nb_2O_5 catalyst exhibited greater H_2 uptake (970.28 μmol g^{-1}) than did 5Ni1Fe/SiO_2 (719.37 μmol g^{-1}). In contrast, the H_2 uptake of 5Ni5Fe/SiO_2 (1313.50 μmol g^{-1}) was similar to that of 5Ni5Fe/Nb_2O_5 (1076.90 μmol g^{-1}). H_2 consumption is primarily due to the reduction of iron and nickel ions to their metallic states (Fe^0 and Ni^0). The notably higher consumption in the 5Ni1Fe/Nb_2O_5 sample than in the 5Ni1Fe/SiO_2 sample suggests that reducibility is closely linked to the dispersion of the catalysts Table 7. This trend in high-temperature reducibility is consistent with the observed catalytic performance, as discussed below.

TABLE 6 Hydrogen uptake and H_2/metal ratios for monometallic and bimetallic catalysts supported on Nb_2O_5 and SiO_2

Catalyst	Uptake (µmol . g cat^{-1})	H_2/Metal (Theorical)	H_2/Metal (Real)	Degree of reduction (%)
Ni/Nb2O5	572.5	1	0.68	68
Fe/Nb2O5	541.1	1.50	0.54	36
5Ni1Fe/Nb2O5	900	1.33	0.87	67
5Ni5Fe/Nb2O5	1076.9	1.33	0.43	40
5Ni/SiO2	697.62	1.00	0.82	82
5Fe/SiO2	626.42	1.50	0.69	46
5Ni1Fe/SiO2	693.7	1.33	0.69	52
5Ni5Fe/SiO2	1313.5	1.33	0.45	60

Hydrogen Temperature-Programmed Desorption (H_2-TPD)

The H_2-TPD results, presented in FIGURE 17, and the corresponding quantitative values in Table 7, illustrate how the support material and metal composition influence hydrogen adsorption capacity and dispersion. For monometallic catalysts, where the primary interaction is between the metal and the support, the H_2 uptake was significantly higher for SiO_2-supported catalysts compared to Nb_2O_5-supported ones. Specifically, 5Ni/SiO_2 exhibited the highest hydrogen adsorption (133 µmol/g), followed by 5Fe/SiO_2 (93.7 µmol/g), whereas 5Ni/Nb_2O_5 (36.0 µmol/g) and 5Fe/Nb_2O_5 (21.3 µmol/g) showed lower values. This trend is consistent with the higher dispersion of Ni on SiO_2 (19.3%), as weak metal-support interactions prevent excessive particle growth, yielding smaller Ni particle sizes (5.2 nm for 5Ni/SiO_2). On the other hand, Nb_2O_5-supported monometallic catalysts showed lower dispersion (8.4% for

5Ni/Nb_2O_5), resulting in larger Ni particles (11.9 nm) due to stronger metal-support interactions that promote particle agglomeration.

For bimetallic catalysts, where Ni-Fe interactions introduce additional effects beyond metal-support interactions, different trends were observed. In Nb_2O_5-supported bimetallic catalysts, H_2 uptake decreased with increasing Fe content, with 5Ni1Fe/Nb_2O_5 adsorbing 30.4 µmol/g and 5Ni5Fe/Nb_2O_5 dropping to 18.3 µmol/g. Despite smaller crystallite sizes in XRD results Table 5, the lower H_2 adsorption suggests that Fe may have migrated into the bulk phase, limiting available Ni sites for hydrogen adsorption. This aligns with findings from Cheng et al. (2020), where Fe incorporation led to reduced metal dispersion and fewer accessible hydrogen adsorption sites due to Fe migration into the bulk [127].

A different trend was observed in SiO_2-supported bimetallic catalysts, where stronger Ni-Fe interactions resulted in higher desorption temperatures. The 5Ni1Fe/SiO_2 catalyst exhibited a broad desorption peak at 580°C, suggesting stronger electronic interactions between Ni and Fe. This effect was even more pronounced in 5Ni5Fe/SiO_2, indicating that SiO_2 facilitated stronger Ni-Fe interactions compared to Nb_2O_5, leading to higher desorption temperatures and stronger adsorption sites.

Table 7 H_2 uptake, metal dispersion (Dp%), and Ni particle size for the studied catalysts. The H_2 uptake values were obtained from H_2-TPD analysis, while dispersion and particle size were calculated based on the H_2 chemisorption method.

Catalyst	H_2 (µmol/g)	Dp (%)	Ni Particle Size (nm)
5Ni/Nb_2O_5	36	8.4	11.9
5Fe/Nb_2O_5	21.3	-	N/A
5Ni1Fe/Nb_2O_5	30.4	13.8	18.2
5Ni5Fe/Nb_2O_5	18.3	14.2	15.5
5Ni/SiO_2	133	19.3	5.2
5Fe/SiO_2	93.7	-	N/A
5Ni1Fe/SiO_2	34	6.1	16.6
5Ni5Fe/SiO_2	100.9	10.1	10

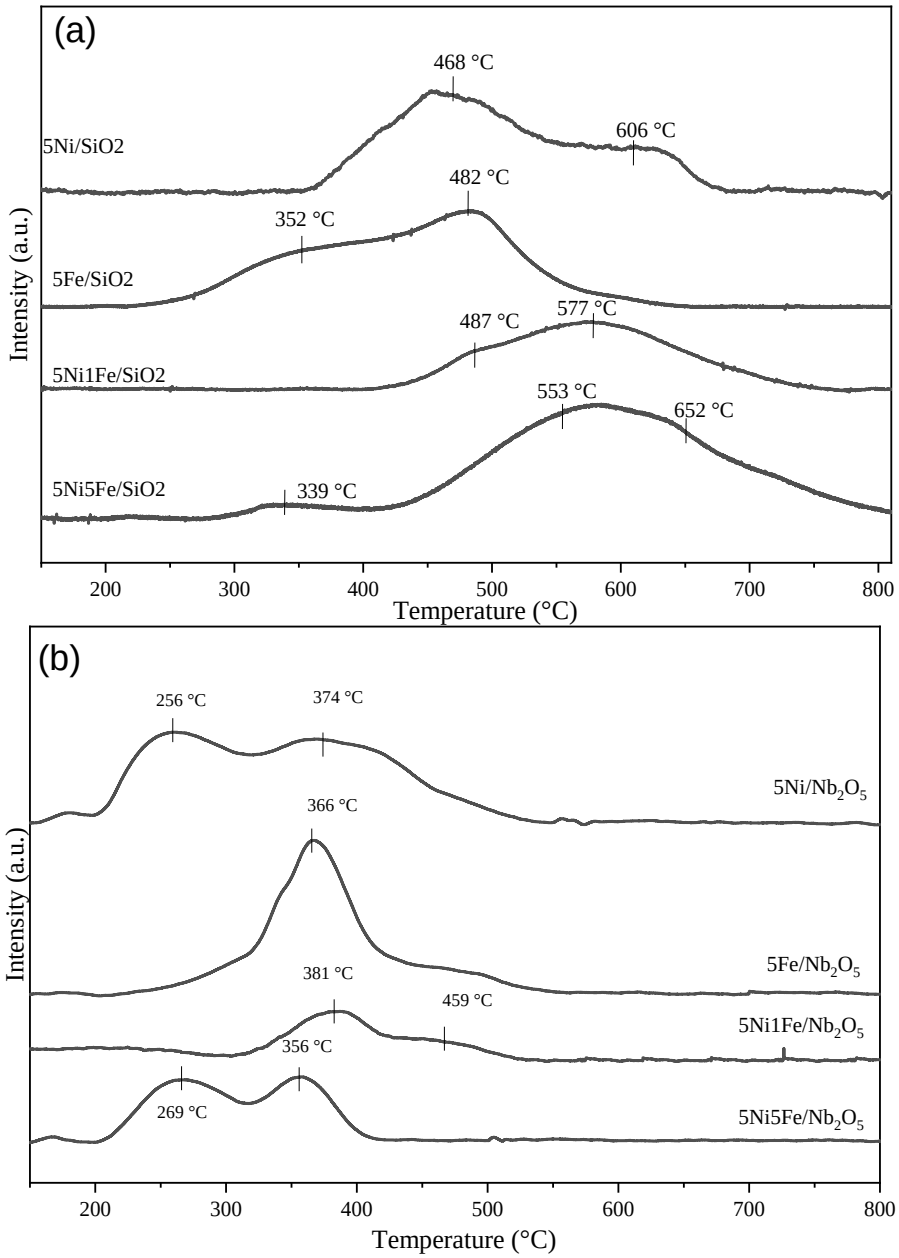

FIGURE 17 Hydrogen temperature-programmed desorption (H_2-TPD) profiles of Ni-Fe catalysts supported on Nb_2O_5 and SiO_2.

Ammonia temperature-programmed desorption (NH_3-TPD)

The density of acid sites in the catalysts was determined via NH_3-TPD, and the desorption profiles are shown in FIGURE 18. The Nb_2O_5-supported catalysts exhibited pronounced peaks, reflecting their inherent acidity. In contrast, the SiO_2-supported catalyst (Ni/SiO_2) had almost no NH_3 desorption, suggesting minimal acidity. This

observation is corroborated by Campos Fraga (2022) [102]. The profiles, spanning temperatures from 200 to 600°C, revealed the existence of acid sites varying in strength, categorized as weak (T < 249.85°C), medium (249.85°C < T < 319.85°C), and strong (T > 319.85°C), on the basis of the temperature range over which ammonia desorption occurs [43]. The presence of multiple peaks within the profiles indicates the presence of acid sites of differing strengths.

The catalysts analyzed presented only medium and strong acid sites, whose densities and distributions are comprehensively detailed in TABLE 8. Compared with its counterpart 5Ni/Nb_2O_5, the monometallic 5Fe/Nb_2O_5 exhibited only strong acid sites but a lower total acidity. The addition of Fe to 5Ni/Nb_2O_5 led to a reduction in acidity, likely due to the partial occupation or blockage of the acid sites originally present on the Nb_2O_5 support by iron species. This phenomenon is consistent with findings reported by Wang et al. (2022) [128], where increasing Fe doping in a Ce-La oxide system led to significant changes in the NH_3 desorption profile and an increase in overall acidity up to an optimal Fe content. Beyond this point, further Fe addition resulted in structural modifications that altered the acid site distribution and intensity. Similarly, in our case, the further reduction in acidity with increasing Fe content can be attributed to disruption of the support's intrinsic acid sites or dilution of the active Ni species, impairing the synergistic metal–support interaction.

Table 8 Total ammonia desorption and the distribution of acid sites (medium and strong) for various catalysts supported on Nb_2O_5 and SiO_2.

Sample	Ammonia desorbed ($\mu mol/g_{cat}$)	Acid sites distribution (%)	
		Medium	Strong
5Fe/Nb_2O_5	312	-	100
5Ni/Nb_2O_5	309	27	73
5Ni1Fe/Nb_2O_5	274	25	75
5Ni5Fe/Nb_2O_5	295	30	70
Nb_2O_5	668	25	75
5Ni/SiO_2	7	-	-

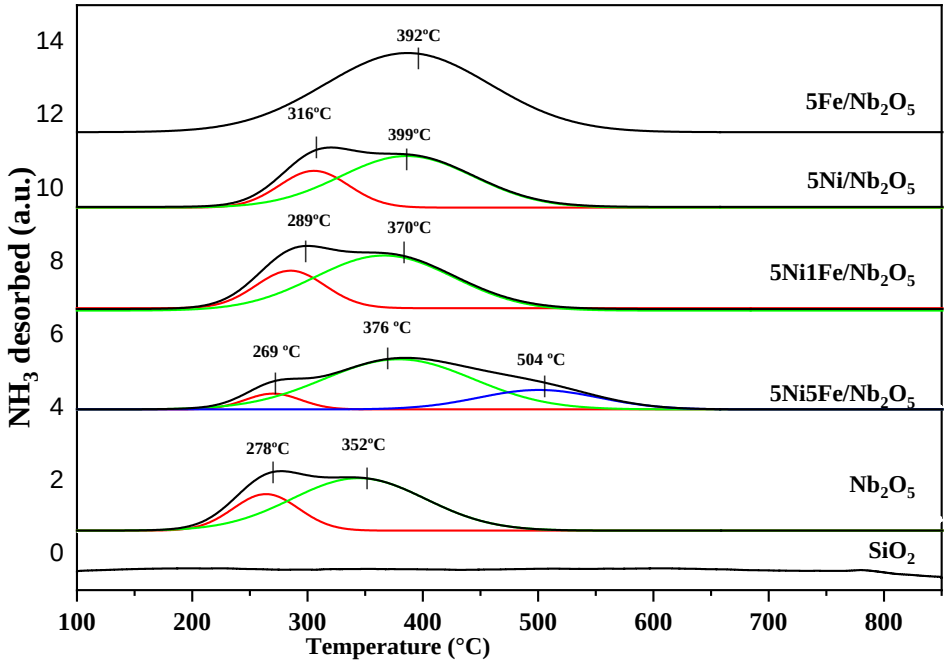

FIGURE 18 Ammonia temperature-programmed desorption (NH_3-TPD) profiles of the Nb_2O_5-supported catalysts.

X-ray photoelectron spectroscopy (XPS)

XPS analysis was performed to examine the surface species and the reduction states of Ni and Fe in the catalysts. All XPS peaks were identified on the basis of an online database (https://srdata.nist.gov/xps/) and published data from the literature. The spectra of the analyzed catalysts are shown in Figure 19.

The Ni 2p spectra of 5Ni1Fe/Nb_2O_5 and 5Ni5Fe/Nb_2O_5, along with the Fe 2p spectra of 5Ni5Fe/Nb_2O_5, exhibit broad and overlapping peaks, indicating the presence of multiple Ni species with different oxidation states. The binding energy at 855.6 eV was attributed to Ni^{2+}, which is associated with $NiFe_2O_4$ [88,129] and NiO. Satellite peaks ranging from 857.1 to 859.9 eV further confirmed the presence of Ni^{2+} cations bound to oxygen [130]. Additionally, the peak at approximately 852.1 eV was assigned to metallic Ni^0, indicating the coexistence of oxidized and metallic Ni species.

Notably, no Fe 2p signal was observed for 5Ni1Fe/Nb_2O_5, indicating that Fe is not significantly present at the surface and is likely embedded within the bulk phase. In contrast, for 5Ni5Fe/Nb_2O_5, The Ni/Fe atomic ratio obtained via XPS (0.16) was significantly lower than the ratio determined by ICP–OES (0.94), suggesting that Fe is

more concentrated at the catalyst surface compared to Ni. Although thermodynamic predictions suggest that Ni tends to remain at the surface in NiFe alloys due to its higher cohesive energy, the lower Ni/Fe ratio observed by XPS compared to ICP-OES indicates surface enrichment of Fe, particularly at higher Fe loadings [127,131,132]. The formation of Ni–Fe alloys within Ni-rich domains likely explains the Fe incorporation into the catalyst structure, while any remaining Fe species may exist as oxides dispersed within the Ni-Fe nanoparticles. This distribution of Fe could modify the electronic properties and catalytic behavior of the material by influencing metal-support interactions and hydrogen activation sites.

The Fe 2p spectra of 5Ni5Fe/Nb_2O_5 revealed a prominent Fe^{3+} peak at 710.4 eV, indicative of abundant oxidized Fe species on the catalyst surface. The peaks at 724.0 eV (Fe $2p_{1/2}$) and 710.4–710.6 eV (Fe $2p_{3/2}$) were attributed to Fe^{3+} species, which is consistent with the presence of Fe_2O_3 or $NiFe_2O_4$ phases [88,129,130]. The absence of XPS signals for the SiO_2-supported catalysts suggests either limited surface accessibility or insufficient surface concentrations of Ni and Fe. These results collectively highlight

the influence of metal–support interactions and the surface distribution of active species on catalyst behavior.

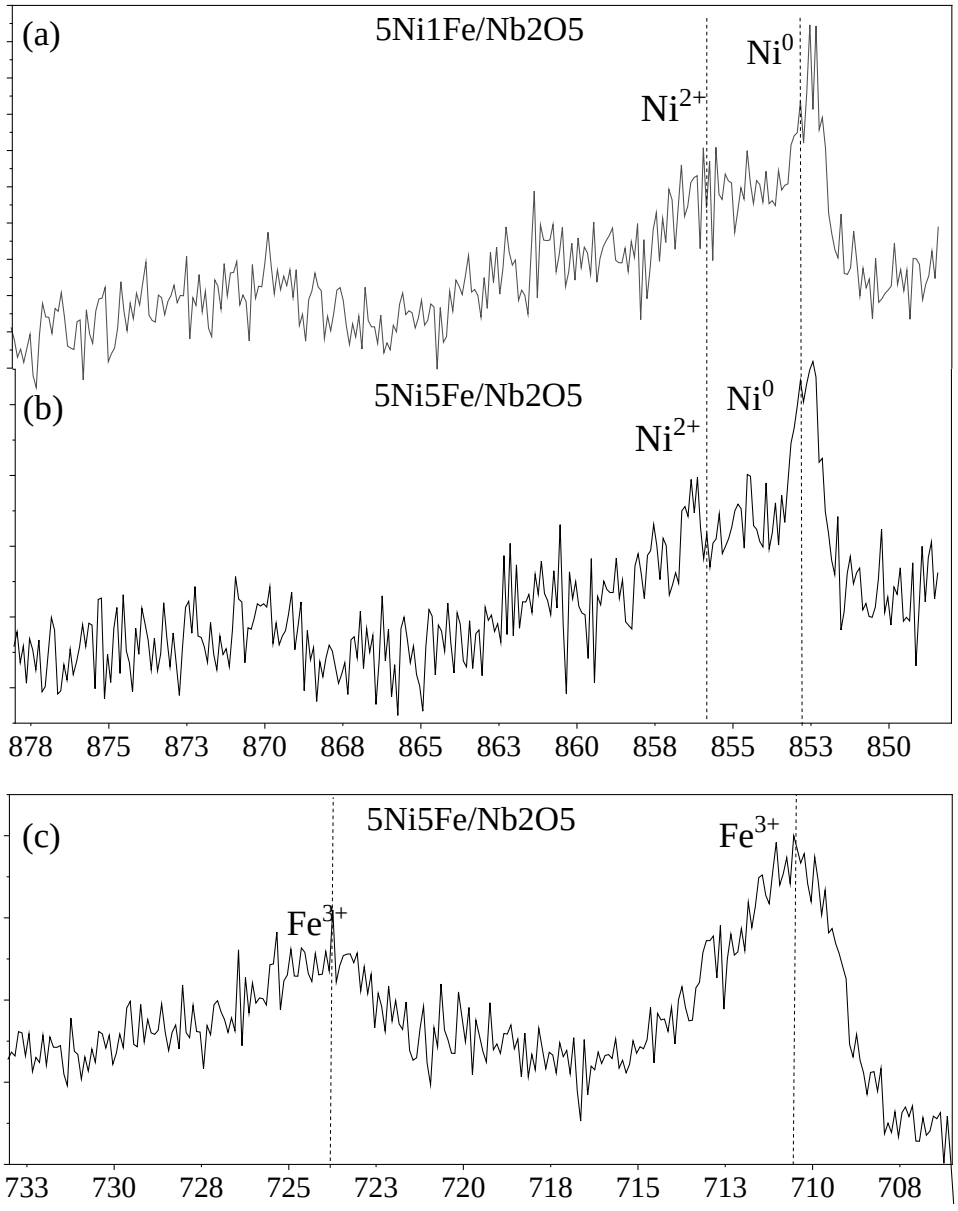

FIGURE 19 XPS spectra of Ni 2p and Fe 2p for the 5Ni1Fe/Nb_2O_5 and 5Ni5Fe/Nb_2O_5 catalysts.

4.2.2. CATALYTIC PERFORMANCE OF GUAIACOL IN HDO

The HDO of guaiacol at 300°C demonstrated that bimetallic Ni–Fe catalysts outperformed their monometallic counterparts, particularly in terms of their hydrogenation and deoxygenation activities, as shown in Table 9 and Figure 21. Among the tested catalysts, 5Ni1Fe/SiO_2 and 5Ni1Fe/Nb_2O_5 exhibited superior hydrogenation of phenolic compounds, with high selectivity toward cyclohexanol. The improved

performance of these catalysts is associated with their ability to promote deeper deoxygenation, as evidenced by the formation of cyclohexane — a fully deoxygenated product. Although the amount of cyclohexane was relatively low (around 10%), its presence was only observed in the Nb_2O_5-supported catalysts, highlighting the role of support acidity and metal-support interactions in favoring the direct deoxygenation (DDO) pathway. This improved performance can be attributed to the synergistic interaction between Ni and Fe, where Fe contributes to hydrogenolysis activity- crucial for breaking C–O bonds - and where Ni facilitates hydrogenation. However, increasing the Fe content in the bimetallic catalysts, as observed for 5Ni5Fe, resulted in lower guaiacol conversion and reduced selectivity toward cyclohexanol. This decline is likely due to the excessive Fe content disrupting the Ni–Fe synergy, thereby weakening the hydrogenation capacity of the catalyst, a phenomenon supported by the literature [20,27,133].

The influence of the support was also critical in determining the catalytic performance. As shown in Table 9 the 5Ni1Fe/Nb_2O_5 catalyst demonstrated the highest deoxygenation activity, significantly increasing the production of cyclohexane, a fully deoxygenated compound. This performance is attributed to the acidic and oxophilic properties of Nb_2O_5, which promote the direct deoxygenation (DDO) pathway by facilitating C–O bond cleavage and enhancing the reduction of Ni and Fe, as confirmed by NH_3-TPD analysis. Furthermore, the acidic sites of TT-Nb_2O_5 is responsible for the dehydration step of the reaction pathway, while the strong metal–support interaction ensures efficient hydrogenation. In contrast, SiO2-supported catalysts exhibited higher overall hydrogenation activity but preferentially promoted demethoxylation and hydrogenolysis pathways, resulting in intermediate products such as phenol, catechol, and cyclohexanone. Consequently, the SiO2-supported catalysts consumed more hydrogen compared to their Nb2O5-supported counterparts.

Monometallic Nb2O5-supported catalysts, such as 5Ni/Nb2O5 and 5Fe/Nb2O5, primarily favored partial deoxygenation routes, generating phenol, catechol, and methanol with relatively low hydrogen consumption (50% and 24%, respectively). On the other hand, the bimetallic catalyst 5Ni1Fe/Nb2O5 exhibited a clear preference for the direct deoxygenation pathway, leading predominantly to cyclohexanol and cyclohexane. The notably lower hydrogen consumption of 5Ni1Fe/Nb2O5 (28%)

compared to its SiO2-supported counterpart (82%) indicates that Nb2O5 promotes more efficient hydrogen utilization due to the balanced interaction of acid sites and metal active phases [134,135]

Additionally, the results align with findings of Yan et al. (2021) [21], which highlighted that bimetallic Ni-Fe catalysts achieve optimal guaiacol conversion and selectivity at higher Ni-Fe ratios owing to enhanced hydrogenation and hydrogenolysis activity. Fang et al. (2017) [87] also reported that a 5:1 Ni/Fe ratio achieves superior selectivity for cyclohexane, whereas higher Fe ratios lead to increased phenol selectivity. In this study, 5Ni1Fe/Nb_2O_5 exhibited similar trends, further emphasizing the importance of Ni–Fe synergy and the role of Nb_2O_5 in promoting deoxygenation pathways.

Synergistic effect of metal sites

The data in Table 5 and Table 9 reveal the crystallite sizes of the nickel and iron phases for the monometallic and bimetallic catalysts, alongside their dispersion values and catalytic performance. For the monometallic 5Ni/Nb_2O_5, the crystallite size of Ni reached 116 nm, which correlates with a relatively low dispersion (8.4%) and moderate guaiacol conversion (40%), with methanol (51%) and phenol (34%) as the primary products. This suggests that larger Ni particles limit the availability of active sites, reducing the overall efficiency of the catalyst. A similar trend was observed for 5Fe/Nb_2O_5, where the Fe crystallites reached 117 nm, leading to minimal H_2 consumption (24%) and a strong preference for partial deoxygenation products such as catechol (11%) and phenol (50%).

Compared with their Nb_2O_5 counterparts, the SiO_2-supported catalysts presented smaller Ni crystallite sizes and greater dispersion for monometallic catalysts. For example, 5Ni/SiO_2 exhibited a Ni crystallite size of 32 nm with a dispersion of 19.3%, resulting in 43% guaiacol conversion and significant production of cyclohexanone (13%). These findings align with those of studies by Li et al. (2017) [136], which demonstrated that the inclusion of SiO_2 enhances Ni dispersion, leading to increased hydrogenation activity but limited deoxygenation efficiency due to the lack of acidity.

In contrast, bimetallic 5Ni1Fe/Nb_2O_5 exhibited a smaller NiFe crystallite size of 21.8 nm, reflecting improved Ni dispersion (13.8%) and higher catalytic performance,

with 59% guaiacol conversion and a marked increase in cyclohexanol (34%) and cyclohexane (10%) selectivity. This enhancement can be attributed to the synergistic interaction between Ni and Fe, which facilitates hydrogenolysis and hydrogenation, as reported in previous studies [85,136]. The addition of Fe increases Ni dispersion by inhibiting agglomeration, thereby improving the accessibility of active sites, which in turn enhances hydrogen adsorption and C–O bond cleavage processes. Similar findings were reported for Fe-Ni/HZSM-5 systems, where Fe doping promoted NiO dispersion and enhanced catalytic activity [136]

However, the 5Ni1Fe/SiO_2 catalyst had a notable NiFe crystallite size of 68.1 nm and a dispersion of 6.1%, which was correlated with a lower guaiacol conversion (57%) than its Nb_2O_5-supported counterpart. The 5Ni5Fe/Nb_2O_5 and 5Ni5Fe/SiO_2 catalysts exhibited NiFe crystallite sizes of 37.8 nm and 66.2 nm, respectively. Guaiacol conversion and selectivity toward cyclohexane for 5Ni5Fe/SiO_2 were lower than those on 5Ni1Fe/Nb_2O_5, reinforcing that a higher Fe content disrupts the Ni–Fe synergy and leads to the dilution of active Ni sites. Excessive Fe addition altered the electronic and structural properties of Ni, thereby weakening hydrogenation and hydrogenolysis processes [26].

Finally, the formation of the NiFe alloy, as evidenced by the XRD patterns, further supports the improved catalytic activity of the bimetallic systems. The presence of alloy phases enhances metal–metal interactions, promoting efficient hydrogen activation and deoxygenation pathways. However, the catalytic performance is strongly dependent on the Ni:Fe ratio and support properties, as excessive Fe content, despite improving acidity (e.g., NH_3-TPD results), can lead to reduced metal dispersion and diminished catalytic efficiency.

TABLE 9 Guaiacol conversion (X Gua, %) and normalized product selectivity (%) for various catalysts during hydrodeoxygenation (HDO) at 300°C.

		X Gua (%)	Methanol	Phenol	Catechol	Cyclohexanone	Cyclohexane	Cyclohexanol	Fraction of H2 consumed (%)
Nb_2O_5	5Ni	40	51	34	6	0	0	0	50
	5Fe	40	50	25	11	1	0	0	24
	5Ni1Fe	59	48	3	0	5	10	34	28
	5Ni5Fe	46	50	4	1	5	10	12	49
SiO_2	5Ni	43	48	31	1	13	0	2	49
	5Fe	45	59	8	15	0	0	0	49
	5Ni1Fe	57	41	7	2	15	0	33	82
	5Ni5Fe	41	46	27	3	12	0	9	89

Influence of temperature on the catalytic performance of 5Ni1Fe/Nb_2O_5

The influence of temperature on product selectivity and guaiacol conversion was investigated using the 5Ni1Fe/Nb_2O_5 catalyst, as shown in Figure 20. These results, in agreement with observations reported in the literature, demonstrate that the reaction temperature plays a crucial role in determining the selectivity of the HDO reaction and the overall reaction pathway [137].

At 250°C, guaiacol conversion was moderate, and the main products were phenolic intermediates such as phenol and catechol. These findings indicate that at lower temperatures, partial deoxygenation and demethoxylation dominate the reaction mechanism, leading to incomplete HDO. This temperature regime is insufficient to overcome the activation energy required for complete deoxygenation, resulting in the accumulation of oxygenated intermediates.

Increasing the temperature to 300°C resulted in the highest guaiacol conversion and significant changes in the product distribution. At this temperature, selectivity toward cyclohexane and cyclohexanol were maximized, whereas phenol and catechol were almost entirely absent. This suggests that 300°C provides the optimal conditions for hydrogenation and deoxygenation pathways, promoting the production of fully deoxygenated products. These results align with those of Wan et al. (2014) [138], who reported enhanced hydrogenolysis and reduced hydrogenation with increasing temperature in HDO reactions using Pt/Al_2O_3. At 300°C, hydrogen availability and adsorption are sufficient to drive the conversion of intermediates into cyclohexane and cyclohexanol.

However, further increasing the reaction temperature to 350°C caused a decrease in guaiacol conversion and cyclohexane selectivity. This behavior can be attributed to the exothermic nature of hydrogen adsorption on the catalyst surface [29]. At elevated temperatures, the reduced hydrogen coverage likely limits the efficiency of hydrogenation and deoxygenation, resulting in a shift toward hydrogenolysis pathways. This shift is evidenced by the lower selectivity for cycloalkanes and the persistence of phenolic intermediates. Additionally, the selectivity for cyclohexanol decreased significantly, reflecting the unfavorable thermodynamics of hydrogenation at higher temperatures.

The temperature dependence of product selectivity highlights the intricate balance between reaction pathways. At lower temperatures, the reaction favors partial deoxygenation, whereas at intermediate temperatures (300°C), hydrogenation and deoxygenation dominate. At higher temperatures, the reaction shifts toward hydrogenolysis and possibly the formation of coke precursors. Previous studies [137,139] have reported that higher temperatures promote the polymerization of oxygen-containing compounds, leading to increased coke formation on the catalyst surface.

These results underscore the importance of temperature optimization in HDO processes. While 300°C is the optimal temperature for maximizing the production of fully deoxygenated products such as cyclohexane, higher temperatures can reduce efficiency by limiting hydrogen adsorption and promoting undesired pathways.

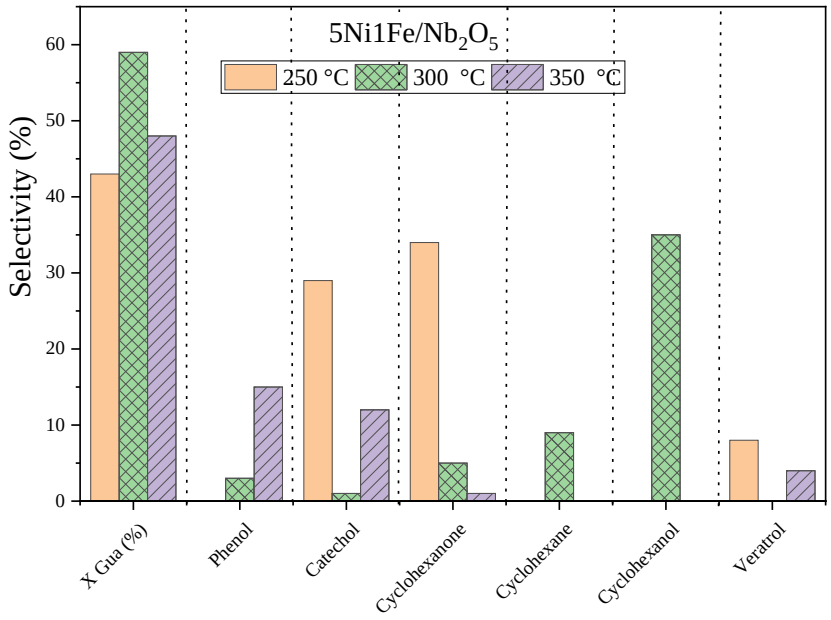

FIGURE 20 Effects of reaction temperature (250°C, 300°C, and 350°C) on guaiacol conversion (X_{Gua}, %) and product selectivity during hydrodeoxygenation (HDO) when the 5Ni1Fe/Nb_2O_5 catalyst is used

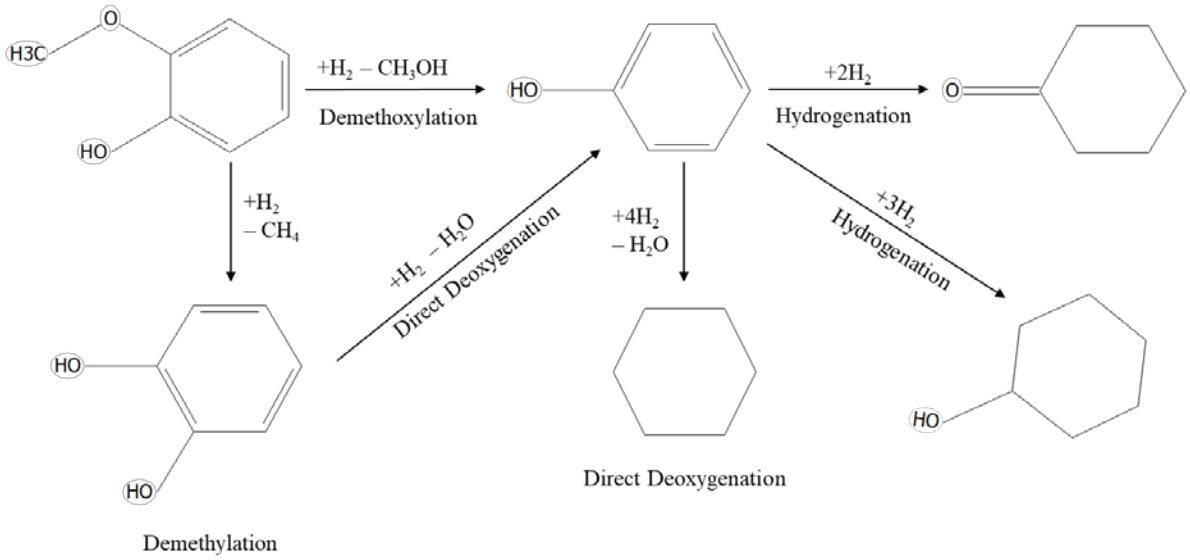

FIGURE 21. Proposed reaction pathway for the hydrodeoxygenation (HDO) of guaiacol

Conclusion

This study explored the hydrodeoxygenation (HDO) of guaiacol using Ni–Fe bimetallic catalysts supported on Nb_2O_5 and SiO_2, focusing on the synergistic interaction between Ni and Fe and the influence of Nb_2O_5 as a support. The catalysts were characterized to correlate their physical and chemical properties with their catalytic activity. Initial screening at 300°C was performed to identify the most suitable catalyst based on activity and selectivity. The selected catalyst, 5Ni1Fe/Nb_2O_5, was then used to investigate the impact of the reaction temperature on the product selectivity and reaction pathways.

The results from the catalyst screening revealed that the Nb_2O_5-supported catalysts exhibited higher deoxygenation activity than their SiO_2-supported counterparts did. This superior performance was attributed to the acidic properties of TT-Nb_2O_5, which promote C–O bond cleavage, and its ability to increase the reduction of Ni and Fe. These factors, combined with the strong synergistic interaction between Ni and Fe, facilitated direct deoxygenation (DDO) pathways, resulting in a significant reduction in oxygenated compounds. Notably, guaiacol conversion to cyclohexane, a fully deoxygenated product, was observed only for the Nb_2O_5-supported Ni–Fe catalysts.

Among the bimetallic catalysts, Fe loading had a critical effect on performance. While the 5Ni1Fe/Nb_2O_5 catalyst demonstrated superior activity and selectivity toward cyclohexanol and cyclohexane, the higher Fe content in 5Ni5Fe/Nb_2O_5 disrupted the Ni–Fe synergy, leading to lower guaiacol conversion and cyclohexanol selectivity.

The temperature-dependent behavior of the selected 5Ni1Fe/Nb_2O_5 catalyst further highlighted its versatility. At moderate temperatures, products from hydrogenation pathways, such as cyclohexanol and cyclohexane, were favored, reflecting the optimal balance between hydrogenation and deoxygenation. At higher temperatures, the selectivity shifted toward phenol, reflecting the reduced thermodynamic favorability of hydrogenation and a shift toward hydrogenolysis pathways.

In conclusion, this study demonstrates that combining the proven Ni–Fe synergy with the properties of Nb_2O_5 as a support offers a promising approach for efficient HDO processes. The 5Ni1Fe/Nb_2O_5 catalyst outperformed the other tested catalysts, achieving high guaiacol conversion and selectivity toward fully deoxygenated products. These findings highlight the potential of Nb_2O_5-supported bimetallic catalysts for sustainable bio-oil upgrading and provide valuable insights into the design of advanced HDO catalysts for renewable energy applications.

CHAPTER 5

INVESTIGATION OF Nb_2O_5 CATALYSTS IN HDO OF FAST PYROLYSIS BIO-OIL

5.1. MOTIVATION

The scope of the investigation has been expanded to understand the catalysts for the mild hydrodeoxygenation of fast pyrolysis bio-oil. This progression is aimed at advancing the practical application of these catalysts in bio-oil upgrading. In addition, this study extends the comparison of the catalytic properties of Ni-Fe alloy with those of a noble metal (ruthenium), providing a broader perspective on catalyst performance.

Ruthenium catalysts, known for their high hydrogenation activity [140], serve as benchmarks due to their synergistic combination with acidic supports like Nb_2O_5, which activate C=O and C=C bonds efficiently. Therefore, they have been selected for comparison with Ni-Fe/Nb_2O_5 catalysts in studying liquid-phase HDO. The bimetallic 5Ni1Fe and 5Ni5Fe supported in Nb_2O_5 were synthetized using the same method described in chapter 3.

The experimental work was conducted at the Karlsruhe Institute of Technology (KIT), specifically at the Institute for Catalysis Research and Technology (IKFT). The catalysts were tested under the same mild conditions previously reported by Boscagli et al. (2015) [109], at 250 °C in a 200 mL batch reactor with 80 bar of H_2. The light fraction of bio-oil was employed, focusing on the reactivity towards polar and lower molecular weight compounds, such as sugar derivatives, lignin-derived monomers, acids, and ketones.

5.2 EXPERIMENTAL METHODS (Summary)

For the hydrodeoxygenation of fast pyrolysis bio-oil (FPBO), the 5Ni1Fe/Nb_2O_5, 5Ni5Fe/Nb_2O_5, and 5Ru/Nb_2O_5 catalysts were prepared using the wet impregnation method, followed by calcination at 500°C. Catalyst characterization included ICP-OES for bulk metal composition, XRD for phase composition, NH_3-TPD for acidity analysis, and BET analysis to determine surface area and porosity. The

morphology and elemental distribution were examined through scanning electron microscopy (SEM) and energy-dispersive spectroscopy (EDS).

The HDO experiments were conducted in a 200 mL batch reactor, using the light fraction of FPBO from beech wood as feedstock. The reaction was performed at 250°C, under an 8 MPa hydrogen pressure, for 2 hours, with 2.5 g of catalyst. The upgraded oil and aqueous phases were analyzed to assess deoxygenation efficiency and fuel quality improvements. Elemental analysis (C, H, N, O) determined the chemical composition, while the water content was measured using Karl Fischer titration. The higher heating value (HHV) of the upgraded oil was calculated to evaluate its energy content. A Van Krevelen plot was used to visualize the carbon efficiency and oxygen removal.

The product composition was analyzed using GC-MS and GC-FID for compound identification and quantification, while ^{1}H-NMR spectroscopy provided insights into the functional group transformations. Additionally, the consumption of H_2 and CO_2 production was monitored to evaluate the efficiency of deoxygenation and hydrogen utilization.

5.3. RESULTS AND DISCUSSION

5.3.1. CATALYST CHARACTERIZATION

Elemental composition of the 5Ru/Nb_2O_5 catalyst was determined via two analytical approaches: Inductively Coupled Plasma (ICP) and Energy-Dispersive X-ray Spectroscopy (EDS). ICP analysis revealed a ruthenium content lower than expected, at 3.17 wt.%, indicating potential challenges in the impregnation process. On the other hand, EDS offered insights into the distribution of metals on the surface, revealing discrepancies between surface metal content and the overall bulk composition. The EDS analysis was conducted to validate and complement the ICP findings. The Table 10 show the results.

TABLE 10. Results of the elementary composition

Catalyst	Elementary Composition by ICP		Elementary Composition by EDS		
	Ru (wt. %)	Nb (wt. %)	Ru (wt. %)	Nb (wt. %)	O (wt. %)
5Ru	3.17	60.2	8.14	65.36	21.62

The calcination of Nb_2O_5 support is a critical step in achieving the optimal niobia structure for catalytic applications. SEM images Figure 22 illustrate the transformations undergone by the support post-calcination at 500 °C. Initially, as niobic acid ($Nb_2O_5.nH_2O$), the material presents a clustered, less defined structure with larger, irregular particles. Following calcination, there is a marked structural transformation; particles become smaller and more defined, signifying dehydration and formation of the TT pseudo-hexagonal crystalline structure of Nb_2O_5. This process results in a more uniform morphology with apparent increased porosity, desirable characteristics for a catalytic support, as they increase the available surface area for the dispersion of catalytic metals and the accessibility of active sites, as highlighted by Campos Fraga et al. (2023) [99].

FIGURE 22. SEM images of HY-340 or $Nb_2O_5 \cdot nH_2O$ on the left and on the right Nb_2O_5 calcined at 500 °C known as TT-Nb_2O_5.

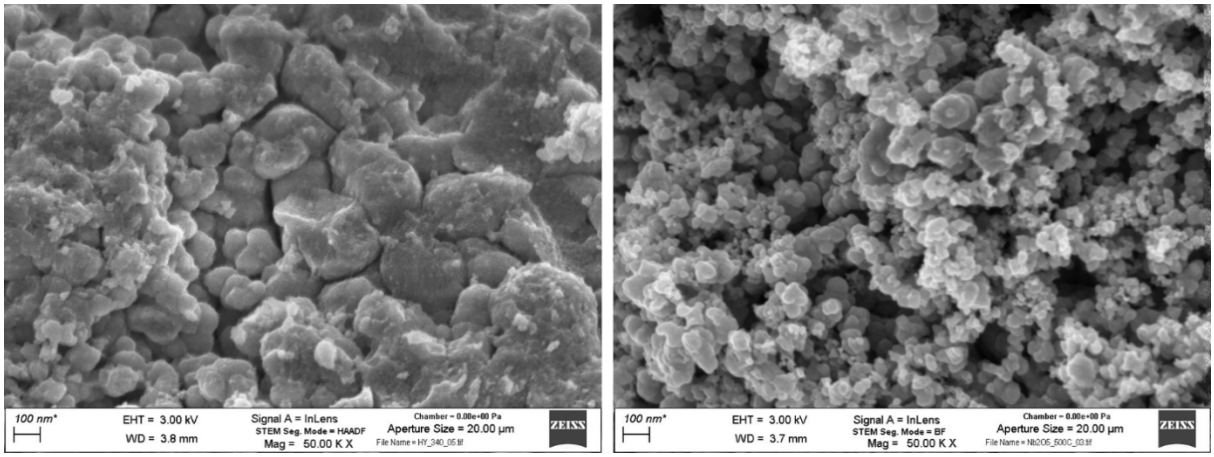

SEM images of the catalysts with corresponded EDS mapping, are showed in Figure 23, Figure 24,Figure 25. This analyze provide the distribution of metals on the catalysts, despite the challenging contrast differentiation between Ni, Fe and Ru particles, and the Nb_2O_5 support crystallites. The left image displays the morphology of the catalysts, while the right images highlight the elemental distribution on its surface. The EDS mapping reveals an even spread of nickel (blue), iron (green), and niobium (purple).

The catalyst 5Ni1Fe/Nb_2O_5 Figure 23 exhibit a relatively uniform distribution, with some larger irregular structures, which could correspond to metal oxide clusters or

areas of localized metal accumulation. The EDS analysis may suggest that Fe is less uniformly distributed compared to Ni, indicating possible phase segregation or clustering. In Figure 24, the 5Ni5Fe/Nb_2O_5 catalyst shows similar in morphology and characterized by clusters, but with a higher presence of Fe through EDS analysis, signifying a more substantial Fe integration, as evidenced by larger cluster formations.

FIGURE 23. SEM image of 5Ni1Fe/Nb_2O_5 catalyst with corresponding chemical mapping and EDS

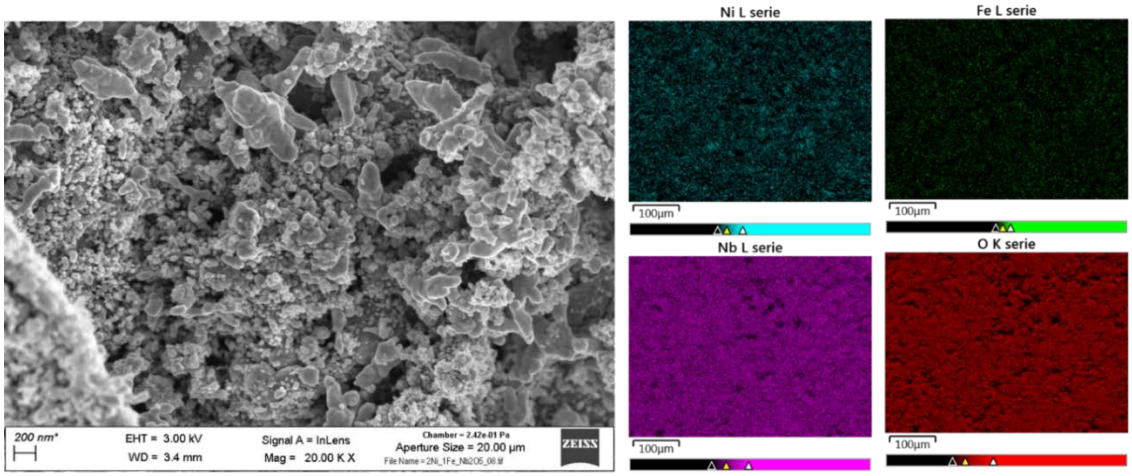

FIGURE 24. SEM image of 5Ni5Fe/Nb_2O_5 catalyst with corresponding chemical mapping and EDS

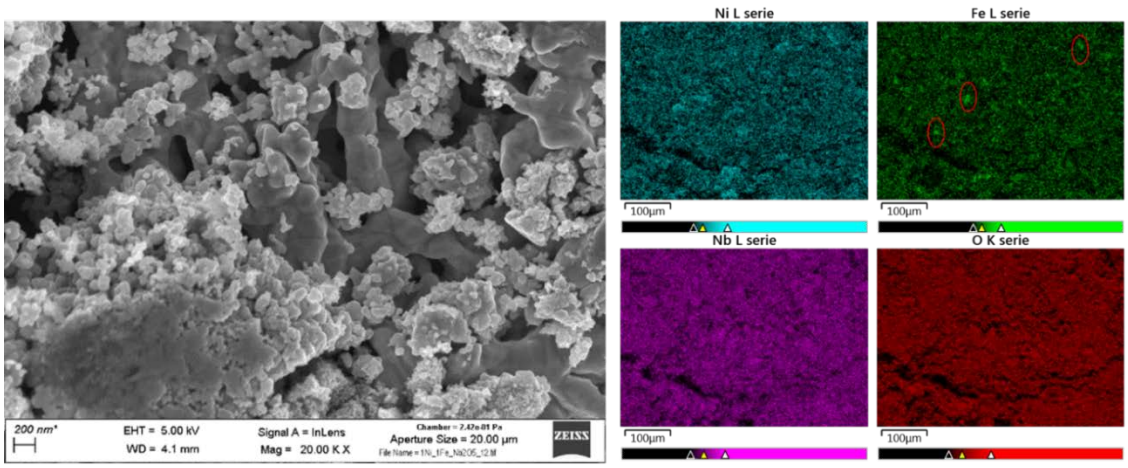

The 5Ru/Nb_2O_5 catalyst exhibits a heterogeneous morphology (Figure 25) similar to the other catalysts, characterized by varying particle sizes. However, it uniquely displays a distinct structure with the formation of sharper, cone-like features with less evidence of cluster formation compared to the previous catalysts. The EDS mapping signals for ruthenium (blue), niobium (green), and oxygen (red) demonstrate a homogeneous dispersion of ruthenium across the niobium oxide support.

FIGURE 25. SEM image of 5Ru/Nb_2O_5 catalyst with corresponding chemical mapping and EDS

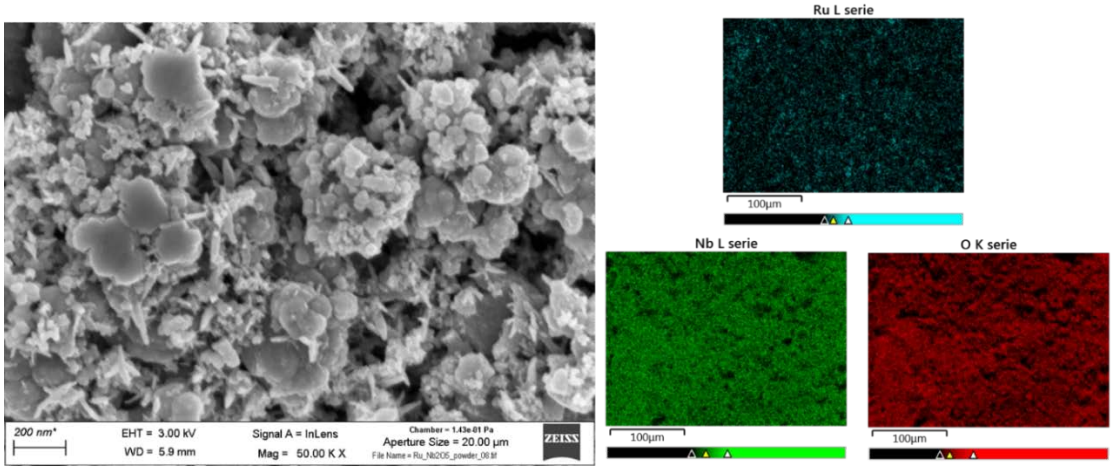

The catalyst 5Ru/Nb_2O_5 underwent NH_3-TPD and BET analysis Table 11 to evaluate the acid site distribution and compare it with the Ni-Fe bimetallic catalysts. Interestingly, the Ru catalyst exhibited a lesser reduction in surface area compared to the Ni-Fe catalysts, likely due to the significantly lower content of impregnated metal. Additionally, the method used for reduction may have impacted the textural properties of these materials.

NH_3-TPD analysis revealed two prominent peaks for the 5Ru/Nb_2O_5 catalyst, indicative of the presence of acid sites of varying strengths. The first peak, observed at 185 °C, is associated with weak acid sites, while the second peak at 345 °C corresponds to medium-strength acid sites [141]. To accurately quantify the types of acid sites, present, the TPD profiles were analyzed using a multiple-Gaussian function. This method allows for the deconvolution of the TPD curves, enabling the integration of individual desorption curves corresponding to weak, medium, and strong acid sites.

TABLE 11. Total acidity (μmol NH_3/g catalyst) measured by NH_3-TPD, the BET surface area (SBET, m^2/g), the acid site density (μmol/m^2), and the relative distribution of weak, medium, and strong acid sites (%).

Sample	Acidity ($\mu molNH_3/g_{cat}$)	S_{BET} (m^2/g)	Density of the acid sites (μmol/m^2)	Acid sites distribution (%)		
				Weak	Medium	Strong
$5Ru/Nb_2O_5$	707.6	35.8	19.7	31	69	0.0
$5Ni1Fe/Nb_2O_5$	274.3	30.2	9.1	0	25	75
$5Ni5Fe/Nb_2O_5$	295.2	21.7	13.6	0	8	70
Nb_2O_5	668.0	57.3	11.65	0	25	75

FIGURE 26. Ammonia desorption profiles (NH_3-TPD) of the samples

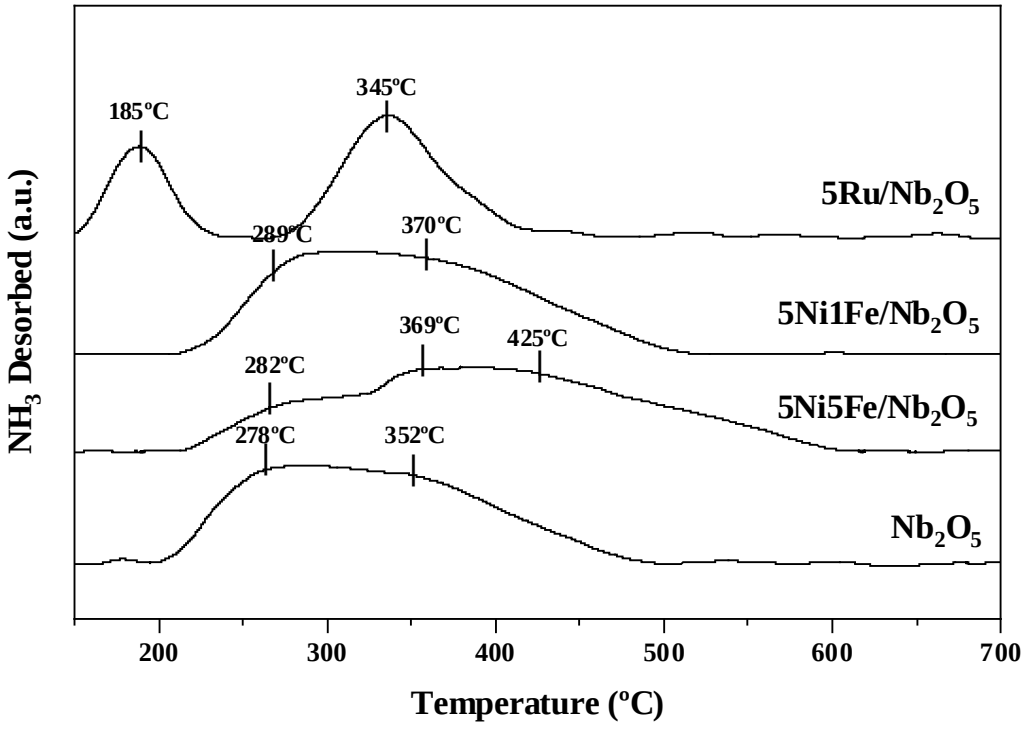

The Ru/Nb_2O_5 catalyst demonstrates significantly higher acidity by mass (707.6 μmol/g_{cat}) as a higher density of the acid sites. It is noteworthy that 31% of the acid sites are categorized as weak, indicating a predominance of weaker acid strength, with no strong acid sites detected, and the remaining 69% being of medium strength. This characteristic may be attributed to the presence of unreduced species within the

catalyst, as evidenced by the detection of RuO_2 in the XRD analysis Figure 27. The catalyst exhibits a low degree of reduction and the presence of RuO_2 on the catalyst surface is likely to affect its acidic properties, impacting its catalytic behavior.

FIGURE 27. X-ray diffraction (XRD) patterns of the passivated 5Ru/Nb_2O_5 catalyst and the Nb_2O_5 support.

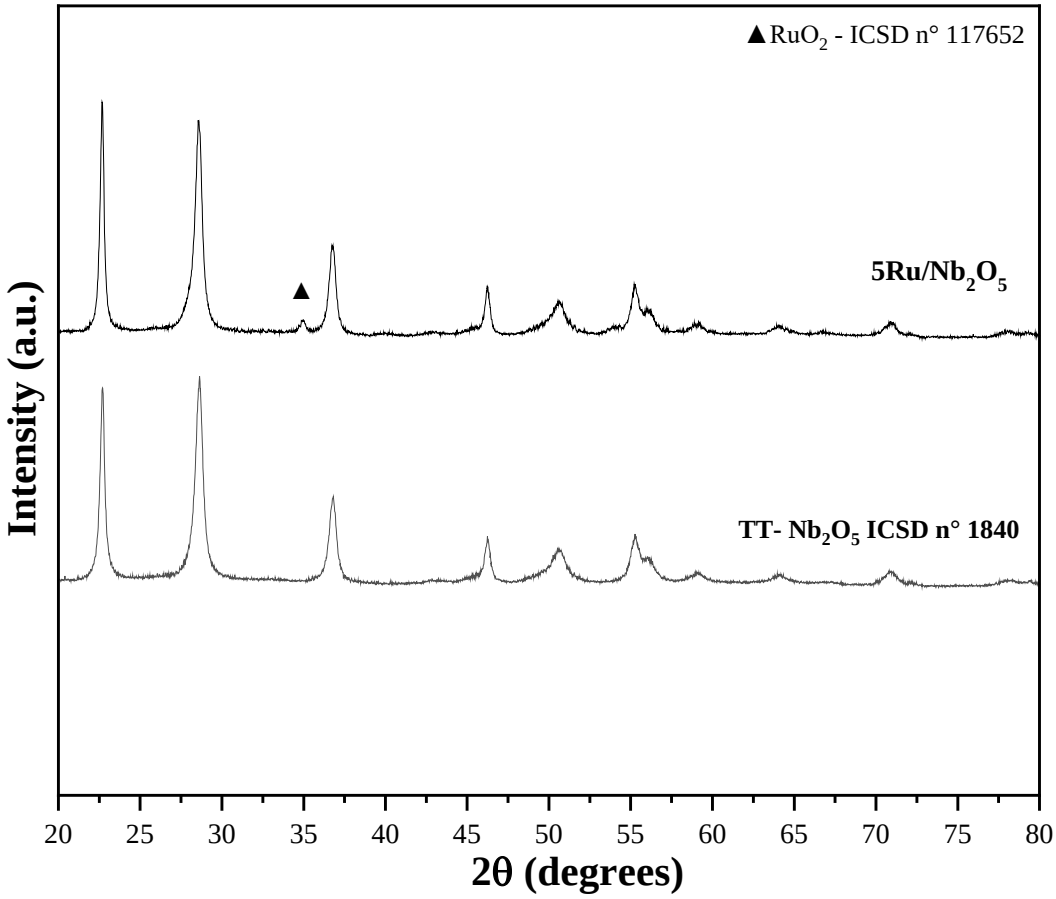

The X-ray diffraction (XRD) patterns for the reduced and passivated catalysts confirm the presence of the TT-Nb_2O_5 phase, characterized by its hexagonal lattice, as previously discussed in Chapter 4. This phase is identified by its characteristic diffraction peaks at 2θ = 22.7° and 28.6°, consistent with the Cambridge Crystallographic Data Centre (CCDC) reference code n° 2103847 or Inorganic Crystal Structure Database (ICSD) n° 1840.

For the 5Ru/Nb_2O_5 catalyst, an additional diffraction peak at 2θ = 35.1° corresponds to RuO_2, referenced in the ICSD under n° 117652. It is noteworthy that the RuO_2 peak at 2θ = 27.9° overlaps with that of TT-Nb_2O_5, which may contribute to peak broadening or intensity variations. The absence of distinct metallic ruthenium (Ru^0)

peaks suggests a high dispersion of Ru species or their possible interaction with the Nb_2O_5 support, reinforcing the hypothesis of strong metal-support interactions.

5.3.3. HYDRODEOXYGENATION (HDO) OF FPBO

The hydrodeoxygenation (HDO) reactions were performed using the light phase of beech wood fast pyrolysis oil (BTG Biomass Technology Group BV, Enschede, The Netherlands) as the feedstock. The primary objective of the HDO reaction was to reduce the oxygen content in the bio-oil while retaining its carbon and hydrogen composition as much as possible. The initial feedstock contained 32.9 wt.% carbon, 8.1 wt.% hydrogen, 0.1 wt.% nitrogen, and a high oxygen content of 58.9 wt.%, making deoxygenation a key requirement.

The catalytic tests were carried out in a 200 mL batch reactor using 2.5 g of catalyst per 50 g of bio-oil. The reactions were conducted at 250 °C for 2 hours, with a controlled heating ramp of 3.33°C min^{-1}, under an initial H_2 pressure of 8 MPa.

After the upgrading reactions, the products were classified into two major liquid phases: upgraded oil phase (UOP) and aqueous phase (AP), along with minor fractions of gaseous and solid products. The aqueous phase exhibited an orange to light brown color, darkening over time due to aging, but maintaining a water-like consistency across all reactions. In contrast, the upgraded oil phase was deep brown, denser than the aqueous phase, and exhibited a significantly higher viscosity. The viscosity varied depending on the catalyst used, indicating different extents of deoxygenation and structural modifications.

Table 12 revealed that the upgraded oils had significantly higher carbon contents, ranging from 62.8 to 65.9 wt.% (dry basis) for all catalysts tested. The highest carbon content was observed for 5Ni5Fe/Nb_2O_5 (65.9 wt.%), representing an increase of 24.5% compared to the feedstock. Similarly, the hydrogen content increased in the upgraded oils, contributing to an improvement in the fuel properties. As expected, a significant reduction in oxygen content was observed across all catalysts, with 5Ru/Nb_2O_5 reducing the oxygen from 40.7 wt.% (dry basis) in the feedstock to 26.5 wt.%, followed by 5Ni5Fe/Nb_2O_5 (27.2 wt.%) and 5Ni1Fe/Nb_2O_5 (30.7 wt.%).

The water content in the upgraded oil was reduced compared to the feedstock, which initially contained 37.8 wt.% water. After upgrading, the water content ranged from 6.0 to 7.4 wt.%, with 5Ru/Nb_2O_5 producing a slightly higher water concentration (7.4 wt.%) than the bimetallic catalysts. This reduction in water content indicates effective deoxygenation and a shift in polarity of the bio-oil components.

The removal of oxygen and water significantly increased the higher heating value (HHV) of the upgraded oils. Compared to the initial 20.1 MJ/kg of the feedstock, the HHV increased by 52.2% for 5Ru/Nb_2O_5 (30.6 MJ/kg), 44.3% for 5Ni5Fe/Nb_2O_5 (29.0 MJ/kg), and 36.8% for 5Ni1Fe/Nb_2O_5 (27.5 MJ/kg). This improvement highlights the efficiency of the catalysts in enhancing the energy density of the bio-oil, making it more suitable for potential fuel applications.

TABLE 12. Chemical composition of upgraded oils at different reaction conditions (8 MPa, 2h of reaction).

Feedstock	C (wt. %)		H (wt. %)		N (wt. %)		O (wt. %)		H2O (wt. %)	HHV calc (MJ/kg)
	wb.	db.	wb.	db.	wb.	db.	wb.	db.	wb.	wb.
	32.9	52.9	8.1	6.3	0.1	0.3	58.9	40.7	37.8	20.1
Upgraded Oil										
5Ni1Fe/Nb_2O_5	58.2	62.8	6.6	6.2	0.2	0.2	35	30.7	6.1	27.5
5Ni5Fe/Nb_2O_5	61	65.9	7	6.7	0.2	0.2	31.8	27.2	6	29
5Ru/Nb_2O_5	59.6	64.3	6.4	6	0.1	0.1	33.9	26.5	7.4	30.6
Aqueous Phase										
5Ni1Fe/Nb_2O_5	13.9	46.6	9.9	7	1	3.3	75.2	43	70.2	20
5Ni5Fe/Nb_2O_5	12.9	41.9	9.8	6.8	1.3	4.2	76	47	69.2	17.9
5Ru/Nb_2O_5	14	45.4	10.2	8.1	1.4	4.5	74.4	41.8	69	21

According to Mortensen et al. (2013) [61], Ni catalysts demonstrate excellent performance when supported on oxides, exhibiting high yield for oxygen removal through hydrogenation and cracking reactions under mild conditions, typically ranging from 150 to 250 °C. On the other hand, Fe catalysts have proven to be effective for bio-oil upgrading through hydrodeoxygenation and ketonization reactions [142] [77].

The $5Ru/Nb_2O_5$ catalyst demonstrated deoxygenation efficiency and an increase in the heating value of the upgraded bio-oil, performing comparably to the bimetallic Ni-Fe catalysts. Ruthenium-based catalysts are well known for their superior hydrogenation capabilities, as reported in the literature [106,143]. The similar deoxygenation efficiency and HHV enhancement observed for $5Ru/Nb_2O_5$ and Ni-Fe catalysts suggest that their catalytic mechanisms involve both hydrogenation and C–O bond cleavage. This observation underscores the significance of the support's acidity in influencing yield for oxygen removal during mild hydrodeoxygenation (HDO) conditions [144–147].

For Ni-Fe catalysts, the dominant reaction pathways in bio-oil upgrading have been identified as hydrogenation and hydrogenolysis, leading to efficient oxygen removal. Both Ru-based and Ni-Fe catalysts removed oxygen primarily in the form of water, with $5Ni1Fe/Nb_2O_5$ exhibiting superior hydrogenation activity, likely due to the specific reaction conditions applied. The oxophilic sites of Fe potentially act as C–O bond scission sites, facilitating deoxygenation—a hypothesis supported by the substantial water formation observed [102]. To further enhance oxygen removal, a secondary upgrading step under more severe conditions, such as elevated temperatures, could be implemented to achieve deeper deoxygenation and improved bio-oil quality.

A Van Krevelen diagram Figure 28 was used in order to visualize the transformations occurring during the hydrotreatment reactions in terms of C, H and O content [106] standard quality characteristic for the upgraded oil is achieving a low molar O/C ratio, ideally approaching zero, indicating efficient removal of oxygen. Simultaneously, a moderate H/C ratio around 1.50 is targeted, considering that the H/C ratio in crude oil typically falls within the range of 1.50 to 2.00. The reduction of the O/C ratio indicates hydrodeoxygenation, whereas an increase in the H/C ratio may indicate hydrogenation of the upgraded oils [148]. The upgrading reactions reduced the O/C ratio of the feedstock from 0.59 to the range of 0.31-0.36. Notably, the $5Ni:5Fe/Nb_2O_5$ catalyst achieved the lowest O/C ratio of 0.31, indicating superior deoxygenation efficiency. In

terms of hydrogenation, although all catalysts facilitated this process, the 5Ru/Nb_2O_5 catalyst stood out, demonstrating enhanced hydrogenation capabilities, as reflected by the reduction in the H/C ratio.

FIGURE 28. Van Krevelen plot of the upgraded oil obtained with the catalysts.

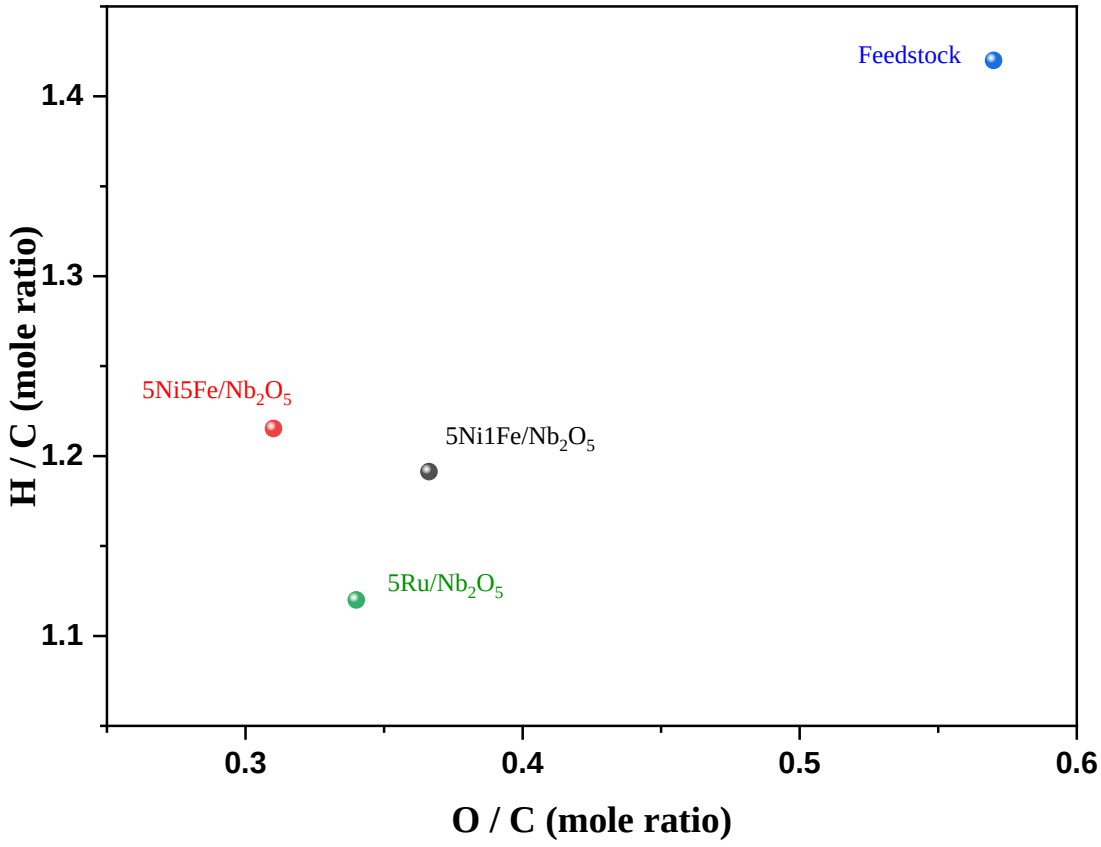

5.3.4. HYDRODEOXYGENATION (HDO) MECHANISMS

The upgraded samples were further analyzed using GC-MS for compound identification, with the main chemical species identified through the National Institute of Standards and Technology (NIST) mass spectral library. The relative content of each compound was determined by calculating its peak area ratio to the total peak area in the GC-MS spectra. Additionally, GC-FID was employed for quantification, ensuring accurate determination of compound concentrations. The combination of GC-MS for qualitative analysis and GC-FID for precise quantification provided a comprehensive evaluation of both the feedstock and its upgraded products. The high sensitivity of GC-FID enabled accurate quantification of seven key compounds, including lignin-derived

phenolics such as phenol, catechol, and guaiacols, which are crucial indicators of deoxygenation efficiency in hydrodeoxygenation (HDO) reactions.

The feedstock's carbohydrate content was primarily composed of sugars (56.1% of detectable compounds), with a lower concentration of lignin-derived compounds and methoxyphenols, which are characteristic of woody biomass [148]. among the detected sugars, levoglucosan was predominant but was completely converted during the catalytic treatments into products such as CO_2, various alcohols (ethylene glycol, propylene glycol, 1,2-butanediol), and acetic acid. Notably, the treated samples exhibited a substantial increase in alcohol compounds, which were absent in the raw feedstock but appeared in four distinct types after upgrading, primarily ethylene glycol and methanol. This transformation aligns with findings from a two-stage HDO process applied to pine sawdust-derived bio-oil, where researchers demonstrated that oxygenated compounds were partially converted into alcohols in the first HDO step (300°C, 10 MPa H_2, Ru/C catalyst), effectively reducing their reactivity. In a subsequent higher-temperature stage (400°C, 13 MPa H_2, $NiMo/Al_2O_3$ catalyst), the remaining oxygenates underwent deep deoxygenation, producing a hydrocarbon-rich bio-oil with enhanced stability [149].

Following the upgrading process, sugars and nitrogenous compounds were entirely removed across all tested catalysts. However, a notable presence of guaiacol compounds and methoxy phenols was observed, which are lignin-derived molecules containing phenol and methoxyl functional groups. This suggests that partial deoxygenation and hydrogenation occurred during the HDO reaction. The formation of alcohols, benzenes, and esters indicates that these species could be intermediates, implying that further conversion might be possible under more severe reaction conditions or by employing a more active catalyst.

The persistent presence of guaiacols and methoxyphenols in the upgraded oil aligns with literature reports suggesting that a single-stage HDO may not achieve complete deoxygenation, particularly when operating under mild conditions. It has been established that two-stage HDO is a more effective strategy to overcome the complexity of pyrolytic oil upgrading, particularly for mitigating coke formation [150]. At lower temperatures, cellulose- and hemicellulose-derived oxygenates are more reactive and prone to polymerization, leading to coke formation. In contrast, at higher temperatures, pyrolytic lignin compounds become the primary cause of coke formation [[151].

Consequently, in a two-step HDO approach, the first stage focuses on stabilizing the reactive oxygenates, converting them into less reactive intermediates at lower temperatures. Even if full deoxygenation is not achieved in this step, the oil becomes more stable, reducing the likelihood of further polymerization and coke formation in the subsequent upgrading stage.

The GC-FID quantification confirmed that hydrotreatment significantly reduced lignin-derived phenols in the upgraded oils, demonstrating the efficiency of the catalysts. For example, guaiacol content decreased from 7.3 g/kgPO in the feedstock to 2.1 g/kgPO with 5Ni1Fe/Nb_2O_5 and to 1.7 g/kgPO with 5Ru/Nb_2O_5, while phenol content was reduced from 1.8 g/kgPO to 0.5 g/kgPO with 5Ni1Fe/Nb_2O_5. These results indicate that 5Ni1Fe/Nb_2O_5 exhibited a strong capacity for deoxygenation. The bimetallic catalyst appears to enhance both hydrogenation and hydrogenolysis, facilitating C–C and C–O bond cleavage in the presence of hydrogen.

Additionally, the observed reduction in phenolic compounds may be attributed to dehydration reactions, where water is eliminated from organic molecules, often resulting in the formation of aromatic hydrocarbons [106]. These findings further support the hypothesis that oxophilic Fe sites in Ni-Fe catalysts act as C–O bond scission sites, promoting efficient oxygen removal via water formation [102].

Figure 29. Distribution of the volatile products based on relative concentration from GC/MS

Feedstock

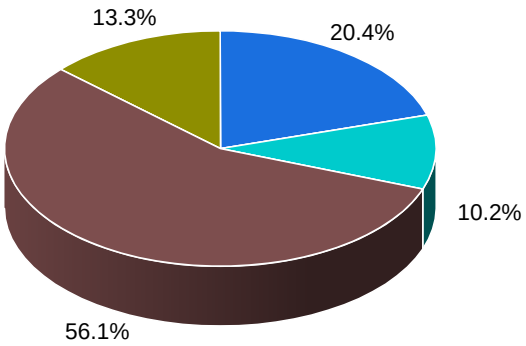

5Ni5Fe/Nb_2O_5

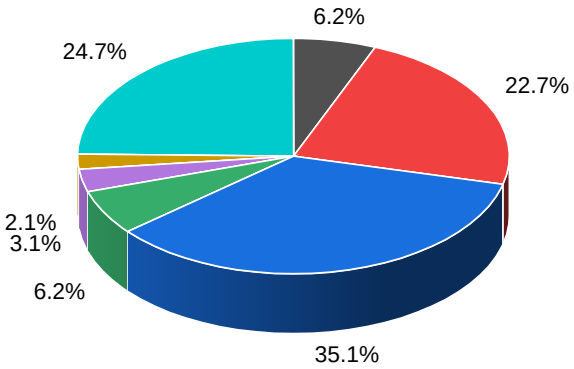

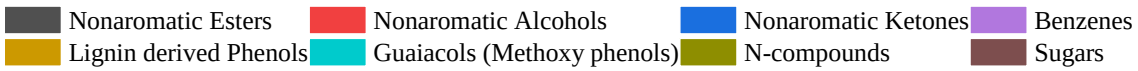

5Ni1Fe/Nb_2O_5

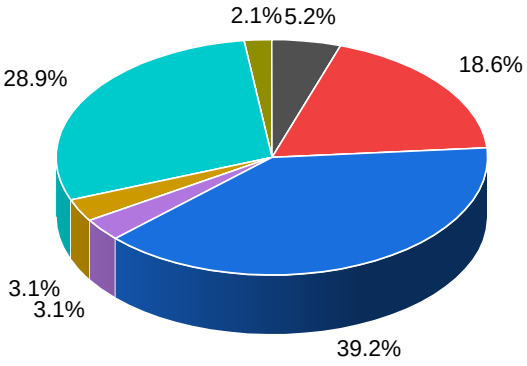

5Ru/Nb_2O_5

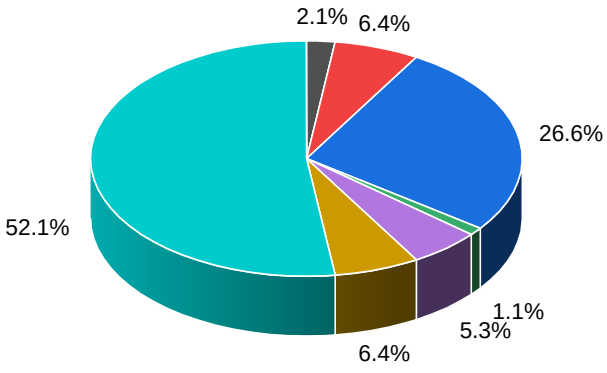

FIGURE 30. Composition of the upgraded oil determined by GC-FID for representative compounds.

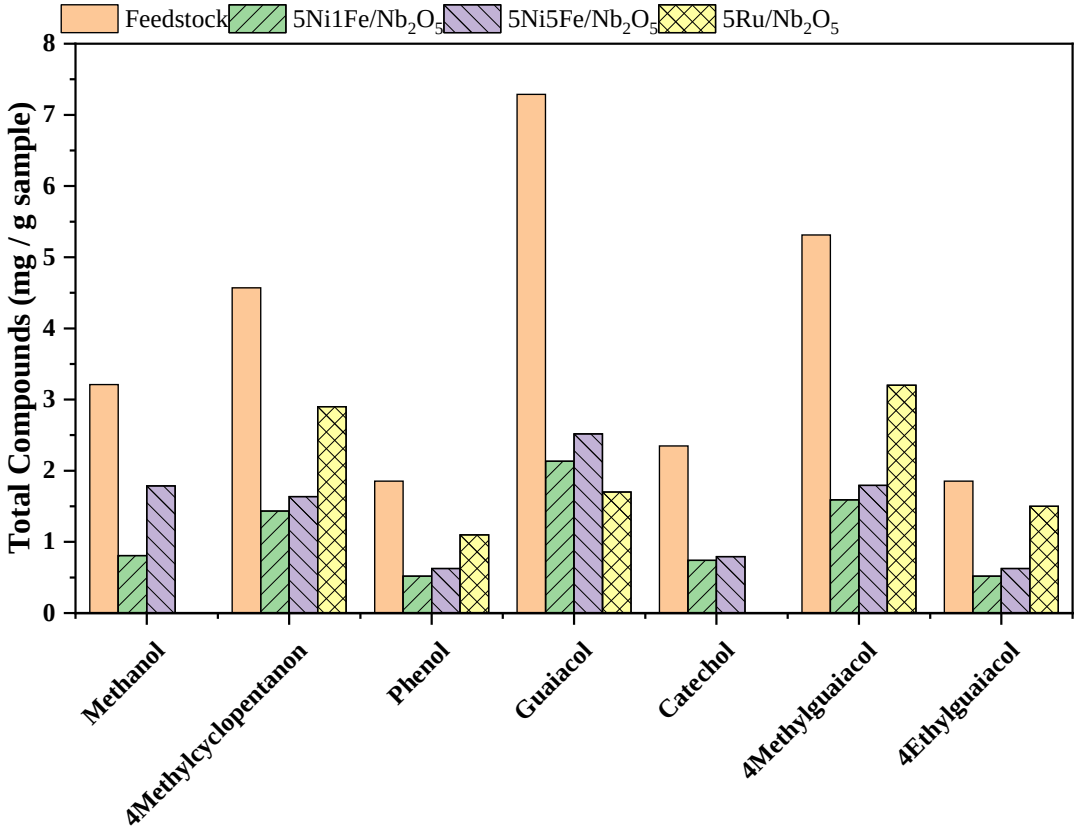

In evaluating the hydrodeoxygenation (HDO) performance of Nb_2O_5 supported catalysts, three critical factors must be considered: hydrogen consumption, degree of deoxygenation (DOD), and CO_2 production. Hydrogenolysis and hydrogenation typically result in increased hydrogen consumption because hydrogen atoms are being added to the organic molecules. In the case of decarboxylation, carbon is lost in the form of CO_2, which is not desirable for HDO efficiency as it indicates the loss of carbon content from the feedstock. The degree of deoxygenation (DOD) is an essential parameter indicating the effectiveness of oxygen removal from the feedstock, which is a key goal in HDO to improve the quality of the bio-oil by reducing its oxygen content.

The internal pressure and temperature of the autoclave were recorded along the reaction. A rough trend was plotted using the ideal gas and Soave Redlich Kwong equations to estimate the theoretical H_2 pressure in the autoclave without gas consumption.

TABLE 13. Comparison of the key results, namely hydrogen consumption, DOD, together with CO_2.

Catalyst	H_2 consumption (mol /Kg FPBO)	DOD (db.)	CO_2 production (mol/Kg FPBO)
$5Ni1Fe/Nb_2O_5$	2.5	24.5	0.61
$5Ni5Fe/Nb_2O_5$	3.9	33.1	0.40
$5Ru/Nb_2O_5$	6.4	34.9	0.93

The $5Ru/Nb_2O_5$ catalyst stands out for its hydrogen consumption rate at 6.4 mol/kg FPBO, paired with the highest CO_2 output of 0.93 mol . kg^{-1} FPBO Table 13. This profile suggests a propensity for hydrogenation, where hydrogen addition to organic compounds is a primary reaction, accompanied by significant decarboxylation, leading to carbon loss as CO_2 [152]. Although this might indicate efficient oxygen removal, the loss of carbon contradicts the objective of maximizing carbon retention in the bio-oil through the HDO process.

In contrast, the $5Ni5Fe/Nb_2O_5$ catalyst exhibits moderate hydrogen consumption at 3.9 mol/kg FPBO and the least CO_2 production at 0.40 mol/kg FPBO among the tested catalysts. This indicates deoxygenation with minimal carbon loss, aligning more closely with the goal of preserving carbon content in the bio-oil, enhancing the HDO process's carbon efficiency [152,153]. $5Ni1Fe/Nb_2O_5$ catalyst uses the least hydrogen at 2.5 mol/kg FPBO and has an intermediate level of CO_2 production at 0.61 mol . kg^{-1} FPBO. It represents a compromise between hydrogen efficiency and carbon conservation, suggesting a selective and efficient HDO process. Meanwhile, the $5Ni5Fe/Nb_2O_5$ catalyst may exhibit a preference for pathways such as hydrogenation or hydrocracking, which could explain the reduced CO_2 in its products. Furthermore, the higher hydrogen uptake and water formation by the $5Ni5Fe/Nb_2O_5$ catalyst imply more robust hydrogenation activities, enhancing the saturation of oxygenated compounds and leading to more water production, thereby achieving greater deoxygenation.

Adding to this, the Degree of Deoxygenation (DOD) values underscore the efficacy of all catalysts in oxygen removal. Nevertheless, the elevated hydrogen and CO_2 figures for the $5Ru/Nb_2O_5$ hint at a lower Yield for deoxygenation without carbon loss.

Conversely, the 5Ni5Fe/Nb_2O_5 demonstrates an optimal balance of hydrogen usage and CO_2 output, hinting at a more carbon-conservative approach to HDO. This analysis indicates that while all catalysts are effective, the 5Ni5Fe/Nb_2O_5 catalyst may offer a more sustainable route in bio-oil upgrading by prioritizing carbon efficiency.

The evaluation of specific functional groups in the upgraded products was carried out using ^{1}H-NMR spectroscopy, a method well-suited for analyzing complex mixtures like fast pyrolysis bio-oil. The observed shifts in proton concentration highlight the catalysts' efficiency in reducing oxygenated functional groups and promoting hydrocarbon formation.

FIGURE 31 Concentration of protons in 1H-NMR spectral regions for feed and HDO upgraded products

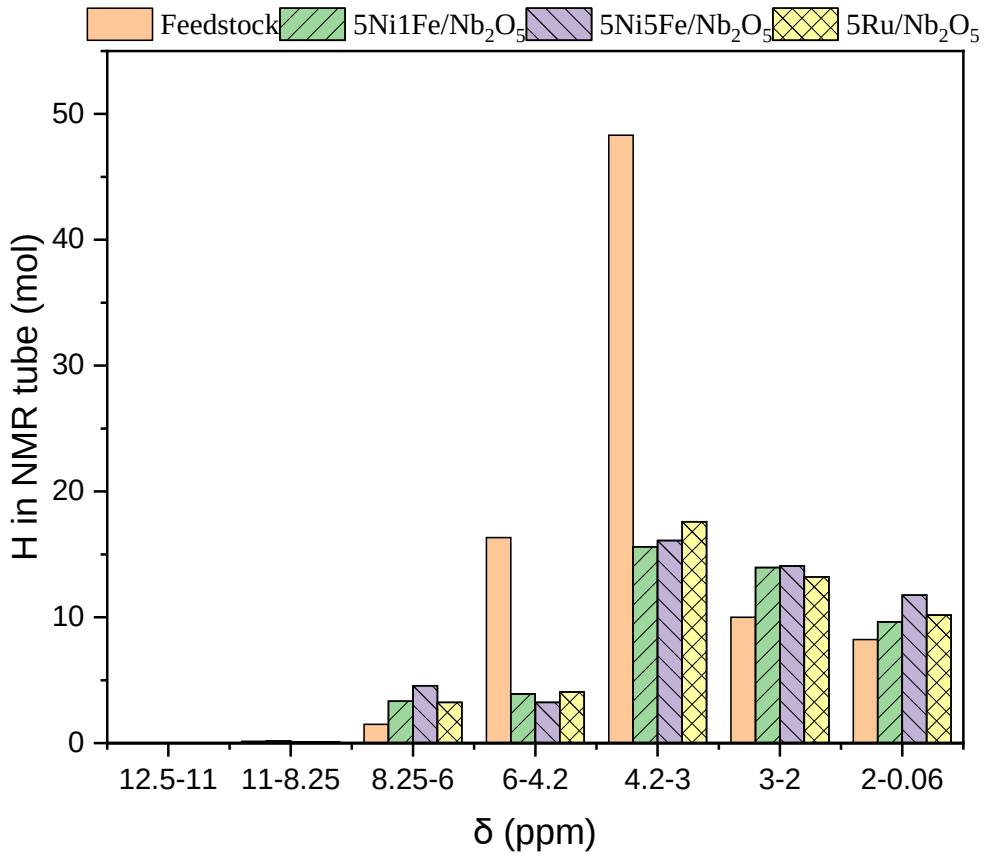

Carboxylic acid protons (12.5−11 ppm) were not detected in either the feedstock or upgraded oils, indicating their very low presence or complete conversion via decarboxylation. Aldehyde and aromatic hydroxyl protons (11−8.25 ppm) were present in minimal concentrations (0.139 mol in the feedstock), and given the high reactivity of

aldehydes [154,155], they underwent hydrogenation or other transformations under the applied conditions.

In the 8.25−6 ppm range, associated with aromatic and conjugated double-bond protons, the feedstock exhibited a concentration of 1.49 mol, which increased in the upgraded oils. This trend is explained by the low polarity of these functional groups, which results in a higher solubility in the organic phase, as previously noted by Campos-Fraga et al. (2022) [156].

For the 6−4.2 ppm range, which corresponds to non-conjugated −C=C− and aryl −CH2−O− groups, the feedstock had a high proton concentration (16.34 mol), but this dropped significantly in the upgraded oils. The 5Ni1Fe/Nb_2O_5 (3.90 mol) and 5Ni5Fe/Nb_2O_5 (3.24 mol) catalysts exhibited the largest decreases, indicating extensive hydrogenation and cleavage of non-conjugated double bonds and ether linkages. Similar behavior was reported by Campos-Fraga et al. (2022) [[102] and Kim et al. (2015) [157], where an increase in Fe loading enhanced the hydrogenation of conjugated and non-conjugated double bonds, reducing the number of protons in this region.

In the 4.2−3 ppm range, dominated by ether (−CH_2−O) and methoxy (−OCH_3) groups, the feedstock showed a high concentration (48.31 mol). This value decreased in the upgraded oils. The significant reduction reflects the hydrogenolysis of methoxy and ether groups, essential for deoxygenation. 5Ru/Nb2O5 retained the highest proton concentration in this range, suggesting a lower hydrogenolysis activity compared to the other catalysts.

In the 3.0−2.0 ppm range, which corresponds to aliphatic protons adjacent to carbonyls and methyl groups of acetic acid, the Ni-Fe catalysts exhibited the highest proton concentrations, indicating efficient hydrogenation of oxygenated intermediates into secondary alcohols, as also observed by Kim et al. (2015). Finally, in the 2.0−0.06 ppm region, representing aliphatic protons in fully saturated hydrocarbons, all upgraded oils showed significant increases. The 5Ni1Fe/Nb_2O_5 catalyst exhibited the highest proton concentration (11.76 mol), highlighting its strong hydrogenation and hydrodeoxygenation activity. The 5Ru/Nb_2O_5 catalyst (10.18 mol) retained slightly more oxygenated functionalities, suggesting a less extensive hydrogenation compared to Ni-Fe catalysts.

5.4. CONCLUSION

Elemental composition analysis by ICP and EDS confirmed the successful impregnation of metals on the catalysts. However, a discrepancy in the expected ruthenium content for 5Ru/Nb_2O_5 suggests challenges in the impregnation process, potentially due to metal-support interactions affecting metal deposition. The post-calcination SEM analysis of the Nb_2O_5 support revealed significant morphological transformations, including increased porosity and more uniform particle size distribution, which enhance catalytic performance by improving metal dispersion and accessibility of active sites.

In the FPBO experiments, the 5Ni5Fe/Nb_2O_5 catalyst demonstrated the best balance between deoxygenation efficiency and carbon retention, making it the most promising candidate for bio-oil upgrading. It effectively removed oxygen while maintaining a high carbon content, a critical factor for preserving the energy value of the upgraded oil. Its moderate hydrogen consumption and low CO_2 production indicate a more selective HDO process that minimizes unnecessary carbon loss. This, combined with its superior deoxygenation efficiency—evidenced by the lowest O/C ratio achieved—positions 5Ni5Fe/Nb_2O_5 as the most efficient and sustainable catalyst tested.

The 5Ru/Nb_2O_5 catalyst, while achieving the highest degree of deoxygenation (DOD), exhibited elevated hydrogen consumption and CO_2 production, suggesting a less selective deoxygenation pathway with extensive decarboxylation. Although this catalyst effectively removed oxygen, its higher carbon loss and hydrogen demand may limit its practical efficiency compared to Ni-Fe catalysts. The results suggest that Nb_2O_5 acidity played a key role in enhancing both direct deoxygenation (DDO) and hydrogenation pathways, contributing to the performance differences observed between the catalysts.

In this study, Nb_2O_5-supported Ni-Fe and Ru catalysts were evaluated model compound (guaiacol) and real bio-oil hydrodeoxygenation reactions. While both processes aimed to remove oxygen from the feedstock to enhance fuel properties, the results differed significantly due to the inherent complexity of FPBO compared to guaiacol. In the guaiacol HDO (previous chapter), 5Ni1Fe/Nb_2O_5 exhibited high hydrogenation activity, leading to selective production of cyclohexanol and cyclohexane. However, when tested with FPBO, the 5Ni5Fe/Nb_2O_5 catalyst emerged as the best-

performing system, achieving an optimal balance between oxygen removal, carbon retention, and hydrogen consumption. The differences observed suggest that while guaiacol HDO provides valuable insights into reaction pathways, the catalytic behavior can shift when processing complex bio-oil mixtures, where competitive adsorption, additional oxygenated functionalities, and varying molecular weights influence deoxygenation selectivity.

CHAPTER 6

EVALUATION OF NIOBIUM-BASED PERFORMANCE CATALYSTS IN A PILOT PLANT CONTINUOUS LIQUID-PHASE HDO REACTION

6.1. MOTIVATION

At the Federal University of Uberlandia (UFU) in Brazil, extensive research has been conducted on a laboratory scale to develop and evaluate various Nb_2O_5-supported catalysts for the hydrodeoxygenation (HDO) of guaiacol in the gas phase (300 °C, ambient pressure). Among the tested formulations, bimetallic Ni-Fe catalysts supported on Nb_2O_5 have demonstrated promising results, achieving high conversion rates with selectivity towards phenol and benzene, while also exhibiting low hydrogen consumption—a crucial factor for improving process efficiency. However, this gas-phase study is still ongoing and is therefore not included in this thesis. Nonetheless, the findings from Chapter 4, where the Ni-Fe catalysts supported on Nb_2O_5 were validated using SiO_2 as a reference, serve as an essential foundation for advancing the research into a liquid-phase continuous HDO system.

As part of the BRISK2 (Biofuels Research Infrastructure) program and a collaboration with the Karlsruhe Institute of Technology (KIT), a research period was conducted at the Institut für Katalyseforschung und -Technologie (IKFT) to scale up these investigations from laboratory-scale experiments to a continuous reactor setup. This transition necessitated modifications to the catalyst formulation, including adapting the catalysts into pellet form to ensure compatibility with continuous operation. The Nb_2O_5 pellets, supplied by CBMM (Companhia Brasileira de Metalurgia e Mineração), were impregnated with Ni-Fe and Ru and subsequently characterized to assess their physical and chemical properties before catalytic testing.

To optimize the pilot-scale continuous trickle-bed reactor, a commercial Ru/C catalyst (5% Ru, grains, KaiDa Technology, UK) was initially used as a benchmark. Ruthenium's noble metal properties and lower reduction temperature were considered advantageous for continuous reactor operation. Following this preliminary evaluation,

the Nb_2O_5-based catalysts were tested first in a batch reactor and later in the trickle-bed reactor to assess their efficiency and stability under continuous flow conditions.

This chapter focuses on the parametrization and optimization of the continuous reactor system, evaluating the performance of Nb_2O_5 as a catalyst support in comparison with the commercial Ru/C catalyst. The results obtained during the research period at KIT provide crucial insights into the scalability and practical application of Nb_2O_5-based catalysts for liquid-phase bio-oil upgrading.

6.2 EXPERIMENTAL METHODS (Summary)

In this study, 5Ni1Fe/Nb_2O_5 and 5Ru/Nb_2O_5 catalysts were prepared via wet impregnation using Nb_2O_5 in pellet form, supplied by CBMM. The catalysts were calcined at 500°C before characterization, which included ICP-OES for bulk metal composition and EDS for surface metal distribution. The BET surface area was determined to assess porosity, and XRD was used to confirm crystalline phases. The H_2-TPR technique was employed to evaluate the reducibility of metal species, while SEM imaging was used to examine catalyst morphology and metal dispersion.

The experiments were carried out in a trickle-bed continuous reactor, with an initial optimization phase using a commercial Ru/C catalyst to adjust parameters such as pressure, hydrogen flow, and temperature control. The final catalytic tests were conducted using 5Ni1Fe/Nb_2O_5 and 5Ru/Nb_2O_5 with a guaiacol solution in decalin as feedstock. The reactor operated at 300°C, with a 300 bar pressure, a liquid flow rate of 300 mL/h, and an H_2 flow rate of 0.4 mol/h. The weight hourly space velocity (WHSV) was set at 5 h^{-1} to optimize conversion while avoiding overheating.

The reaction products were analyzed using GC-FID and GC-MS to determine conversion rates and product selectivity. Hydrogen consumption was estimated based on process conditions, while the conversion and selectivity trends were evaluated to compare the performance of Ru and Ni-Fe catalysts under continuous HDO conditions.

6.3. RESULTS AND DISCUSSION

6.3.1. CATALYST CHARACTERIZATION

The metal loading and impregnation processes for the catalysts are detailed in Table 14. Both the 5Ni1Fe/Nb_2O_5 and 5Ru/Nb_2O_5 catalysts were prepared using Nb_2O_5 in pellet form. However, challenges were encountered in the impregnation of Ru, both on powder and pellet supports, reflecting similar difficulties observed in Chapter 5.

To verify the metal distribution on the surface of the pellets, EDS analysis was conducted. However, discrepancies were noted between the metal loadings obtained by ICP-OES (representing bulk composition) and EDS (representing surface composition). EDS results revealed a higher concentration of metals on the surface, a phenomenon commonly associated with the wet impregnation technique. This suggests that the impregnation process resulted in an enrichment of metals at the pellet surface.

For 5Ru/Nb_2O_5, ICP-OES analysis indicated a bulk Ru content of 1.32 wt. %, while EDS showed a significantly higher Ru concentration (7.44 wt. %) on the pellet surface. This disparity suggests that Ru was not homogeneously distributed throughout the Nb_2O_5 support, potentially impacting its long-term catalytic performance due to localized Ru enrichment and possible sintering effects.

Similarly, for 5Ni1Fe/Nb_2O_5, ICP-OES analysis indicated 4.8 wt. % Ni and 0.9 wt. % Fe, whereas EDS showed notably higher surface concentrations (8.9 wt. % Ni and 8.5 wt. % Fe). This suggests that Fe, despite its lower bulk content, was preferentially concentrated on the catalyst surface.

TABLE 14. Surface composition via ICP-OES and REM/EDS.

	Composition by ICP (wt. %)				**Composition by REM/EDS (wt. %)**					
	Ru	**Ni**	**Fe**	**Nb**	**Ru**	**Ni**	**Fe**	**Nb**	**O**	**C**
Pellet 5% Ru/Nb_2O_5	1.32	-	-	63.05	7.44	-	-	61.8	19.5	11.7
Pellet 5Ni1Fe/Nb_2O_5	-	4.8	0.9	60.1	-	8.9	8.5	51.6	19.56	11.4
Pellet Nb_2O_5	-	-	-	61.1	-	-	-	52.8	20	27.2

The discussion on wet impregnation brings attention to the critical aspects influencing the formation and dispersion of catalysts on porous supports, particularly when utilizing pellet-shaped impregnated support. Throughout the impregnation

process, the evidence of black liquid containing remnants of the Ru precursor indicates the challenge of retaining all the impregnated material. The lack of a strong interaction leads to precursor mobility, causing agglomeration as the solvent evaporates [158].

According with Komiyama 1985 [159], liquid-phase impregnation involves depositing small crystallites of catalyst precursors on the support's internal surface during impregnation and subsequent drying. However, these processes may not reach equilibrium, resulting in non-uniform impregnation profiles along the support pellet's radius. In cases where the reaction is mass-transfer limited, depositing the catalytic constituent closer to the external surface is desirable. Conversely, a uniformly distributed profile is preferred when the reaction is kinetically limited.

Carbon is often utilized as a binder to form pellets, as indicated by Bui et al., (2022) [160]. However, the inclusion of carbon can complicate the impregnation process and influence the catalyst's morphology. Scanning Electron Microscopy (SEM) images, detailed in Figure 32Figure 33, were used to examine the morphology of the pellet-shaped catalyst. In the SEM image displaying the support, a dark and flat surface is observed. Subsequent EDS analysis confirmed that these dark areas represent carbon.

FIGURE 32. Nb_2O_5 pellet SEM and EDS image

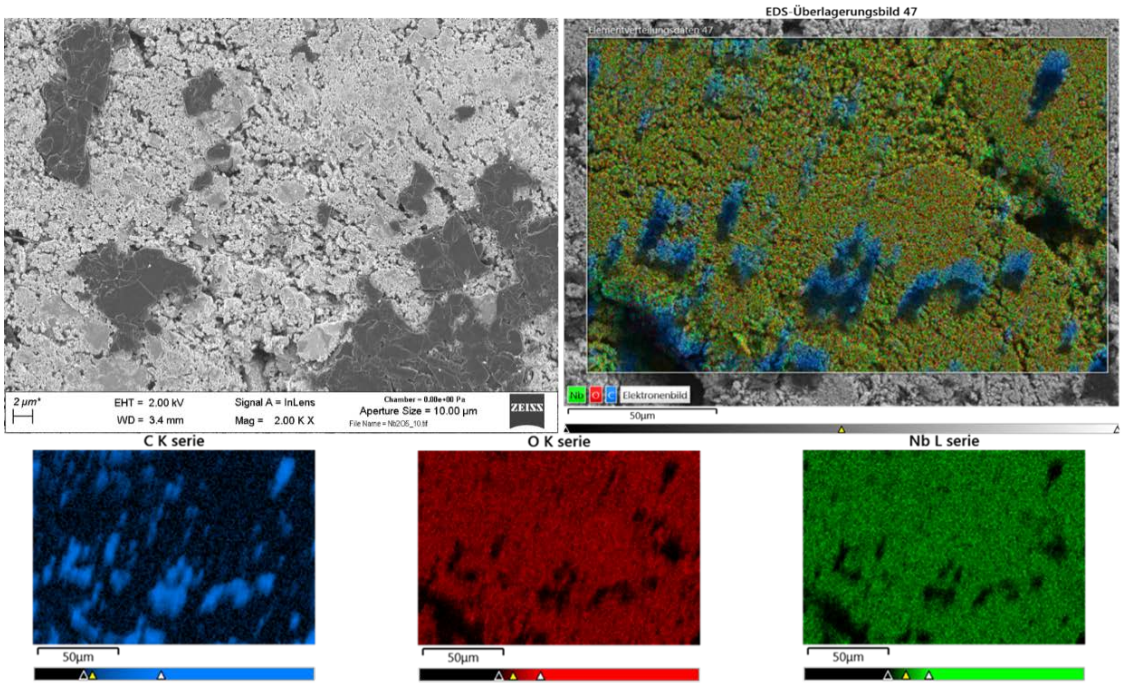

Following calcination at 500 °C and metal impregnation, SEM images reveal the presence of metals on the surface of the pellets (Figure 33). The figure displays the pellet post-calcination on the left side, with the upper right showing 5Ni-1Fe/Nb_2O_5 and the lower right showing 5Ru/Nb_2O_5. Notably, a flat surface can be observed, resulting from the pellet preparation method, tabletization, which employs pressure to shape the pellet, potentially leading to surface alterations.

FIGURE 33. SEM images of pellet after calcination and the prepared catalysts on the right.

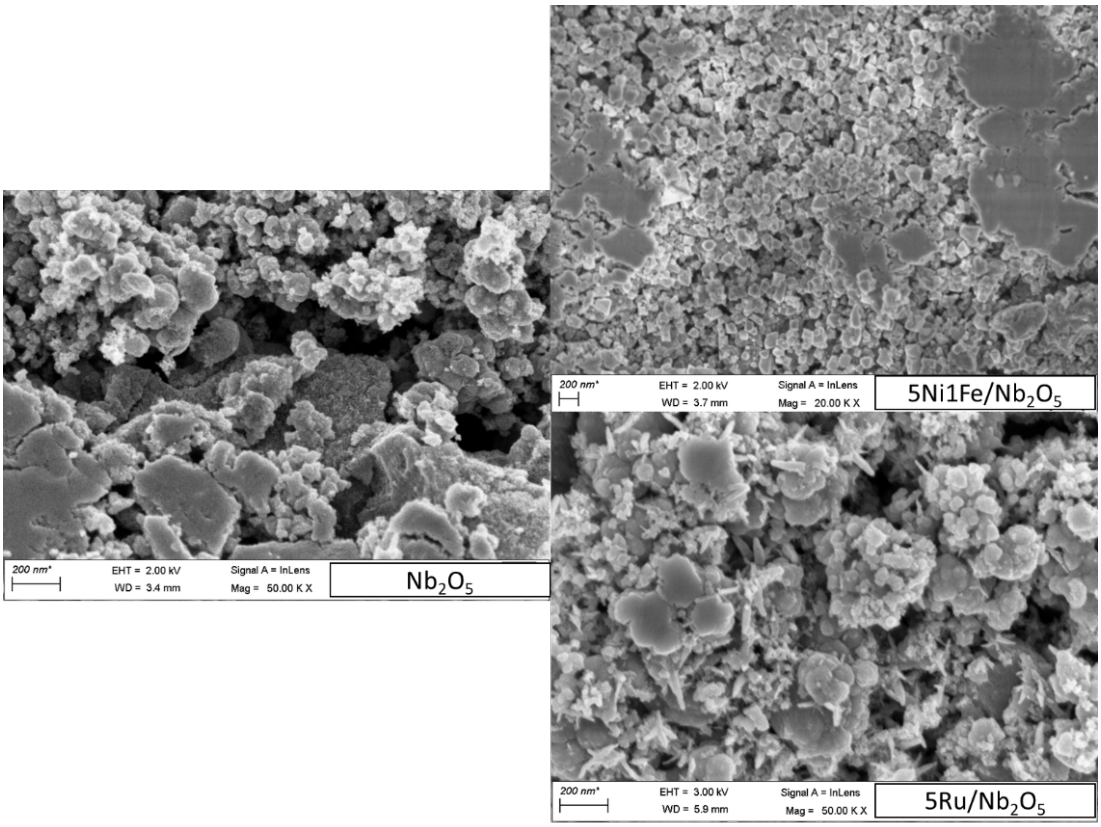

TABLE 15. Textured properties of the Nb_2O_5 support pellet before and after calcination.

Sample	[a]S_{BET} (m^2/g)	[b]S_{Meso} (m^2/g)	[c]V_{Total} (cm^3/g)	[d]V_{Meso} (cm^3/g)	[e]D (nm)
Pellet not calcined	115.27	109.86	0.16	0.16	6.28
Pellet calcined	85.78	84.68	0.14	0.14	7.04

[a]Specific surface area determined by the method Brunauer–Emmett–Teller (BET). [b]Mesoporous area calculated by t-plot method. [c]Total pore volume

measured by the amount of N_2 adsorbed at a relative pressure close to unity (P/P_0 = 0.995). [d]Mesoporous volume area measured by t-plot method. [e]Average pore diameter calculated by the Barrett–Joyner–Halenda (BJH) adsorption method.

Before calcination, the support pellet exhibits a specific surface area (S_{BET}) of 115.27 m^2/g and a mesoporous area (S_{Meso}) of 109.86 m^2/g, indicating a high proportion of mesopores within its structure. The total pore volume (V_{Total}) is measured at 0.16 cm^3/g, with the mesoporous volume (V_{Meso}) also at 0.16 cm^3/g, suggesting that the mesopores contribute significantly to the total pore volume. The average pore diameter (D), calculated using the Barrett–Joyner–Halenda (BJH) method, is 6.28 nm, falling within the mesoporous range (2-50 nm), confirming the mesoporous nature of the uncalcined pellet.

After calcination, there is a noticeable reduction in both the specific surface area and the mesoporous area, with values decreasing to 85.78 $m^2. g^{-1}$ and 84.68 $m^2. g^{-1}$, respectively. This reduction suggests that calcination leads to a collapse of some mesoporous structures or to the sintering of the material, which results in a decrease in surface area and pore volume. Similarly, the total and mesoporous volumes decrease to 0.14 $cm^3. g^{-1}$, and the average pore diameter increases from 6.28 nm to 7.04 nm after calcination.

XRD measurements were conducted to evaluate the crystalline structure of the Nb_2O_5 support and the impregnated catalysts. Post-calcination, the Nb_2O_5 pellet support exhibited diffraction peaks representative of the TT-Nb_2O_5 phase, consistent with CCDC reference code n° 2103847, a structure present in all prepared catalysts. Additionally, a common peak at $2\theta = 26.4°$, shared between the catalysts and Nb_2O_5 support, indicates the presence of graphite carbon, suggesting carbon deposition on the surface, which could impact the catalytic activity and yield. In the XRD analysis of the 5Ni1Fe/Nb_2O_5 catalyst, peaks indicative of NiFe, aligned with ICSD reference number n° 040334, are noted at $2\theta = 44.3°$ and 51.6°. Additionally, peaks corresponding to $FeNb_2O_6$, identified with ICSD n°047187, appear at $2\theta = 24.5°$, and 34.8°. The typical pattern for Ruthenium is identified at 2θ angles of 38.4°, 42.16°, and 44.1°.

FIGURE 34. XRD Patterns of the samples reduced and passiveted.

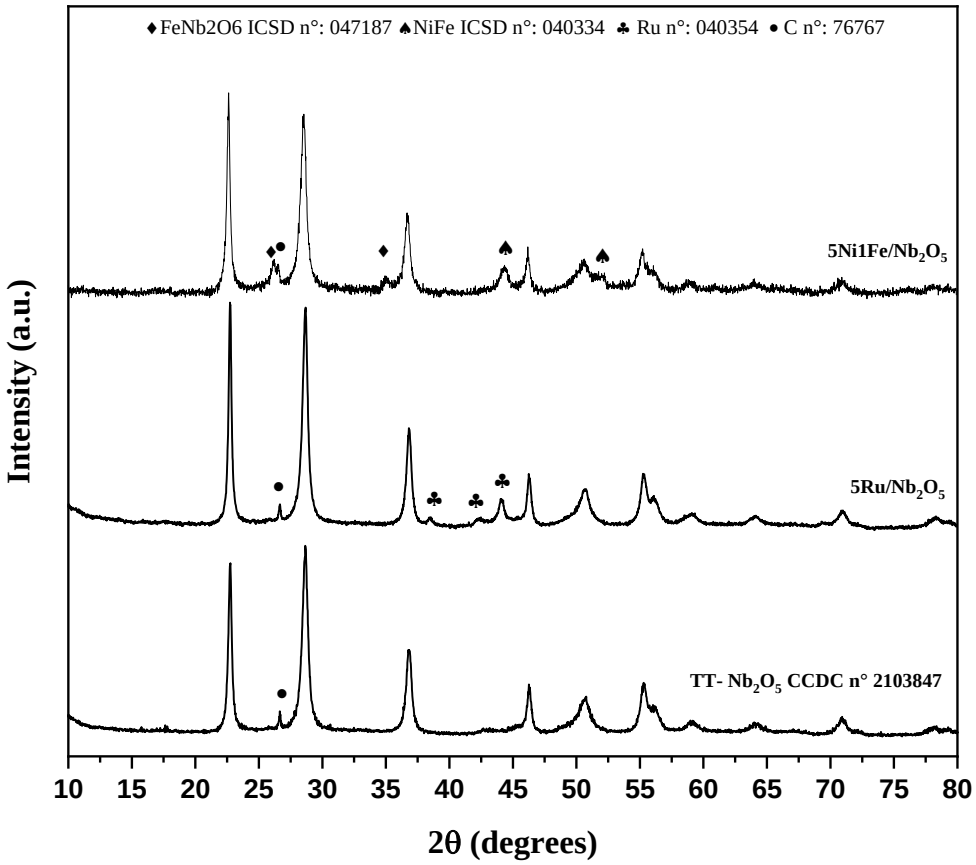

The table presents the BET surface areas and crystallite sizes of the XRD identified phases of the catalysts $5Ru/Nb_2O_5$ and $5Ni1Fe/Nb_2O_5$. The $5Ru/Nb_2O_5$ catalyst exhibits a BET surface area of 68.2 m²/g, surpassing the 56.2 m²/g surface area of the $5Ni1Fe/Nb_2O_5$ catalyst. This difference could be linked to the varying metal content: 1.32% for ruthenium in the single-metal catalyst versus a combined 6.8% for the metals in the bimetallic catalyst, as confirmed by ICP. The $5Ru/Nb_2O_5$ catalyst's ruthenium phase has a crystallite size of 22.41 nm. Conversely, the $5Ni1Fe/Nb_2O_5$ catalyst displays crystallite sizes of 32.4 nm for the $FeNb_2O_6$ phase and 34.1 nm for the NiFe phase.

TABLE 16. BET surface area and crystallite sizes (τ) of Ru and Ni-Fe based phases in Nb_2O_5-supported catalysts.

Sample	BET Surface area m^2/g	τ (nm)		
		Ru	FeNb2O6	NiFe
$5Ru/Nb_2O_5$	68.2	22.41		
$5Ni5Fe/Nb_2O_5$	56.2		32.4	34.1

The H_2-TPR profile (Figure 35) of the catalysts display single peaks of H_2 consumption related to the reduction of Ru on Ru/Nb_2O_5, observed at approximately 203 °C for the pellet. In the profile of $5Ru/Nb_2O_5$, only a strong and sharp reduction peak typically attributed to the reduction of highly dispersed RuO_2 clusters interacting with Nb_2O_5. The catalysts displayed a narrow peak, indicating the homogeneity of Ru species. However, compared to previously reported Ru/Nb_2O_5 catalysts, the reduction temperature observed in this study was higher. This discrepancy could be attributed to the strong interaction between metallic Ru and the support, influencing the reduction behavior and requiring a higher temperature for the reduction process. Additionally, setting the reduction temperature at 250 °C ensures the reduction of all Ru oxides to active metallic Ru [79,144,161,162].

For the $5Ni1Fe/Nb_2O_5$ catalyst, a pronounced and broad peak is observed at 580 °C, associated with the reduction of the Ni alloy, alongside a smaller peak at 353 °C, corresponding to the conversion of α-Fe_2O_3 to magnetite (Fe_3O_4), as supported by Sirikulbodee et al. (2022). [124]. Furthermore, the extensive peak at the higher temperature (580 °C) could be attributed to the simultaneous reduction of NiO and Fe_2O_3, which exhibit a strong interaction with the support, indicative of the formation of an Ni-Fe alloy. This pattern of reduction suggests a considerable influence of the support on the catalyst's reduction behavior and the alloy formation process [26].

FIGURE 35. TPR of samples in pellets

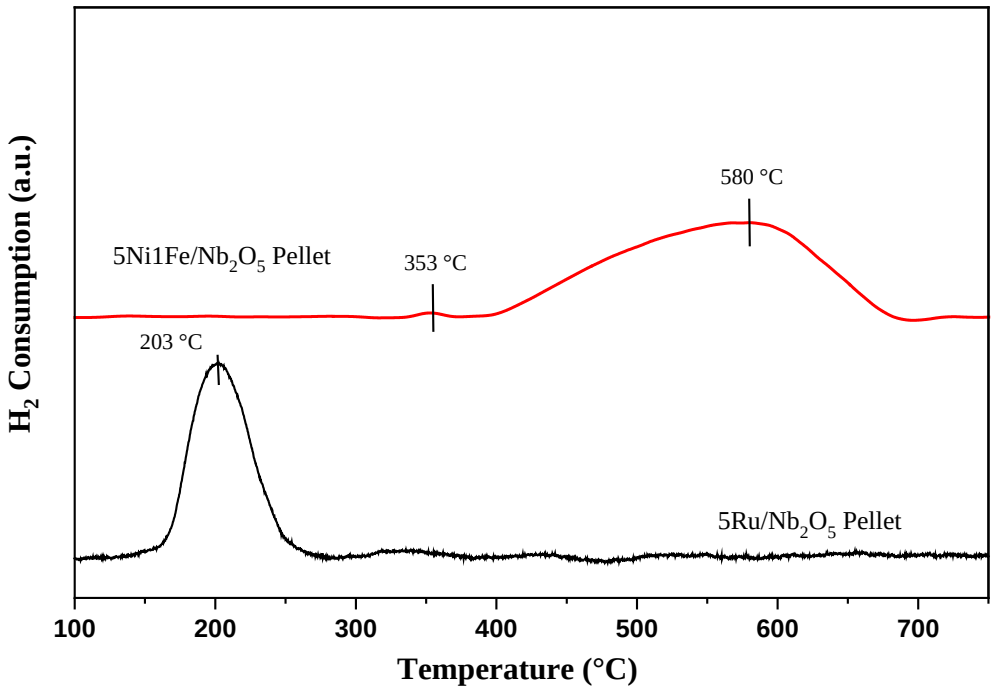

6.3.2. REACTOR OPTIMIZATION USING COMMERCIAL CATALYST WITH MODEL SUBSTANCE

The catalytic tests in the continuous reactor provided insights into the performance of different catalyst compositions and operating conditions. To optimize reactor conditions, including pressure, temperature and flow, initial tests were conducted using a well-established commercial catalyst, Ru/C, known for its reliable performance. In the first test, the use of 36.5 g of commercial 5% Ru/C with a 1:1 (wt.%) dilution of catalyst to inert SiO_2 at a WHSV of 1.4 h^{-1} resulted in reactor overheating at 300 °C, indicating a potential limitation in the system's thermal management. In response, the second test involved reducing the catalyst amount to 8 g with 58 g of SiO_2, and a higher WHSV of 5 h^{-1}. While overheating still occurred at 300 °C, it was less intense, suggesting a potential improvement in heat dissipation (Figure 36).

FIGURE 36. Conversion of guaiacol in different WHSV, in black with 36.5 g of Ru/C catalyst WHSV of 1.4 h^{-1} and in red and blue with 8g of Ru/C and WHSV of 5 h^{-1}.

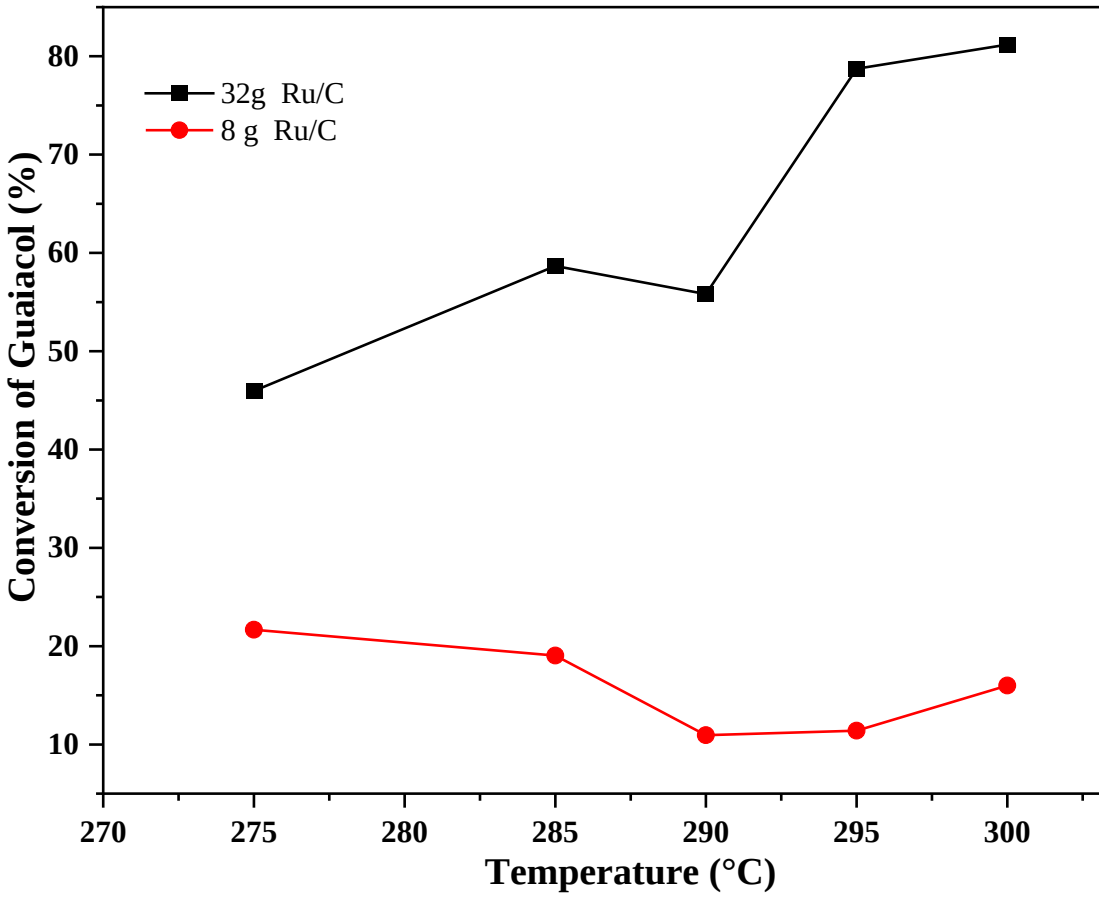

In the initial HDO system trials, as depicted in Figure 36, a higher catalyst load led to a substantial increase in conversion. However, this was accompanied by system overheating—a scenario less than ideal for sustainable operations. To address this, targeted strategies were employed to enhance system control and conversion efficiency while mitigating overheating and reducing the amount of catalyst used. Figure 37 illustrates the outcome of implementing these strategies. By incorporating a filter to prevent valve blockages, optimizing liquid and gas flows, and installing a new pressure-relief system, the system operated with less fluctuation and more consistency. A newly introduced compressor with advanced control for hydrogen flow further stabilized the process. These enhancements successfully increased the conversion rate at a constant WHSV of 5 h^{-1} with just 8 grams of catalyst, thus demonstrating that system

optimization can lead to improved performance without the drawbacks observed in the initial setup.

FIGURE 37. Conversion of guaiacol with 8 g of catalyst and WHSV of 5 h^{-1} before and after improvements of the rector setup.

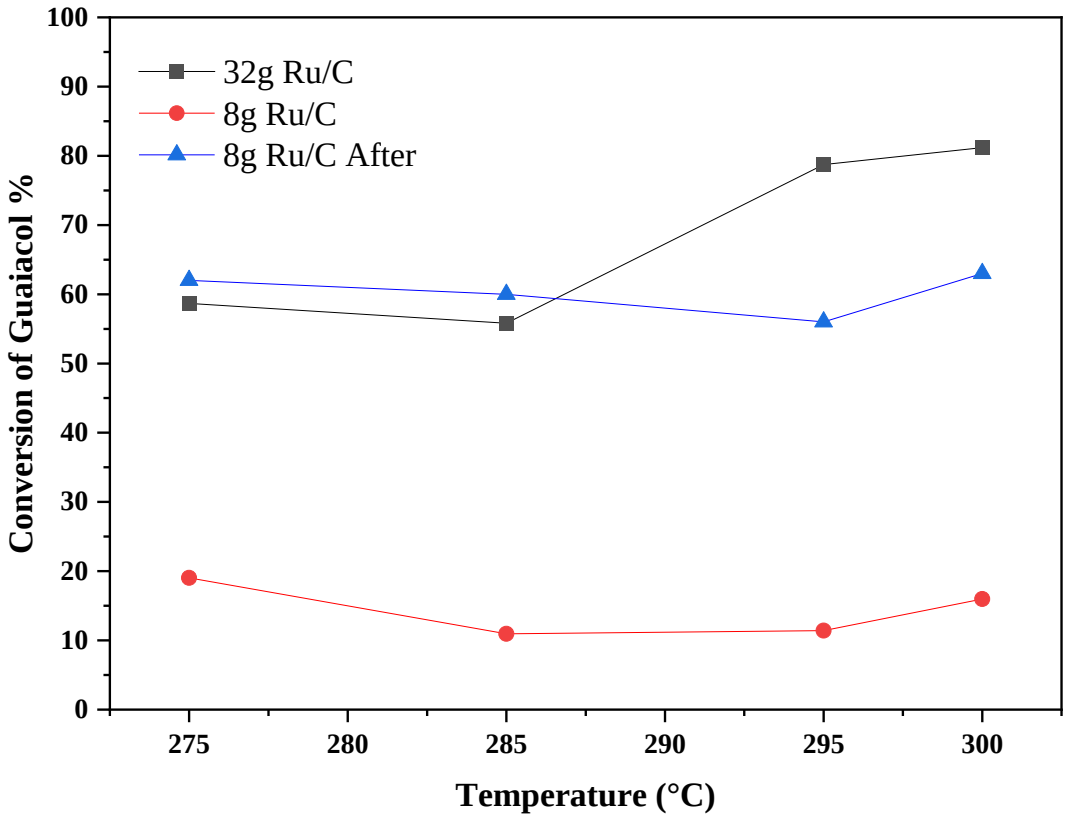

6.3.3 PILOT PLANT TESTING IN TRICKLE-BED REACTOR – CATALYSTS TESTS

Following the system optimizations, the prepared catalysts were tested in the continuous reactor using a guaiacol solution in decalin. The reactor operated at 300 °C, with a liquid flow rate of 300 mL/h and an H_2 flow rate of 0.4 mol/h, under a pressure of 300 bar. The Weight Hourly Space Velocity (WHSV) was maintained at 5 h^{-1} to assess catalyst performance under these conditions.

The conversion rates of guaiacol observed (Figure 38) for both catalysts in the continuous reactor, which vary between 55.3% and 24.5%, reflect the operational conditions implemented, notably the WSHV settings. The chosen WSHV aimed to prevent overheating and optimize the hydrogenation process. Initially, the 5Ni-

1Fe/Nb_2O_5 catalyst demonstrates a high conversion rate exceeding 55.3% at half an hour, which decreases to approximately 33% at one and a half hours and subsequently rises close to 40%. Similarly, the 5Ru/Nb_2O_5 catalyst begins with a conversion rate above 27.2%. Like the 5Ni1Fe/Nb_2O_5, the conversion for the 5Ru/Nb_2O_5 increases after 1.5 hours of reaction due to the heating control mechanism of the reactor. Given that HDO reactions are exothermic, the system's temperature must be managed to maintain steady conditions. However, this temperature regulation is gradual, causing a significant reaction rate at this stage, which results in increased conversions. The reaction is halted after 2.5 hours for safety concerns.

FIGURE 38. Conversion of Guaiacol and products Yield (%) as a function of time on stream (TOS) of HDO in the continuous reactor with Pellet catalyst

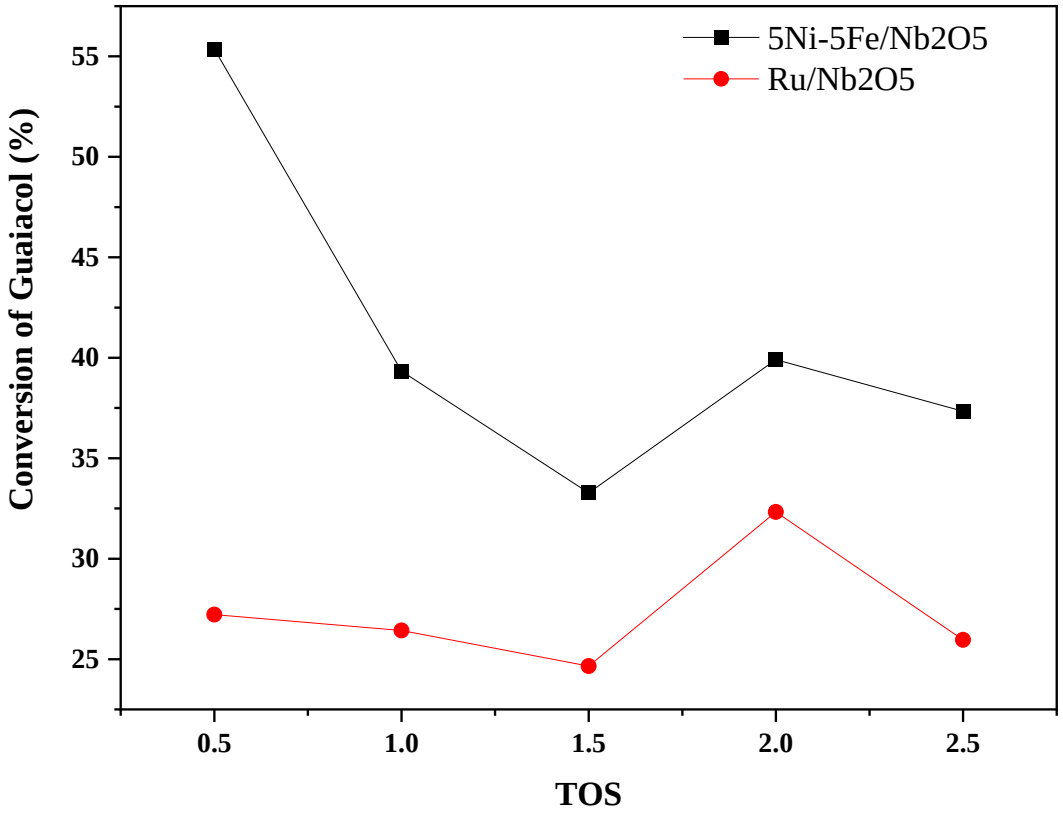

To compare the yield at a comparable level of guaiacol conversion, around 30%, the performance of both catalysts was evaluated. The 5Ni1Fe/Nb_2O_5 catalyst achieved a guaiacol conversion of 32.33%. The distribution of reaction products reveals a strong preference for cyclohexanol (60.4%) and cyclohexanone (30.3%), indicating that the reaction is primarily driven by hydrogenation. This preference for hydrogenated products can be attributed to the high hydrogen pressure used during the reaction, which

leads to increased hydrogen consumption without a corresponding significant decrease in oxygen content. This suggests that under these conditions, hydrogenation reactions are favored over hydrodeoxygenation, according to findings by Schmitt et al. (2018) [154].

TABLE 17. Yield of the Catalysts $5Ru/Nb_2O_5$ and $5Ni5Fe/Nb_2O_5$ under approximately 30% of Guaiacol conversion.

Catalyst	Cyclohexanone	Cyclohexanol	Cyclohexane	Methanol	Phenol	Catechol
$5Ru/Nb_2O_5$	53.7	43.3	2.1	-	-	-
$5Ni1Fe/Nb_2O_5$	30.3	60.4	-	2.8	3.3	3.4

The yield data for the $5Ru/Nb_2O_5$ catalyst exhibits a significant yield towards cyclohexanone (53.7 %) and cyclohexanol (43.3 %). These two products are indicative of the hydrogenation of guaiacol, suggesting that this pathway is effectively facilitated by the $5Ru/Nb_2O_5$ catalyst. The higher yield for cyclohexanone over cyclohexanol could imply that the ketone formation is favored under the reaction conditions employed. The yield towards cyclohexane is quite low (2.1%), which might suggest that the complete hydrogenation of the ring to form cyclohexane is not the preferred pathway under the given conditions. The catalyst yield profile with high values for cyclohexanone and cyclohexanol is indicative of a catalyst that is proficient in the hydrogenation steps, but less so in the complete saturation to cyclohexane [80].

The exploration of HDO of lignin-derived pyrolysis oils under continuous-flow conditions, particularly in high-pressure trickle-bed reactors, represents an evolving research field with significant industrial implications. This study contributes to the advancement of Nb_2O_5-supported catalysts in continuous-flow HDO processes, providing valuable insights into their performance and selectivity trends. Future investigations should further explore the optimization of reaction conditions and catalyst formulation to maximize oxygen removal while minimizing hydrogen consumption and carbon loss, improving the viability of bio-oil upgrading technologies.

6.4. CONCLUSION

This study, conducted between the Federal University of Uberlândia and the Karlsruher Institut für Technologie (KIT), demonstrated the promising performance of bimetallic Ni-Fe catalysts supported on Nb_2O_5 in the hydrodeoxygenation (HDO) process. These catalysts achieved high conversion rates, good selectivity for desired products, and efficient hydrogen utilization, making them good candidates for upgrading bio-oil into more stable liquid fuels.

The initial tests in the pilot-scale HDO reactor using commercial catalysts were essential for adjusting pressure, hydrogen flow, and temperature control, leading to a more stable and efficient operation. The transition from batch to continuous flow processing highlighted the importance of optimizing WHSV and preventing overheating to ensure process stability.

The synthesis of catalysts using Nb_2O_5 pellets as support and ruthenium as the active phase faced challenges, resulting in lower-than-expected metal loading. Despite this, the tests confirmed that Ru-based catalysts exhibited strong hydrogenation activity, effectively facilitating selective oxygen removal. Among the tested catalysts, 5Ni1Fe/Nb_2O_5 stood out, delivering higher conversion and a balanced hydrogenation and deoxygenation performance, reinforcing the synergistic effect between Ni and Fe.

The comparison between Ni-Fe catalysts and Ru catalysts offered important findings into their performance under continuous HDO conditions. The results highlight the potential of Nb_2O_5 as a catalytic support and support the use of transition metal-based catalysts as cost-effective alternatives to noble metal catalysts. The transition from laboratory-scale to pilot plant operations represents a significant step toward large-scale application, contributing to the development of low-carbon renewable fuels from lignin-derived bio-oils.

CHAPTER 7

CONCLUSION

This thesis presents a detailed investigation of the hydrodeoxygenation process, focusing on the efficiency of different catalysts for bio-oil upgrading. Using guaiacol as a model compound for lignin-derived bio-oils, the study aimed to gain a deeper understanding of reaction mechanisms, catalyst behavior, and deoxygenation pathways. Through a series of experiments, this work evaluates the performance of Ni-Fe bimetallic catalysts supported on niobia for the upgrading of bio-oil, providing key insights into catalyst behavior, deoxygenation pathways, and process optimization.

The study first examined the HDO of guaiacol to investigate catalytic reaction pathways and metal-support interactions, testing Ni and Fe catalysts in both monometallic and bimetallic forms. The results highlighted the superior performance of the bimetallic 5Ni1Fe/Nb_2O_5 catalyst, attributed to the synergistic interaction between Ni and Fe. This research also emphasized the critical role of Nb_2O_5 as a support material, influencing catalyst reducibility, selectivity, and hydrogen utilization. These insights provided a fundamental basis for understanding bio-oil upgrading, guiding the transition to more complex feedstocks in subsequent stages of the study.

Transitioning to bio-oil upgrading, the study evaluated the catalytic performance of 5Ni1Fe/Nb_2O_5 and 5Ni5Fe/Nb_2O_5, using 5Ru/Nb_2O_5 as a reference catalyst for the hydrodeoxygenation (HDO) of fast pyrolysis bio-oil (FPBO). The results revealed differences in carbon efficiency, CO_2 production, and deoxygenation performance among the catalysts. 5Ni5Fe/Nb_2O_5 demonstrated a promising balance between oxygen removal and carbon retention, making it a candidate for efficient bio-oil upgrading. In contrast, 5Ru/Nb_2O_5 exhibited high deoxygenation activity but with increased hydrogen consumption and CO_2 production, indicating a less selective deoxygenation pathway with potential carbon loss.

In the final phase of this study, the performance of Nb_2O_5-supported catalysts was evaluated in a pilot-scale continuous trickle-bed reactor to advance the application of HDO in bio-oil upgrading. The transition from batch to continuous operation required system optimization, including adjustments to pressure control, hydrogen flow, and

reactor stability, which were successfully implemented using a commercial Ru/C catalyst as a benchmark. The 5Ni1Fe/Nb_2O_5 and 5Ru/Nb_2O_5 catalysts were then tested under continuous flow conditions. 5Ni1Fe/Nb_2O_5 was selected for this stage due to its superior performance in guaiacol HDO, where it achieved high conversion and efficient deoxygenation while balancing hydrogenation and carbon retention. In the continuous reactor, 5Ni1Fe/Nb_2O_5 maintained high guaiacol conversion, favoring hydrogenation and producing cyclohexanol as the main product, whereas 5Ru/Nb_2O_5 exhibited stronger deoxygenation activity, leading to higher cyclohexanone selectivity. These findings reinforce the synergistic effect of Ni and Fe in optimizing both hydrogenation and deoxygenation reactions, while also demonstrating the high reactivity of Ru-based catalysts. The successful adaptation of Nb_2O_5-based catalysts for continuous operation marks an important step toward scaling up HDO processes, supporting the development of cost-effective and sustainable alternatives for bio-oil upgrading.

KEY OUTCOMES

- The bimetallic 5Ni1Fe/Nb_2O_5 catalyst demonstrated superior performance in guaiacol HDO, confirming the synergistic effect between Ni and Fe in promoting both hydrogenation and deoxygenation.
- In liquid-phase HDO of fast pyrolysis bio-oil (FPBO), the 5Ni5Fe/Nb_2O_5 catalyst achieved the best balance between oxygen removal and carbon retention, highlighting the distinct roles of Ni and Fe in optimizing the reaction pathways.
- System optimization in the continuous reactor improved process stability, hydrogen flow control, and temperature management, demonstrating the feasibility of scaling up Nb_2O_5-supported catalysts for industrial applications.
- The study validated Nb_2O_5 as an effective catalyst support, emphasizing its unique acidity and strong metal-support interactions, which enhance both hydrogenation and deoxygenation reactions.
- The comparative analysis of Ru and Ni-Fe catalysts established a cost-performance benchmark, positioning Ni-Fe catalysts as viable and cost-effective alternatives to noble metal-based catalysts for large-scale bio-oil upgrading.

- The successful transition from batch to continuous processing represents a crucial step toward industrial-scale HDO, reinforcing the practical potential of Nb_2O_5-supported catalysts in renewable fuel production.

OUTLOOKS

- WHSV Evaluation for Nb_2O_5 Supported Catalysts: Further investigation into the impact of WHSV on catalyst performance, especially in the continuous-flow HDO process, will be crucial. Adjusting WHSV could optimize conversion rates and Yield towards desired products, enhancing the efficiency of bio-oil upgrading processes.
- Optimization of the Continuous Trickle-Bed Reactor: Continuous efforts to optimize the trickle-bed reactor setup, particularly for bio-oil feeds, will be essential. This includes refining operational parameters, enhancing system stability, and minimizing catalyst deactivation to ensure sustainable long-term performance.
- Testing of Synthesized Pelletized Catalysts with Real Bio-Oil: The synthesized Nb_2O_5 pelletized catalysts demonstrated promising results in pilot-scale testing. Future work should focus on evaluating these catalysts with bio-oil feeds to assess their efficacy and stability under practical operating conditions.
- Temperature and Time Variations in FPBO Studies: Exploring the effects of reaction temperature and time on the HDO process, especially for the Ni-Fe catalysts, could provide deeper insights into the reaction mechanisms. This could lead to the development of catalysts with enhanced yield and activity for specific reaction pathways.
- Investigation of Catalyst Longevity and Regeneration: A critical aspect of catalyst design for commercial applications involves understanding and improving catalyst stability and longevity. Future studies should explore methods for catalyst regeneration and techniques to mitigate catalyst deactivation, particularly due to coke formation and metal leaching.
- Scale-up and Commercialization Prospects: Bridging the gap between laboratory-scale findings and commercial applications will be a key objective. This entails scaling up the HDO process, evaluating economic viability, and addressing engineering challenges associated with bio-oil upgrading at an industrial scale.
- Integration with Other Bio-refinery Processes: Exploring the integration of HDO processes with other bio-refinery operations, such as pyrolysis, gasification,

and biochemical conversion routes, could offer holistic solutions for biomass valorization, enhancing the overall efficiency and sustainability of bio-refineries.

By addressing these outlooks, future research can significantly advance the field of bio-oil upgrading, contributing to the development of sustainable and economically viable processes for converting lignin-derived feedstocks into valuable hydrocarbons.

REFERENCES

1. Paraschiv, S.; Paraschiv, L.S. Trends of Carbon Dioxide (CO2) Emissions from Fossil Fuels Combustion (Coal, Gas and Oil) in the EU Member States from 1960 to 2018. *Energy Reports* **2020**, *6*, 237–242, doi:10.1016/j.egyr.2020.11.116.

2. Jaeglé, L.; Steinberger, L.; Martin, R. V.; Chance, K. Global Partitioning of NOx Sources Using Satellite Observations: Relative Roles of Fossil Fuel Combustion, Biomass Burning and Soil Emissions. In Proceedings of the Faraday Discussions; 2005; Vol. 130, pp. 407–423.

3. Mishra, R.K.; kumar, V.; Kumar, P.; Mohanty, K. Hydrothermal Liquefaction of Biomass for Bio-Crude Production: A Review on Feedstocks, Chemical Compositions, Operating Parameters, Reaction Kinetics, Techno-Economic Study, and Life Cycle Assessment. *Fuel* **2022**, *316*, 123377, doi:10.1016/j.fuel.2022.123377.

4. Magazzino, C.; Mele, M.; Schneider, N.; Shahbaz, M. Can Biomass Energy Curtail Environmental Pollution? A Quantum Model Approach to Germany. *J Environ Manage* **2021**, *287*, 112293, doi:10.1016/j.jenvman.2021.112293.

5. Mishra, R.K.; Misra, M.; Mohanty, A.K. Value-Added Biocarbon Production through Slow Pyrolysis of Mixed Bio-Oil Wastes: Studies on Their Physicochemical Characteristics and Structure–Property–Processing Co-Relation. *Biomass Convers Biorefin* **2024**, *14*, 7887–7901, doi:10.1007/s13399-022-02906-2.

6. Gea, S.; Hutapea, Y.A.; Piliang, A.F.R.; Pulungan, A.N.; Rahayu, R.; Layla, J.; Tikoalu, A.D.; Wijaya, K.; Saputri, W.D. A Comprehensive Review of Experimental Parameters in Bio-Oil Upgrading from Pyrolysis of Biomass to Biofuel Through Catalytic Hydrodeoxygenation. *Bioenergy Res* **2023**, *16*, 325–347, doi:10.1007/s12155-022-10438-w.

7. Zasypalov, G.; Vutolkina, A.; Klimovsky, V.; Abramov, E.; Vinokurov, V.; Glotov, A. Hydrodeoxygenation of Guaiacol over Halloysite Nanotubes Decorated with Ru Nanoparticles: Effect of Alumina Acid Etching on Catalytic Behavior and Reaction Pathways. *Appl Catal B* **2024**, *342*, 123425, doi:10.1016/j.apcatb.2023.123425.

8. Tran, Q.K.; Han, S.; Ly, H.V.; Kim, S.-S.; Kim, J. Hydrodeoxygenation of a Bio-Oil Model Compound Derived from Woody Biomass Using Spray-Pyrolysis-Derived Spherical γ-Al2O3-SiO2 Catalysts. *Journal of Industrial and Engineering Chemistry* **2020**, *92*, 243–251, doi:10.1016/j.jiec.2020.09.012.

9. Mäki-Arvela, P.; Murzin, D.Y. Hydrodeoxygenation of Lignin-Derived Phenols: From Fundamental Studies towards Industrial Applications. *Catalysts* **2017**, *7*, 265, doi:10.3390/catal7090265.

10. Duong, N.N.; Teles, C.A.; Noronha, F.B.; Resasco, D.E. Non-Linear Arrhenius Behavior of m-Cresol Hydrogenation over Platinum. *Catal Letters* **2024**, *154*, 6123–6132, doi:10.1007/s10562-024-04776-x.

11. Deutsch, K.L.; Shanks, B.H. Hydrodeoxygenation of Lignin Model Compounds over a Copper Chromite Catalyst. *Appl Catal A Gen* **2012**, *447–448*, 144–150, doi:10.1016/j.apcata.2012.09.047.

12. Zhao, C.; Kasakov, S.; He, J.; Lercher, J.A. Comparison of Kinetics, Activity and Stability of Ni/HZSM-5 and Ni/Al2O3-HZSM-5 for Phenol Hydrodeoxygenation. *J Catal* **2012**, *296*, 12–23, doi:10.1016/j.jcat.2012.08.017.

13. Kang, Y.-H.; Wei, X.-Y.; Liu, G.-H.; Gao, Y.; Li, Y.-J.; Ma, X.-R.; Zhang, Z.-F.; Zong, Z.-M. Catalytic Hydroconversion of Soluble Portion in the Extraction from Hecaogou Subbituminous Coal to Clean Liquid Fuel over a Y/ZSM-5 Composite Zeolite-Supported Nickel Catalyst. *Fuel* **2020**, *269*, 117326, doi:10.1016/j.fuel.2020.117326.

14. Kim, H.; Lim, Y.H.; Park, J.H.; Ha, J.-M.; Kim, D.H. Hydrodeoxygenation of Guaiacol over Physically Mixed Co/TiO2 and WO3/TiO2 Catalysts. *Green Chemistry* **2024**, *26*, 2692–2704, doi:10.1039/D3GC04400A.

15. Lu, J.; Behtash, S.; Mamun, O.; Heyden, A. Theoretical Investigation of the Reaction Mechanism of the Guaiacol Hydrogenation over a Pt(111) Catalyst. *ACS Catal* **2015**, *5*, 2423–2435, doi:10.1021/cs5016244.

16. Xin, Y.; Zheng, Z.; Luo, Z.; Jiang, C.; Gao, S.; Wang, Z.; Zhao, C. The Influence of Pore Structures and Lewis Acid Sites on Selective Hydrogenolysis of Guaiacol to Benzene over Ru/TS-1. *Green Energy & Environment* **2022**, *7*, 1014–1023, doi:10.1016/j.gee.2020.12.024.

17. Meshkini Far, R.; Ischenko, O. V.; Dyachenko, A.G.; Bieda, O.; Gaidai, S. V.; Lisnyak, V. V. CO2 Hydrogenation into CH4 over Ni-Fe Catalysts. *Functional Materials Letters* **2018**, *11*, 3–6, doi:10.1142/S1793604718500571.

18. Han, Q.; Rehman, M.U.; Wang, J.; Rykov, A.; Gutiérrez, O.Y.; Zhao, Y.; Wang, S.; Ma, X.; Lercher, J.A. The Synergistic Effect between Ni Sites and Ni-Fe Alloy Sites on Hydrodeoxygenation of Lignin-Derived Phenols. *Appl Catal B* **2019**, *253*, 348–358, doi:10.1016/j.apcatb.2019.04.065.

19. Nie, L.; De Souza, P.M.; Noronha, F.B.; An, W.; Sooknoi, T.; Resasco, D.E. Selective Conversion of M-Cresol to Toluene over Bimetallic Ni-Fe Catalysts. *J Mol Catal A Chem* **2014**, *388–389*, 47–55, doi:10.1016/j.molcata.2013.09.029.

20. Yan, P.; Kennedy, E.; Stockenhuber, M. Hydrodeoxygenation of Guaiacol over BEA Supported Bimetallic Ni-Fe Catalysts with Varied Impregnation Sequence. *J Catal* **2021**, *404*, 1–11, doi:10.1016/j.jcat.2021.08.033.

21. Yan, P.; Kennedy, E.; Stockenhuber, M. Hydrodeoxygenation of Guaiacol over BEA Supported Bimetallic Ni-Fe Catalysts with Varied Impregnation Sequence. *J Catal* **2021**, *404*, 1–11, doi:10.1016/j.jcat.2021.08.033.

22. Yan, P.; Kennedy, E.; Stockenhuber, M. Hydrodeoxygenation of Guaiacol over BEA Supported Bimetallic Ni-Fe Catalysts with Varied Impregnation Sequence. *J Catal* **2021**, *404*, 1–11, doi:10.1016/j.jcat.2021.08.033.

23. Meng, F.; Zhong, P.; Li, Z.; Cui, X.; Zheng, H. Surface Structure and Catalytic Performance of Ni-Fe Catalyst for Low-Temperature CO Hydrogenation. *J Chem* **2014**, *2014*, doi:10.1155/2014/534842.

24. Huang, L.; Tang, F.; Liu, P.; Xiong, W.; Jia, S.; Hao, F.; Lv, Y.; Luo, H. Highly Efficient and Selective Conversion of Guaiacol to Cyclohexanol over Ni-Fe/MgAlOx: Understanding the Synergistic Effect between Ni-Fe Alloy and Basic Sites. *Fuel* **2022**, *327*, 125115, doi:10.1016/j.fuel.2022.125115.

25. Huang, L.; Tang, F.; Liu, P.; Xiong, W.; Jia, S.; Hao, F.; Lv, Y.; Luo, H. Highly Efficient and Selective Conversion of Guaiacol to Cyclohexanol over Ni-Fe/MgAlOx: Understanding the Synergistic Effect between Ni-Fe Alloy and Basic Sites. *Fuel* **2022**, *327*, 125115, doi:10.1016/j.fuel.2022.125115.

26. Zhang, Y.; Zou, X.; Liu, H.; Chen, Y.; Dong, S.; Ji, M.; Chen, D.; Xu, C.; Xie, H.; Zhu, C.; et al. Perspective on Steam Reforming of Toluene Over Mineral Supported Ni-Fe Catalysts: Essential Roles of Different Structures. *SSRN Electronic Journal* **2021**, doi:10.2139/ssrn.3950213.

27. Tian, D.; Liu, Z.; Li, D.; Shi, H.; Pan, W.; Cheng, Y. Bimetallic Ni-Fe Total-Methanation Catalyst for the Production of Substitute Natural Gas under High Pressure. *Fuel* **2013**, *104*, 224–229, doi:10.1016/j.fuel.2012.08.033.

28. Xin, H.; Yang, H.; Lei, X.; Du, X.; Zhou, K.; Li, D.; Hu, C. Ni-Fe Catalysts Supported on $γ$-Al2O3/HZSM-5 for Transformation of Palmitic Acid into Hydrocarbon Fuel. *Ind Eng Chem Res* **2020**, *59*, 17373–17386, doi:10.1021/acs.iecr.0c01937.

29. Mäkelä, E.; González Escobedo, J.L.; Neuvonen, J.; Lahtinen, J.; Lindblad, M.; Lassi, U.; Karinen, R.; Puurunen, R.L. Liquid-Phase Hydrodeoxygenation of 4-Propylphenol to Propylbenzene: Reducible Supports for Pt Catalysts. *ChemCatChem* **2020**, *12*, 4090–4104, doi:10.1002/cctc.202000429.

30. Teles, C.A.; de Souza, P.M.; Rabelo-Neto, R.C.; Teran, A.; Jacobs, G.; Vilela Weikert, C.; Magriotis, Z.M.; Gonçalves, V.O.O.; Resasco, D.E.; Noronha, F.B. Reaction Pathways for the HDO of Guaiacol over Supported Pd Catalysts: Effect of Support Type in the Deoxygenation of Hydroxyl and Methoxy Groups. *Molecular Catalysis* **2022**, *523*, 111491, doi:10.1016/j.mcat.2021.111491.

31. Silva, N.K.G.; Ribas, R.M.; Monteiro, R.S.; Barrozo, M.A. de S.; Soares, R.R. Thermodynamic Equilibrium Analysis of the Vapor Phase Hydrodeoxygenation of Guaiacol. *Renew Energy* **2020**, *147*, 947–956, doi:10.1016/j.renene.2019.09.059.

32. Silva, N.K.G.; Ferreira, R.A.R.; Ribas, R.M.; Monteiro, R.S.; Barrozo, M.A.S.; Soares, R.R. Gas-Phase Hydrodeoxygenation (HDO) of Guaiacol over Pt/Al2O3 Catalyst Promoted by Nb2O5. *Fuel* **2021**, *287*, doi:10.1016/j.fuel.2020.119509.

33. Souza, N. Estudo de Catalisadores de Níquel e Ferro Suportados Em Nióbia e Sílica Na Reação de Hidrodesoxigenação de Guaiacol, Universidade Federal de Uberlândia, 2020.

34. Birniwa, A.H.; Abdullahi, S.S.; Ali, M.; Mohammad, R.E.A.; Jagaba, A.H.; Amran, M.; Avudaiappan, S.; Maureira-Carsalade, N.; Flores, E.I.S. Recent Trends in Treatment and Fabrication of Plant-Based Fiber-Reinforced Epoxy Composite: A Review. *Journal of Composites Science* **2023**, *7*, 120, doi:10.3390/jcs7030120.

35. Bot, B.V.; Axaopoulos, P.J.; Sakellariou, E.I.; Sosso, O.T.; Tamba, J.G. Energetic and Economic Analysis of Biomass Briquettes Production from Agricultural Residues. *Appl Energy* **2022**, *321*, 119430, doi:10.1016/j.apenergy.2022.119430.

36. Sharma, S.; Kundu, A.; Basu, S.; Shetti, N.P.; Aminabhavi, T.M. Sustainable Environmental Management and Related Biofuel Technologies. *J Environ Manage* **2020**, *273*, 111096, doi:10.1016/j.jenvman.2020.111096.

37. Xie, S.; Li, Z.; Luo, S.; Zhang, W. Bioethanol to Jet Fuel: Current Status, Challenges, and Perspectives. *Renewable and Sustainable Energy Reviews* **2024**, *192*, 114240, doi:10.1016/j.rser.2023.114240.

38. Čespiva, J.; Niedzwiecki, L.; Vereš, J.; Skřínský, J.; Wnukowski, M.; Borovec, K.; Ochodek, T. Evaluation of Performance of the Unique, Cross/Updraft Type Gasification Technology with Sliding Bed Over Circular Grate. *SSRN Electronic Journal* **2022**, 1–16, doi:10.2139/ssrn.4137311.

39. Čespiva, J.; Niedzwiecki, L.; Wnukowski, M.; Krochmalny, K.; Mularski, J.; Ochodek, T.; Pawlak-Kruczek, H. Torrefaction and Gasification of Biomass for Polygeneration: Production of Biochar and Producer Gas at Low Load Conditions. *Energy Reports* **2022**, *8*, 134–144, doi:10.1016/j.egyr.2022.10.081.

40. Janoska, P. Energy Transitions Indicators – Analysis - IEA. *International Energy Agency* 2019.

41. IEA World Energy Outlook. *World Energy Outlook 2023, IEA, Paris* **2023**, 23–28.

42. International Energy Agency, I. *World Energy Outlook 2023*; 2023;

43. Bridgwater, A. V. Review of Fast Pyrolysis of Biomass and Product Upgrading. *Biomass Bioenergy* **2012**, *38*, 68–94, doi:10.1016/j.biombioe.2011.01.048.

44. Mohan, D.; Pittman, C.U.; Steele, P.H. Pyrolysis of Wood /Biomass for Bio-Oil. *Prog Energy Combust Sci* **2017**, *62*, 848–889.

45. Guedes, R.E.; Luna, A.S.; Torres, A.R. Operating Parameters for Bio-Oil Production in Biomass Pyrolysis: A Review. *J Anal Appl Pyrolysis* **2018**, *129*, 134–149, doi:10.1016/j.jaap.2017.11.019.

46. Polin, J.P.; Carr, H.D.; Whitmer, L.E.; Smith, R.G.; Brown, R.C. Conventional and Autothermal Pyrolysis of Corn Stover: Overcoming the Processing Challenges of High-Ash Agricultural Residues. *J Anal Appl Pyrolysis* **2019**, *143*, 104679, doi:10.1016/j.jaap.2019.104679.

47. Anca-Couce, A. Reaction Mechanisms and Multi-Scale Modelling of Lignocellulosic Biomass Pyrolysis. *Prog Energy Combust Sci* **2016**, *53*, 41–79, doi:10.1016/j.pecs.2015.10.002.

48. El Bari, H.; Fanezoune, C.K.; Dorneanu, B.; Arellano-Garcia, H.; Majozi, T.; Elhenawy, Y.; Bayssi, O.; Hirt, A.; Peixinho, J.; Dhahak, A.; et al. Catalytic Fast Pyrolysis of Lignocellulosic Biomass: Recent Advances and Comprehensive Overview. *J Anal Appl Pyrolysis* **2024**, *178*, 106390, doi:10.1016/j.jaap.2024.106390.

49. Hoang, A.T.; Ong, H.C.; Fattah, I.M.R.; Chong, C.T.; Cheng, C.K.; Sakthivel, R.; Ok, Y.S. Progress on the Lignocellulosic Biomass Pyrolysis for Biofuel Production toward Environmental Sustainability. *Fuel Processing Technology* **2021**, *223*, 106997, doi:10.1016/j.fuproc.2021.106997.

50. Bridgwater, A. V. Renewable Fuels and Chemicals by Thermal Processing of Biomass. *Chemical Engineering Journal* **2003**, *91*, 87–102, doi:10.1016/S1385-8947(02)00142-0.

51. Mohan, D.; Pittman, C.U.; Steele, P.H. Pyrolysis of Wood/Biomass for Bio-Oil: A Critical Review. *Energy & Fuels* **2006**, *20*, 848–889, doi:10.1021/ef0502397.

52. Xiu, S.; Shahbazi, A. Bio-Oil Production and Upgrading Research: A Review. *Renewable and Sustainable Energy Reviews* **2012**, *16*, 4406–4414, doi:10.1016/j.rser.2012.04.028.

53. Stelmach, S.; Ignasiak, K.; Czardybon, A.; Bigda, J. Evaluation of Bio-Oils in Terms of Fuel Properties. *Processes* **2023**, *11*, doi:10.3390/pr11123317.

54. Dabros, T.M.H.; Stummann, M.Z.; Høj, M.; Jensen, P.A.; Grunwaldt, J.D.; Gabrielsen, J.; Mortensen, P.M.; Jensen, A.D. Transportation Fuels from Biomass Fast Pyrolysis, Catalytic Hydrodeoxygenation, and Catalytic Fast Hydropyrolysis. *Prog Energy Combust Sci* **2018**, *68*, 268–309, doi:10.1016/j.pecs.2018.05.002.

55. Oasmaa, A.; Czernik, S. Fuel Oil Quality of Biomass Pyrolysis Oils - State of the Art for the End Users. *Energy and Fuels* **1999**, *13*, 914–921, doi:10.1021/ef980272b.

56. Abnisa, F.; Wan Daud, W.M.A. A Review on Co-Pyrolysis of Biomass: An Optional Technique to Obtain a High-Grade Pyrolysis Oil. *Energy Convers Manag* **2014**, *87*, 71–85, doi:10.1016/j.enconman.2014.07.007.

57. Mishra, R.K.; Jaya Prasanna Kumar, D.; Sankannavar, R.; Binnal, P.; Mohanty, K. Hydro-Deoxygenation of Pyrolytic Oil Derived from Pyrolysis of Lignocellulosic Biomass: A Review. *Fuel* **2024**, *360*, 130473, doi:10.1016/j.fuel.2023.130473.

58. Ruddy, D.A.; Schaidle, J.A.; Ferrell, J.R.; Wang, J.; Moens, L.; Hensley, J.E. *Recent Advances in Heterogeneous Catalysts for Bio-Oil Upgrading via "Ex Situ Catalytic Fast Pyrolysis": Catalyst Development through the Study of Model Compounds*; 2014; Vol. 16; ISBN 3033847951.

59. Bacha, J.; Freel, J.; Gibbs, A.; Gibbs, L.; Hemighaus, G.; Hoekman, K.; Horn, J.; Ingham, M.; Jossens, L.; Kohler, D.; et al. Diesel Fuels Technical Review. *Chevron Global Marketing* **2007**, 1–116.

60. Prabhudesai, V.S.; Gurrala, L.; Vinu, R. Catalytic Hydrodeoxygenation of Lignin-Derived Oxygenates: Catalysis, Mechanism, and Effect of Process Conditions. *Energy & Fuels* **2022**, *36*, 1155–1188, doi:10.1021/acs.energyfuels.1c02640.

61. Mortensen, P.M.; Grunwaldt, J.D.; Jensen, P.A.; Jensen, A.D. Screening of Catalysts for Hydrodeoxygenation of Phenol as a Model Compound for Bio-Oil. *ACS Catal* **2013**, *3*, 1774–1785, doi:10.1021/cs400266e.

62. Girgis, M.J.; Gates, B.C. Reactivities, Reaction Networks, and Kinetics in High-Pressure Catalytic Hydroprocessing. *Ind Eng Chem Res* **1991**, *30*, 2021–2058, doi:10.1021/ie00057a001.

63. Patel, M.; Kumar, A. Production of Renewable Diesel through the Hydroprocessing of Lignocellulosic Biomass-Derived Bio-Oil: A Review. *Renewable and Sustainable Energy Reviews* **2016**, *58*, 1293–1307, doi:10.1016/j.rser.2015.12.146.

64. Barrios, A.M.; Teles, C.A.; de Souza, P.M.; Rabelo-Neto, R.C.; Jacobs, G.; Davis, B.H.; Borges, L.E.P.; Noronha, F.B. Hydrodeoxygenation of Phenol over Niobia Supported Pd Catalyst. *Catal Today* **2018**, *302*, 115–124, doi:10.1016/j.cattod.2017.03.034.

65. Wang, H.; Male, J.; Wang, Y. Recent Advances in Hydrotreating of Pyrolysis Bio-Oil and Its Oxygen-Containing Model Compounds. *ACS Catal* **2013**, *3*, 1047–1070, doi:10.1021/cs400069z.

66. Bui, V.N.; Toussaint, G.; Laurenti, D.; Mirodatos, C.; Geantet, C. Co-Processing of Pyrolisis Bio Oils and Gas Oil for New Generation of Bio-Fuels: Hydrodeoxygenation of Guaïacol and SRGO Mixed Feed. *Catal Today* **2009**, *143*, 172–178, doi:10.1016/j.cattod.2008.11.024.

67. Saidi, M.; Samimi, F.; Karimipourfard, D.; Nimmanwudipong, T.; Gates, B.C.; Rahimpour, M.R. Upgrading of Lignin-Derived Bio-Oils by Catalytic Hydrodeoxygenation. *Energy Environ Sci* **2014**, *7*, 103–129, doi:10.1039/c3ee43081b.

68. Bykova, M.V.; Ermakov, D.Yu.; Kaichev, V.V.; Bulavchenko, O.A.; Saraev, A.A.; Lebedev, M.Yu.; Yakovlev, V.A. Ni-Based Sol–Gel Catalysts as Promising Systems for Crude Bio-Oil Upgrading: Guaiacol Hydrodeoxygenation Study. *Appl Catal B* **2012**, *113–114*, 296–307, doi:10.1016/j.apcatb.2011.11.051.

69. Gao, D.; Xiao, Y.; Varma, A. Guaiacol Hydrodeoxygenation over Platinum Catalyst: Reaction Pathways and Kinetics. *Ind Eng Chem Res* **2015**, *54*, 10638–10644, doi:10.1021/acs.iecr.5b02940.

70. Silva, N.K.G.; Ferreira, R.A.R.; Ribas, R.M.; Monteiro, R.S.; Barrozo, M.A.S.; Soares, R.R. Gas-Phase Hydrodeoxygenation (HDO) of Guaiacol over Pt/Al2O3 Catalyst Promoted by Nb2O5. *Fuel* **2021**, *287*, doi:10.1016/j.fuel.2020.119509.

71. Xu, Y.; Wang, W.; Liu, B.; Pan, Y.; Dong, B.; Li, Y.; Li, Y.; Guo, H.; Chai, Y.; Liu, C. The Role of Nb2O5 in Controlling Metal-Acid Sites of CoMoS/γ-Al2O3 Catalyst for the Enhanced Hydrodeoxygenation of Guaiacol into Hydrocarbons. *J Catal* **2022**, *407*, 19–28, doi:10.1016/j.jcat.2022.01.027.

72. He, Y.; Bie, Y.; Lehtonen, J.; Liu, R.; Cai, J. Hydrodeoxygenation of Guaiacol as a Model Compound of Lignin-Derived Pyrolysis Bio-Oil over Zirconia-Supported Rh Catalyst: Process Optimization and Reaction Kinetics. *Fuel* **2019**, *239*, 1015–1027, doi:10.1016/j.fuel.2018.11.103.

73. Li, W.; Wang, H.; Wu, X.; Betancourt, L.E.; Tu, C.; Liao, M.; Cui, X.; Li, F.; Zheng, J.; Li, R. Ni/Hierarchical ZSM-5 Zeolites as Promising Systems for Phenolic Bio-Oil Upgrading: Guaiacol Hydrodeoxygenation. *Fuel* **2020**, *274*, 117859, doi:10.1016/j.fuel.2020.117859.

74. Hita, I.; Sarathy, S.M.; Castaño, P. Polymeric Waste Valorization at a Crossroads: Ten Ways to Bridge the Research on Model and Complex/Real Feedstock. *Green Chemistry* **2021**, *23*, 4656–4664, doi:10.1039/D1GC00845E.

75. Mishra, R.K.; kumar, V.; Kumar, P.; Mohanty, K. Hydrothermal Liquefaction of Biomass for Bio-Crude Production: A Review on Feedstocks, Chemical Compositions, Operating Parameters, Reaction Kinetics, Techno-Economic Study, and Life Cycle Assessment. *Fuel* 2022, *316*.

76. Bu, Q.; Lei, H.; Zacher, A.H.; Wang, L.; Ren, S.; Liang, J.; Wei, Y.; Liu, Y.; Tang, J.; Zhang, Q.; et al. A Review of Catalytic Hydrodeoxygenation of Lignin-Derived Phenols from Biomass Pyrolysis. *Bioresour Technol* 2012, *124*, 470–477.

77. Olcese, R.N.; Bettahar, M.; Petitjean, D.; Malaman, B.; Giovanella, F.; Dufour, A. Gas-Phase Hydrodeoxygenation of Guaiacol over Fe/SiO 2 Catalyst. *Appl Catal B* **2012**, *115–116*, 63–73, doi:10.1016/j.apcatb.2011.12.005.

78. Grunwaldt, J.; Dahmen, N. Upgrading Fast Pyrolysis Bio-Oil. **2019**.

79. Shao, Y.; Xia, Q.; Liu, X.; Lu, G.; Wang, Y. Pd/Nb2O5/SiO2 Catalyst for the Direct Hydrodeoxygenation of Biomass-Related Compounds to Liquid Alkanes under Mild Conditions. *ChemSusChem* **2015**, *8*, 1761–1767, doi:10.1002/cssc.201500053.

80. Wang, X.; Zhu, S.; Wang, S.; He, Y.; Liu, Y.; Wang, J.; Fan, W.; Lv, Y. Low Temperature Hydrodeoxygenation of Guaiacol into Cyclohexane over Ni/SiO 2 Catalyst Combined with Hβ Zeolite. *RSC Adv* **2019**, *9*, 3868–3876, doi:10.1039/c8ra09972c.

81. Zhou, M.; Ye, J.; Liu, P.; Xu, J.; Jiang, J. Water-Assisted Selective Hydrodeoxygenation of Guaiacol to Cyclohexanol over Supported Ni and Co Bimetallic Catalysts. *ACS Sustain Chem Eng* **2017**, *5*, 8824–8835, doi:10.1021/acssuschemeng.7b01615.

82. Ambursa, M.M.; Juan, J.C.; Yahaya, Y.; Taufiq-Yap, Y.H.; Lin, Y.C.; Lee, H.V. A Review on Catalytic Hydrodeoxygenation of Lignin to Transportation Fuels by Using Nickel-Based Catalysts. *Renewable and Sustainable Energy Reviews* **2021**, *138*, 110667, doi:10.1016/j.rser.2020.110667.

83. López, M.; Palacio, R.; Royer, S.; Mamede, A.S.; Fernández, J.J. Mesostructured CMK-3 Carbon Supported Ni–ZrO2 as Catalysts for the Hydrodeoxygenation of Guaiacol. *Microporous and Mesoporous Materials* **2020**, *292*, 109694, doi:10.1016/j.micromeso.2019.109694.

84. Yang, Y.; Hao, J.; Lv, G. Comparative Study of Catalytic Hydrodeoxygenation Performance over SBA-15 and TiO2 Supported 20 wt% Ni for Bio-Oil Upgrading. *Fuel* **2019**, *253*, 630–636, doi:10.1016/j.fuel.2019.05.060.

85. Shu, R.; Xu, Y.; Ma, L.; Zhang, Q.; Chen, P.; Wang, T. Synergistic Effects of Highly Active Ni and Acid Site on the Hydrodeoxygenation of Syringol. *Catal Commun* **2017**, *91*, 1–5, doi:10.1016/j.catcom.2016.12.006.

86. Song, W.; Liu, Y.; Baráth, E.; Zhao, C.; Lercher, J.A. Synergistic Effects of Ni and Acid Sites for Hydrogenation and C-O Bond Cleavage of Substituted Phenols. *Green Chemistry* **2015**, *17*, 1204–1218, doi:10.1039/c4gc01798f.

87. Fang, H.; Zheng, J.; Luo, X.; Du, J.; Roldan, A.; Leoni, S.; Yuan, Y. Product Tunable Behavior of Carbon Nanotubes-Supported Ni–Fe Catalysts for Guaiacol Hydrodeoxygenation. *Appl Catal A Gen* **2017**, *529*, 20–31, doi:10.1016/j.apcata.2016.10.011.

88. Xin, H.; Yang, H.; Lei, X.; Du, X.; Zhou, K.; Li, D.; Hu, C. Ni–Fe Catalysts Supported on γ-Al 2 O 3 /HZSM-5 for Transformation of Palmitic Acid into Hydrocarbon Fuel. *Ind Eng Chem Res* **2020**, *59*, 17373–17386, doi:10.1021/acs.iecr.0c01937.

89. Singh, C.; Goyal, A.; Singhal, S. Nickel-Doped Cobalt Ferrite Nanoparticles: Efficient Catalysts for the Reduction of Nitroaromatic Compounds and Photo-Oxidative Degradation of Toxic Dyes. *Nanoscale* **2014**, *6*, 7959–7970, doi:10.1039/c4nr01730g.

90. Duan, H.; Dong, J.; Gu, X.; Peng, Y.-K.; Chen, W.; Issariyakul, T.; Myers, W.K.; Li, M.-J.; Yi, N.; Kilpatrick, A.F.R.; et al. Hydrodeoxygenation of Water-Insoluble Bio-Oil to Alkanes Using a Highly Dispersed Pd–Mo Catalyst. *Nat Commun* **2017**, *8*, 591, doi:10.1038/s41467-017-00596-3.

91. Poole, O.; Alharbi, K.; Belic, D.; Kozhevnikova, E.F.; Kozhevnikov, I. V. Hydrodeoxygenation of 3-Pentanone over Bifunctional Pt-Heteropoly Acid Catalyst in the Gas Phase: Enhancing Effect of Gold. *Appl Catal B* **2017**, *202*, 446–453, doi:10.1016/j.apcatb.2016.09.044.

92. Lee, J.H.; Do, L.T.; Eun, J.; Choi, J.; Suh, D.J.; Choi, J. Deactivation-Free Continuous Production of Bio-Aviation Fuel from Biomass Pyrolysis Oil Using La-Ti-Ce-Ni Perovskite-Derived Catalysts. **2020**, *4390*, 4390.

93. Ballesteros-Plata, D.; Barroso-Martín, I.; Medina Cervantes, J.A.; Maciel, C.; Huirache-Acuña, R.; Rodríguez-Castellón, E.; Infantes-Molina, A. Bimetallic Niobium-Based Catalysts Supported on SBA-15 for Hydrodeoxygenation of Anisole. *Ind Eng Chem Res* **2021**, *60*, 18831–18840, doi:10.1021/acs.iecr.1c02799.

94. Zhu, Y.; Zhang, Z.; Cheng, J.; Guo, H.; Yang, W. Ni-BTC Metal-Organic Framework Loaded on MCM-41 to Promote Hydrodeoxygenation and Hydrocracking in Jet Biofuel Production. *Int J Hydrogen Energy* **2021**, *46*, 3898–3908, doi:10.1016/j.ijhydene.2020.10.216.

95. Arun, N.; Nanda, S.; Hu, Y.; Dalai, A.K. Hydrodeoxygenation of Oleic Acid Using γ-Al2O3 Supported Transition Metallic Catalyst Systems: Insight into the Development of Novel FeCu/γ-Al2O3 Catalyst. *Molecular Catalysis* **2022**, *523*, 111526, doi:10.1016/j.mcat.2021.111526.

96. Schäfer, H.; Gruehn, R.; Schulte, F. The Modifications of Niobium Pentoxide. *Angewandte Chemie International Edition in English* **1966**, *5*, 40–52, doi:10.1002/anie.196600401.

97. Ko, E.I.; Weissman, J.G. Structures of Niobium Pentoxide and Their Implications on Chemical Behavior. *Catal Today* **1990**, *8*, 27–36, doi:10.1016/0920-5861(90)87005-N.

98. Nico, C.; Monteiro, T.; Graça, M.P.F. Niobium Oxides and Niobates Physical Properties: Review and Prospects. *Prog Mater Sci* **2016**, *80*, 1–37, doi:10.1016/j.pmatsci.2016.02.001.

99. Campos Fraga, M.M.; Vogt, J.; Lacerda de Oliveira Campos, B.; Schmitt, C.C.; Raffelt, K.; Dahmen, N. Investigation of Nb2O5 and Its Polymorphs as Catalyst Supports for Pyrolysis Oil Upgrading through Hydrodeoxygenation. *Energy and Fuels* **2023**, doi:10.1021/acs.energyfuels.3c01152.

100. Zhang, Z.; Xu, H.; Li, H. Insights into the Catalytic Performance of Ni/Nb2O5 Catalysts for Vanillin Hydrodeoxygenation in Aqueous Phase: The Role of Nb2O5 Crystal Structures. *Fuel* **2022**, *324*, 124400, doi:10.1016/j.fuel.2022.124400.

101. Ma, D.; Lu, S.; Liu, X.; Guo, Y.; Wang, Y. Depolymerization and Hydrodeoxygenation of Lignin to Aromatic Hydrocarbons with a Ru Catalyst on a Variety of Nb-Based Supports. *Chinese Journal of Catalysis* **2019**, *40*, 609–617, doi:10.1016/S1872-2067(19)63317-6.

102. Campos Fraga, M.M.; Lacerda de Oliveira Campos, B.; Hendrawidjaja, H.; Carriel Schmitt, C.; Raffelt, K.; Dahmen, N. Fast Pyrolysis Oil Upgrading via HDO with Fe-Promoted Nb2 O5-Supported Pd-Based Catalysts. *Energies (Basel)* **2022**, *15*, doi:10.3390/en15134762.

103. Vasconcelos, Y. The Niobium Controversy. *Revista pesquisa FAPESP* **2019**, 1–8.

104. Patterson, A.L. *The Scherrer Formula for I-Ray Particle Size Determination*; 1939; Vol. 56;.

105. Schmal, M.; Vargas, D.C. *Spectroscopy in the Infrared Region*; 2016; ISBN 9783319092492.

106. Boscagli, C.; Tomasi Morgano, M.; Raffelt, K.; Leibold, H.; Grunwaldt, J.D. Influence of Feedstock, Catalyst, Pyrolysis and Hydrotreatment Temperature on the Composition of Upgraded Oils from Intermediate Pyrolysis. *Biomass Bioenergy* **2018**, *116*, 236–248, doi:10.1016/j.biombioe.2018.06.022.

107. Li, C.; Chen, Y.W. Temperature-Programmed-Reduction Studies of Nickel Oxide/Alumina Catalysts: Effects of the Preparation Method. *Thermochim Acta* **1995**, *256*, 457–465, doi:10.1016/0040-6031(94)02177-P.

108. Cai, Z.; Wang, F.; Zhang, X.; Ahishakiye, R.; Xie, Y.; Shen, Y. Selective Hydrodeoxygenation of Guaiacol to Phenolics over Activated Carbon Supported Molybdenum Catalysts. *Molecular Catalysis* **2017**, *441*, 28–34, doi:10.1016/j.mcat.2017.07.024.

109. Boscagli, C.; Raffelt, K.; Zevaco, T.A.; Olbrich, W.; Otto, T.N.; Sauer, J.; Grunwaldt, J.D. Mild Hydrotreatment of the Light Fraction of Fast-Pyrolysis Oil Produced from Straw over Nickel-Based Catalysts. *Biomass Bioenergy* **2015**, *83*, 525–538, doi:10.1016/j.biombioe.2015.11.003.

110. Channiwala, S.A.; Parikh, P.P. *A Uni®ed Correlation for Estimating HHV of Solid, Liquid and Gaseous Fuels q*;

111. Saito, T.; Nakaie, S.; Kinoshita, M.; Ihara, T.; Kinugasa, S.; Nomura, A.; Maeda, T. Practical Guide for Accurate Quantitative Solution State NMR Analysis. *Metrologia* **2004**, *41*, 213–218, doi:10.1088/0026-1394/41/3/015.

112. Mullen, C.A.; Strahan, G.D.; Boateng, A.A. Characterization of Various Fast-Pyrolysis Bio-Oils by NMR Spectroscopy. *Energy and Fuels* **2009**, *23*, 2707–2718, doi:10.1021/ef801048b.

113. Jin, S.; Guan, W.; Tsang, C.W.; Yan, D.Y.S.; Chan, C.Y.; Liang, C. Enhanced Hydroconversion of Lignin-Derived Oxygen-Containing Compounds Over Bulk Nickel Catalysts Though Nb2O5 Modification. *Catal Letters* **2017**, *147*, 2215–2224, doi:10.1007/s10562-017-2085-6.

114. Nie, L.; de Souza, P.M.; Noronha, F.B.; An, W.; Sooknoi, T.; Resasco, D.E. Selective Conversion of M-Cresol to Toluene over Bimetallic Ni–Fe Catalysts. *J Mol Catal A Chem* **2014**, *388–389*, 47–55, doi:10.1016/j.molcata.2013.09.029.

115. Schmal, M.; Vargas, D.C. *Heterogeneous Catalysis and Its Industrial Applications*; 2016; ISBN 9783319092492.

116. Leofanti, G.; Padovan, M.; Tozzola, G.; Venturelli, B. Surface Area and Pore Texture of Catalysts. *Catal Today* **1998**, *41*, 207–219, doi:10.1016/S0920-5861(98)00050-9.

117. Campos Fraga, M.M.; Vogt, J.; Lacerda de Oliveira Campos, B.; Schmitt, C.C.; Raffelt, K.; Dahmen, N. Investigation of Nb2O5 and Its Polymorphs as Catalyst Supports for Pyrolysis Oil Upgrading through Hydrodeoxygenation. *Energy and Fuels* **2023**, *37*, 10474–10492, doi:10.1021/acs.energyfuels.3c01152.

118. Zhang, C.; Wu, J.; Hua, C.; Zhu, L.; Qiu, K.; Wang, S. Hydrodeoxygenation Performance of Lignin-Derived Phenolics to Cycloalkanes: Insights into the Crystal Structures of the Nb 2 O 5 Support. *Energy & Fuels* **2023**, *37*, 14006–14020, doi:10.1021/acs.energyfuels.3c02083.

119. Nayak, P.P.; Datta, A.K. Synthesis of SiO2-Nanoparticles from Rice Husk Ash and Its Comparison with Commercial Amorphous Silica through Material Characterization. *Silicon* **2021**, *13*, 1209–1214, doi:10.1007/s12633-020-00509-y.

120. Gomes, G.H.M.; Mohallem, N.D.S. Insights into the TT-Nb2O5 Crystal Structure Behavior. *Mater Lett* **2022**, *318*, 132136, doi:10.1016/j.matlet.2022.132136.

121. Xu, J.; Zhu, P.; El Azab, I.H.; Bin Xu, B.; Guo, Z.; Elnaggar, A.Y.; Mersal, G.A.M.; Liu, X.; Zhi, Y.; Lin, Z.; et al. An Efficient Bifunctional Ni-Nb2O5 Nanocatalysts for the Hydrodeoxygenation of Anisole. *Chin J Chem Eng* **2022**, *49*, 187–197, doi:10.1016/j.cjche.2022.07.009.

122. Insyani, R.; Kim, M.K.; Choi, J.W.; Yoo, C.J.; Jin Suh, D.; Lee, H.; Soo Kim, C.; Ho Kim, K.; Kim, K.; Ha, J.M. Selective Hydrodeoxygenation of Biomass Pyrolysis Oil and Lignin-Derived Oxygenates to Cyclic Alcohols Using the Bimetallic NiFe Core-Shell Supported on TiO2. *Chemical Engineering Journal* **2022**, *446*, doi:10.1016/j.cej.2022.136578.

123. Jozwiak, W.K.; Kaczmarek, E.; Maniecki, T.P.; Ignaczak, W.; Maniukiewicz, W. Reduction Behavior of Iron Oxides in Hydrogen and Carbon Monoxide Atmospheres. *Appl Catal A Gen* **2007**, *326*, 17–27, doi:10.1016/j.apcata.2007.03.021.

124. Sirikulbodee, P.; Phongaksorn, M.; Sornchamni, T.; Ratana, T.; Tungkamani, S. Effect of Different Iron Phases of Fe/SiO2 Catalyst in CO2 Hydrogenation under Mild Conditions. *Catalysts* **2022**, *12*, 1–19, doi:10.3390/catal12070698.

125. Meng, F.; Zhong, P.; Li, Z.; Cui, X.; Zheng, H. Surface Structure and Catalytic Performance of Ni-Fe Catalyst for Low-Temperature CO Hydrogenation. *J Chem* **2014**, *2014*, doi:10.1155/2014/534842.

126. Zhang, Z.; Xu, H.; Li, H. Insights into the Catalytic Performance of Ni/Nb2O5 Catalysts for Vanillin Hydrodeoxygenation in Aqueous Phase: The Role of Nb2O5 Crystal Structures. *Fuel* **2022**, *324*, 124400, doi:10.1016/j.fuel.2022.124400.

127. Cheng, Z.F.; Wang, F.J.; Yang, W.X.; Zhang, H.Y.; Deng, L.D.; Zhou, G.L.; Zhang, X.M. Study of Bimetallic NiFe Catalysts for Methyl Laurate Hydrogenation. *Ranliao Huaxue Xuebao/Journal of Fuel Chemistry and Technology* **2020**, *48*, 860–866, doi:10.1016/s1872-5813(20)30059-1.

128. Wang, Y.; Zhao, R.; Sun, J. wei; Zhang, K.; Liu, Z. xing; Zhao, Z. wu; Wu, W. fei Mechanistic Study of Ce–La–Fe/γ-Al2O3 Catalyst for Selective Catalytic Reduction of NO with NH3. *Int J Hydrogen Energy* **2022**, *47*, 8261–8274, doi:10.1016/j.ijhydene.2021.12.170.

129. Briggs, D.; Seah, M.P. *Practical Surface Analysis By Auger and X-Ray Photoelectron Spectroscopy.*; Practical Surface Analysis; Wiley, 1983; ISBN 047126279X.

130. Gai, C.; Zhang, F.; Yang, T.; Liu, Z.; Jiao, W.; Peng, N.; Liu, T.; Lang, Q.; Xia, Y. Hydrochar Supported Bimetallic Ni-Fe Nanocatalysts with Tailored Composition, Size and Shape for Improved Biomass Steam Reforming Performance. *Green Chemistry* **2018**, *20*, 2788–2800, doi:10.1039/c8gc00433a.

131. Zhou, J.; An, W.; Wang, Z.; Jia, X. Hydrodeoxygenation of Phenol over Ni-Based Bimetallic Single-Atom Surface Alloys: Mechanism, Kinetics and Descriptor. *Catal Sci Technol* **2019**, *9*, 4314–4326, doi:10.1039/c9cy01082c.

132. Ruban, A. V.; Skriver, H.L.; Nørskov, J.K. Surface Segregation Energies in Transition-Metal Alloys. *Phys Rev B Condens Matter Mater Phys* **1999**, *59*, 15990–16000, doi:10.1103/PhysRevB.59.15990.

133. Shi, D.; Sadier, A.; Girardon, J.S.; Mamede, A.S.; Ciotonea, C.; Marinova, M.; Stievano, L.; Sougrati, M.T.; La Fontaine, C.; Paul, S.; et al. Probing the Core and Surface Composition of Nanoalloy to Rationalize Its Selectivity: Study of Ni-Fe/SiO2 Catalysts for Liquid-Phase Hydrogenation. *Chem Catalysis* **2022**, *2*, 1686–1708, doi:10.1016/j.checat.2022.04.009.

134. Mishra, R.K.; Mohanty, K. Pyrolysis of Manilkara Zapota Seeds over ZSM-5 to Produce High-Quality Bio-Oil and Chemicals. *Fuel* **2020**, *280*, doi:10.1016/j.fuel.2020.118594.

135. Tran, Q.K.; Han, S.; Ly, H.V.; Kim, S.S.; Kim, J. Hydrodeoxygenation of a Bio-Oil Model Compound Derived from Woody Biomass Using Spray-Pyrolysis-Derived Spherical γ-Al2O3-SiO2 Catalysts. *Journal of Industrial and Engineering Chemistry* **2020**, *92*, 243–251, doi:10.1016/j.jiec.2020.09.012.

136. Li, X.; Chen, G.; Liu, C.; Ma, W.; Yan, B.; Zhang, J. Hydrodeoxygenation of Lignin-Derived Bio-Oil Using Molecular Sieves Supported Metal Catalysts: A Critical Review. *Renewable and Sustainable Energy Reviews* **2017**, *71*, 296–308, doi:10.1016/j.rser.2016.12.057.

137. Ojagh, H.; Creaser, D.; Tamm, S.; Hu, C.; Olsson, L. Effect of Thermal Treatment on Hydrogen Uptake and Characteristics of Ni-, Co-, and Mo-Containing Catalysts. *Ind Eng Chem Res* **2015**, *54*, 11511–11524, doi:10.1021/acs.iecr.5b02510.

138. Wan, H.; Chaudhari, R. V.; Subramaniam, B. Catalytic Hydroprocessing of P-Cresol: Metal, Solvent and Mass-Transfer Effects. *Top Catal* **2012**, *55*, 129–139, doi:10.1007/s11244-012-9782-6.

139. Shafaghat, H.; Rezaei, P.S.; Daud, W.M.A.W. Catalytic Hydrodeoxygenation of Simulated Phenolic Bio-Oil to Cycloalkanes and Aromatic Hydrocarbons over Bifunctional Metal/Acid Catalysts of Ni/HBeta, Fe/HBeta and NiFe/HBeta. *Journal of Industrial and Engineering Chemistry* **2016**, *35*, 268–276, doi:10.1016/j.jiec.2016.01.001.

140. Jing, Y.; Wang, Y.; Furukawa, S.; Xia, J.; Sun, C.; Hülsey, M.J.; Wang, H.; Guo, Y.; Liu, X.; Yan, N. Towards the Circular Economy: Converting Aromatic Plastic Waste Back to Arenes over a Ru/Nb2O5 Catalyst. *Angewandte Chemie - International Edition* **2021**, *60*, 5527–5535, doi:10.1002/anie.202011063.

141. Berteau, P.; Delmon, B. *Modified Aluminas : Relationship Between Activity in 1-Butanol Dehydration and Acidity Measured by NH3 TPD*; 1989; Vol. 5;.

142. Cheng, S.; Wei, L.; Julson, J.; Muthukumarappan, K.; Kharel, P.R. Upgrading Pyrolysis Bio-Oil to Hydrocarbon Enriched Biofuel over Bifunctional Fe-Ni/HZSM-5 Catalyst in Supercritical Methanol. *Fuel Processing Technology* **2017**, *167*, 117–126, doi:10.1016/j.fuproc.2017.06.032.

143. Aswin, P.; Sreenavya, A.; Venkatesha, N.J.; Ganesh, V.; Balamurugan, S.; Sakthivel, A. Hydrodeoxygenation of Anisole by Using a Ruthenium-Containing Nickel-Iron Hydrotalcite-Based Catalyst. *ChemistrySelect* **2022**, *7*, doi:10.1002/slct.202202523.

144. Li, L.; Dong, L.; Liu, X.; Guo, Y.; Wang, Y. Selective Production of Ethylbenzene from Lignin Oil over FeOx Modified Ru/Nb2O5 Catalyst. *Appl Catal B* **2020**, *260*, 118143, doi:10.1016/j.apcatb.2019.118143.

145. Jing, Y.; Wang, Y. Catalytic Hydrodeoxygenation of Lignin-Derived Feedstock Into Arenes and Phenolics. *Frontiers in Chemical Engineering* 2020, *2*.

146. Si, Z.; Zhang, X.; Wang, C.; Ma, L.; Dong, R. An Overview on Catalytic Hydrodeoxygenation of Pyrolysis Oil and Its Model Compounds. *Catalysts* **2017**, *7*, 1–22, doi:10.3390/catal7060169.

147. Zhan, J.; Hu, R.; Luo, X.; Zhang, C.; Luo, G.; Fan, J.; Clark, J.H.; Zhang, S. Highly Selective Conversion of Phenol to Cyclohexanol over Ru/Nb2O5-: N C18PA Catalysts with Increased Acidity in a Biphasic System under Mild Conditions. *Green Chemistry* **2022**, *24*, 1152–1164, doi:10.1039/d1gc04046d.

148. Schmitt, C.C.; Zimina, A.; Fam, Y.; Raffelt, K.; Grunwaldt, J.D.; Dahmen, N. Evaluation of High-Loaded Ni-Based Catalysts for Upgrading Fast Pyrolysis Bio-Oil. *Catalysts* **2019**, *9*, doi:10.3390/CATAL9090784.

149. Xu, X.; Zhang, C.; Liu, Y.; Zhai, Y.; Zhang, R. Two-Step Catalytic Hydrodeoxygenation of Fast Pyrolysis Oil to Hydrocarbon Liquid Fuels. *Chemosphere* **2013**, *93*, 652–660, doi:10.1016/j.chemosphere.2013.06.060.

150. Venderbosch, R.H.; Ardiyanti, A.R.; Wildschut, J.; Oasmaa, A.; Heeres, H.J. Stabilization of Biomass-Derived Pyrolysis Oils. *Journal of Chemical Technology and Biotechnology* **2010**, *85*, 674–686, doi:10.1002/jctb.2354.

151. Mishra, R.K.; Jaya Prasanna Kumar, D.; Sankannavar, R.; Binnal, P.; Mohanty, K. Hydro-Deoxygenation of Pyrolytic Oil Derived from Pyrolysis of Lignocellulosic Biomass: A Review. *Fuel* **2024**, *360*, 130473, doi:10.1016/j.fuel.2023.130473.

152. Fisk, C.A.; Morgan, T.; Ji, Y.; Crocker, M.; Crofcheck, C.; Lewis, S.A. Bio-Oil Upgrading over Platinum Catalysts Using in Situ Generated Hydrogen. *Appl Catal A Gen* **2009**, *358*, 150–156, doi:10.1016/j.apcata.2009.02.006.

153. Elliott, D.C. Biofuel from Fast Pyrolysis and Catalytic Hydrodeoxygenation. *Curr Opin Chem Eng* **2015**, *9*, 59–65, doi:10.1016/j.coche.2015.08.008.

154. Schmitt, C.C.; Raffelt, K.; Zimina, A.; Krause, B.; Otto, T.; Rapp, M.; Grunwaldt, J.D.; Dahmen, N. Hydrotreatment of Fast Pyrolysis Bio-Oil Fractions Over Nickel-Based Catalyst. *Top Catal* **2018**, *61*, 1769–1782, doi:10.1007/s11244-018-1009-z.

155. Jongerius, A. *Catalytic Conversion of Lignin for the Production of Aromatics.*; 2013; ISBN 978-90-393-6001-9.

156. Campos Fraga, M.M.; Lacerda de Oliveira Campos, B.; Hendrawidjaja, H.; Carriel Schmitt, C.; Raffelt, K.; Dahmen, N. Fast Pyrolysis Oil Upgrading via HDO with Fe-Promoted Nb2 O5-Supported Pd-Based Catalysts. *Energies (Basel)* **2022**, *15*, doi:10.3390/en15134762.

157. Kim, J.K.; Lee, J.K.; Kang, K.H.; Song, J.C.; Song, I.K. Selective Cleavage of C-O Bond in Benzyl Phenyl Ether to Aromatics over Pd-Fe Bimetallic Catalyst Supported on Ordered Mesoporous Carbon. *Appl Catal A Gen* **2015**, *498*, 142–149, doi:10.1016/j.apcata.2015.03.034.

158. Mehrabadi, B.A.T.; Eskandari, S.; Khan, U.; White, R.D.; Regalbuto, J.R. *A Review of Preparation Methods for Supported Metal Catalysts*; 1st ed.; Elsevier Inc., 2017; Vol. 61;.

159. Komiyama, M. *Design and Preparation of Impregnated Catalysts*; 1985; Vol. 27; ISBN 0161494850806.

160. Bui, H.M.; Großmann, P.F.; Gros, T.; Blum, M.; Berger, A.; Fischer, R.; Szesni, N.; Tonigold, M.; Hinrichsen, O. 3D Printed Co-Precipitated Ni-Al CO2 Methanation Catalysts by Binder Jetting: Fabrication, Characterization and Test in a Single Pellet String Reactor. *Appl Catal A Gen* **2022**, *643*, doi:10.1016/j.apcata.2022.118760.

161. Guo, W.; Tong, T.; Liu, X.; Guo, Y.; Wang, Y. Morphology-Tuned Activity of Ru/Nb2O5 Catalysts for Ketone Reductive Amination. *ChemCatChem* **2019**, *11*, 4130–4138, doi:10.1002/cctc.201900335.

162. Porta, A.; Falbo, L.; Visconti, C.G.; Lietti, L.; Bassano, C.; Deiana, P. Synthesis of Ru-Based Catalysts for CO2 Methanation and Experimental Assessment of Intraporous Transport Limitations. *Catal Today* **2020**, *343*, 38–47, doi:10.1016/j.cattod.2019.01.042.

APPENDIX 1

Calibration Curve for Liquid Products Quantification - Agilent GC 7820A (Karlsruhe Institute of Technology - Germany)

The quantitative chemical compositions of feedstock samples, upgraded oil, and products from guaiacol hydrodeoxygenation (HDO) reactions, as detailed in Chapters 5 and 6, were analyzed using gas chromatography. An Agilent 7820A (Figure 39) gas chromatograph equipped with an Rxi®5Sil MS capillary column (0.25µm film thickness, 0.25 mm internal diameter, 30m length) and a flame ionization detector (FID) was utilized for quantitative analyses. The injection port was maintained at a temperature of 280 ℃, and helium was used as the carrier gas with a flow rate set at 1.5 mL . min^{-1}. The thermal program began with an initial oven temperature of 35 ℃, held for 2 minutes, followed by a first ramp at 8 ℃ . min^{-1} up to 240 ℃. Subsequently, the ramp rate was reduced to 4 ℃ . min^{-1} until the oven temperature reached 280 ℃, where it was held for 15 minutes to complete the analysis.

FIGURE 39. Agilent 7820A

Quantification of the liquid products was carried out using the external standard method, with tetrahydrofuran (THF) as the solvent to prepare the standard mixtures. The analysis focused on a spectrum of key compounds, including cyclohexanone, benzene, cyclohexane, anisole, cyclohexanol, veratrole, phenol, 4-methylguaiacol, 3-methoxycatechol, 4-ethylguaiacol, 2-methyl-2-cyclopenten-1-one, and methanol. These

analytical standards, sourced from Sigma-Aldrich, boast a purity of 99.9%, ensuring the reliability and accuracy of the quantification process.

The calibration process was carried out by first manually preparing a mixture from the standard solutions, followed by its subsequent dilution to create six distinct concentrations. Utilizing Agilent OpenLab CDS software, the prepared standard solutions underwent chromatographic analysis, with the results being subjected to a linear correlation assessment between the concentration of each compound and the corresponding detector response (area). The retention time are reported in Table 18

Illustrating the calibration procedure, the Figure 40 presents the calibration curve for methanol, exemplifying the analytical precision of the Agilent 7820A gas chromatograph. The curve was derived from the linear correlation between the known concentrations of methanol in the prepared standard solutions and their corresponding detector responses, measured as peak areas. Each point on the curve corresponds to a distinct concentration from the series of dilutions, enabling the software to generate a report detailing the concentrations of each compound found, expressed in milligrams per liter (mg . L^{-1}).

FIGURE 40. Calibration curve of methanol obtained from the Agilent 7820A.

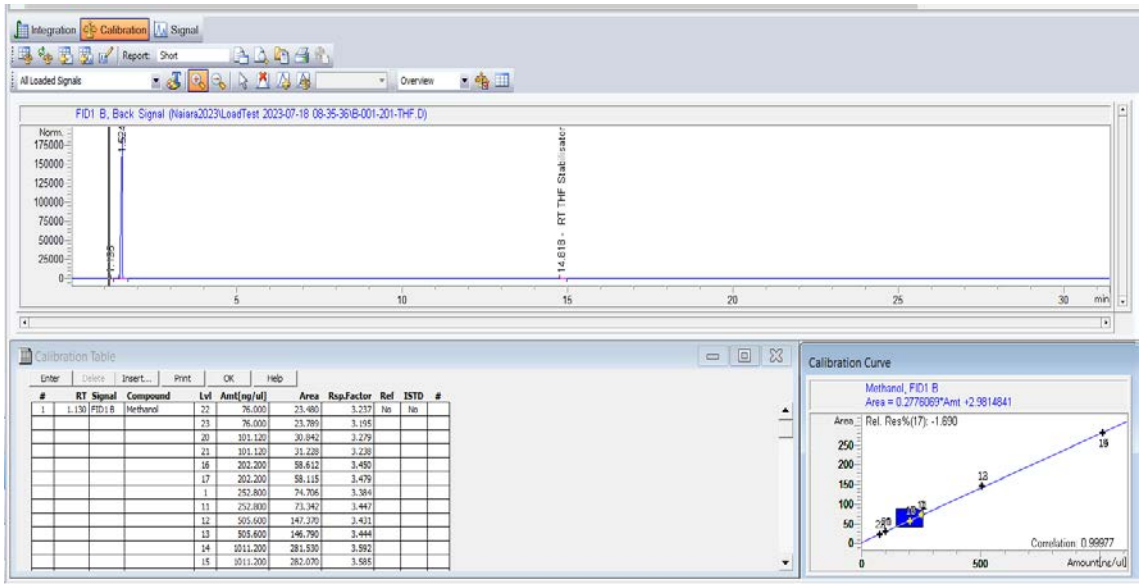

TABLE 18. Retention time, response factor, and detection limit of the calibrated liquid products.

Product	Retention Time
Methanol	1.150
Cyclohexanone	1.622
Benzene	2.685
Cyclohexane	6.676
Anisole	7.433
Guaiacol	7.755
Cyclohexanol	8.394
4-Methylguaiacol	9.605
Catechol	9.714
3-Methoxycatechol	10.76
Veratrole	14.184
Phenol	16.813

Calibration Methodology for gaseous products - Agilent 6890 FID/TCD (Karlsruhe Institute of Technology - Germany)

The quantitative chemical compositions of gaseous products of the hydrodeoxygenation (HDO) reactions, as detailed in Chapters 5 and 6, were analyzed using gas chromatography Figure 41

FIGURE 41 AGILENT 6890 FID/TCD

For calibration a certified gas mix containing H_2, CO, CO_2, CH_4 was purchased. Calibration was performed via manual injection, using syringes of various volumes: 500µl, 250µl, 100µl, 50µl, and 25µl. For each volume, three readings were taken to

ensure accuracy, the retention times are reported in Table 19 The injections were then analyzed chromatographically using Agilent OpenLab CDS software, which assessed the linear correlation between the concentrations of the compounds and their respective detector responses, indicated by the peak areas. Each data point on the resulting calibration curve represents a unique concentration from the dilution series. This process allows the software to accurately generate a report that specifies the concentrations of each compound, expressed as a volume percentage of gas (%v/v).

TABLE 19. Retention time and detector of the calibrated gaseous products.

Product	Detector	Retention Time
CH_4	FID	11.983
H_2	TCD	5.081
CO	TCD	12.345
CO_2	TCD	2.861

APPENDIX 2

DETAILED CHEMICAL COMPOSITION FROM GC-MS MEASUREMENTS GCMS

The chromatograms for the aqueous phases (ap), upgraded oils (hp), and feedstock are presented in figures 1 from a to g, while table 1 compiles the retention times of the principal compounds identified. By comparing the GC-MS data of the upgraded products with the feedstock, we can monitor the consumption or production of specific compounds and gain an initial understanding of the variations in their concentrations.

TABLE 20. Single compounds identified by gc-ms in the upgraded oils and feedstocks.

Retention Time	Chemical Compound	Retention Time	Chemical Compound
2.68	Formaldehyde	18.09	3-Methyl-4-hexyn-3-ol
2.76	Methanol	18.12	5-(Hydroxymethyl) dihydrofuran-2(3H)-one
2.79	Methyl Alcohol	18.21	1,2-Benzenediol, mono(methylcarbamate)
2.99	Ethanol	18.22	4-Methylguaiacol
3.17	Hydrogen isocyanate	18.23	1,3-Benzenediol, o-butoxycarbonyl-
3.24	Acetic acid, methyl ester	18.24	5-Amino-2-methoxyphenol
4.84	2-Propanone, 1-hydroxy-	18.43	1,3,2-Dioxaborolane-4,5-dimethanol, 2-ethyl-

			, diacetate, (4S-trans) -
4.84	Acetic acid, methoxy-, methyl ester	18.66	4-Hexen-3-one
5.61	1,2-Ethanediol	19.09	4-Chlorobutyric acid, 4-isopropylphenyl ester
5.67	2-Amino-2-methyl-1,3-propanediol	19.19	Cyclohexane, 1-bromo-3-methyl-
5.97	Acetoin	19.23	2(5H) -Furanone, 5,5-dimethyl-
5.97	Acetic acid, (acetyloxy)-	19.57	Ethanone, 1-(2,5-dihydroxyphenyl) -
7.73	Boronic acid, ethyl-	19.75	Ethyne, fluoro-
7.74	1-Hydroxy-2-butanone	19.82	4-Ethylguaiacol
8.15	Succindialdehyde	19.85	N-Hydroxy-1,5-dimethyl-1H-pyrrole-2-carboxamidine
8.42	1-Penten-3-one	19.85	Resorcinol, 2-acetyl-
8.7	Propane, 1,2-dimethoxy-	19.94	2-Methylpropanoic acid, TMS derivative
8.94	2-Hydroxy-3-pentanone	19.96	3-(1-Methylpropyl) -2-hydroxy-2-cyclopenten-1-one
9.69	Furfural	20.02	N-Ethylbenzimidoyl chloride

9.78	1-Azabicyclo [3.1.0] hexane	20.23	Stearic acid, TBDMS derivative
9.96	Proline, 2-methyl-5-oxo-, methyl ester	20.42	Propane, 2-ethoxy-
9.96	2-Cyclopenten-1-one, 2-hydroxy-	21.21	Phenol, 2-methoxy-4-(2-propenyl) -, acetate
10.19	2-Hydroxyethylacetate	21.24	4-Vinylbenzoic acid
10.91	1,3-Dioxolane-2-methanol	21.39	2-Methoxy-4-Propylphenol
10.97	Propanoic acid, 2-hydroxy-, propyl ester	21.42	Acetic acid, (4-aminophenoxy) -
11.45	2-Hydroxy-3-hexanone	21.55	Beta.-D-Glucopyranose, 1,6-anhydro-
11.52	4-Hydroxy-3-hexanone	21.55	Propanamide
11.71	Cyclohexane, 1-bromo-4-methyl-	21.87	3-Ethyl-2-nonanone
11.73	2-Methyl-2-cyclopenten-1-on	21.9	Acetamide, N-[(4-methoxyphenyl) methyl]-
11.84	Cyclopentanon	21.97	Vanillin
11.85	1-(1'-pyrrolidinyl) -2-butanone	22.01	3(2H) -Furanone, 4-hydroxy-5-methyl-
11.86	2-Propenoic acid, 2-methyl-	22.39	3-(Benzo(b)thien-6-yl) propionic acid
11.87	(S)-4-Ethyl-2-oxazolidone	22.42	Butanedioic acid, methoxy-, dimethyl ester

11.88	Butanoic acid, 4-hydroxy-	22.51	Alanine, N-methyl-N-methoxycarbonyl-, undecyl ester
12.09	Butane, 2,3-dimethyl-	22.69	Beta.-D-Glucopyranose, 1,6-anhydro-
12.33	2,5-Hexanedione	22.69	n-Propyl heptyl ether
12.91	1,3-Dioxolan-2-one, 4,5-bis(methylene)-	22.81	Phenol, 2-methoxy-4-(1-propenyl) -, acetate
13.54	1-Penten-3-one, 2-methyl-	22.95	2,8-Dihydroxyquinoline, bis(2-methylpropionate)
13.65	2,3-Pentanedione	23.15	Glycine, N-(2-fluorobenzoyl) -, propyl ester
13.66	Carbonochloridic acid, 2-chloroethyl ester	23.21	3,6-Dimethyl-4H-furo[3,2-c] pyran-4-one
13.67	Phenol	23.37	Ethanone, 1-(3-hydroxy-4-methoxyphenyl) -
13.77	5-Hydroxy-7-methoxy-2-methyl-3-phenyl-4-chromenone	23.39	1,4-Pentadiene, 3-ethenyl-
13.88	anti-2-Acetoxyacetaldoxime	23.41	Methane, isocyanato-

13.99	1-Pentanone, 1-(2-furanyl) -	23.41	Acetone cyanohydrin
14.08	1-Propoxy-3,3-diethyltriazene 2-oxide	23.69	Butylhydroxytoluol
14.1	2-Propanone, 1,1,1-trifluoro-	23.92	D-Mannitol
14.68	2-Hydroxy-3-methyl-2-cyclopentenon	24	Propan-2-one, 1-(4-isopropoxy-3-methoxyphenyl) -
15.13	Fumaric acid, monoamide, N, N-dimethyl-, 2-fluorophenyl ester	24.03	2-Propanone, 1-(4-hydroxy-3-methoxyphenyl) -
15.22	Butanoic acid, 2-oxo-, methyl ester	24.03	3-Propoxy-benzoic acid
15.53	Propanoic acid, 2-methyl-, anhydride	25.19	Homosyringaldehyde
15.55	Dithiocarbamic acid, N, N-dimethyl-, S-dimethylamino ester	25.46	3,4-Diethoxybenzaldehyde
15.64	Naphthalene, decahydro-	25.5	Thymine
15.86	p-Cresol	25.83	Homovanillic acid
15.89	5,10-Pentadecadienoic acid, (E, Z)	26.29	Benzoic acid, phenyl ester
16.09	1H-Indene-1-methanol, acetate	26.29	Benzene, 1,1'-(1,2-dimethyl-1,2-ethanediyl) bis-
16.11	Guaiacol	26.63	2-Cyano-6-methoxybenzothiazole

16.13	Pyrazine	27.06	2,4(1H,3H) -Pteridinedione, 6-methyl-
16.29	2-Acetoxyacetaldoxime	27.52	Benzeneacetamide, N-(aminocarbonyl)-4-hydroxy-3-methoxy-
16.42	1,2,3-Propanetriol, 1-acetate	27.76	1,2-Oxaphosphole, 3,5-bis(1,1-dimethylethyl) -2,5-dihydro-2-hydroxy-, 2-oxide
17.08	2,4-Dihydroxybenzaldehyde, 2TMS derivative	28.32	2-Acetyl-6-methoxynaphthalene
17.13	(2S,6R,7S,8E) -(+) -2,7-Epoxy-4,8-megastigmadiene	29.44	l-Alanine, N-(2,3,4-trifluorobenzoyl) -, methyl ester
17.3	3,4-Dihydroxybenzaldehyde, diacetate	31.57	4(1H) -Pyridinone, 1,2,6-trimethyl-3,5-diphenyl-
17.62	1H-1,2,3-Triazole	32.81	1,2,4,5-Tetrazin-3-amine, 6-methyl-
		33.16	4H-1-Benzopyran-4-one, 3,5,7-trihydroxy-2-(4-hydroxyphenyl)-6-methoxy-
		34.24	5,6,4'-Trihydroxy-7,8-dimethoxyflavone

	35.53	Benzenamine, 4-methoxy-2-methyl-

FIGURE 42. Qualitative results obtained by gc-ms for the products after upgrading. feedstock: btg light phase bio-oil.

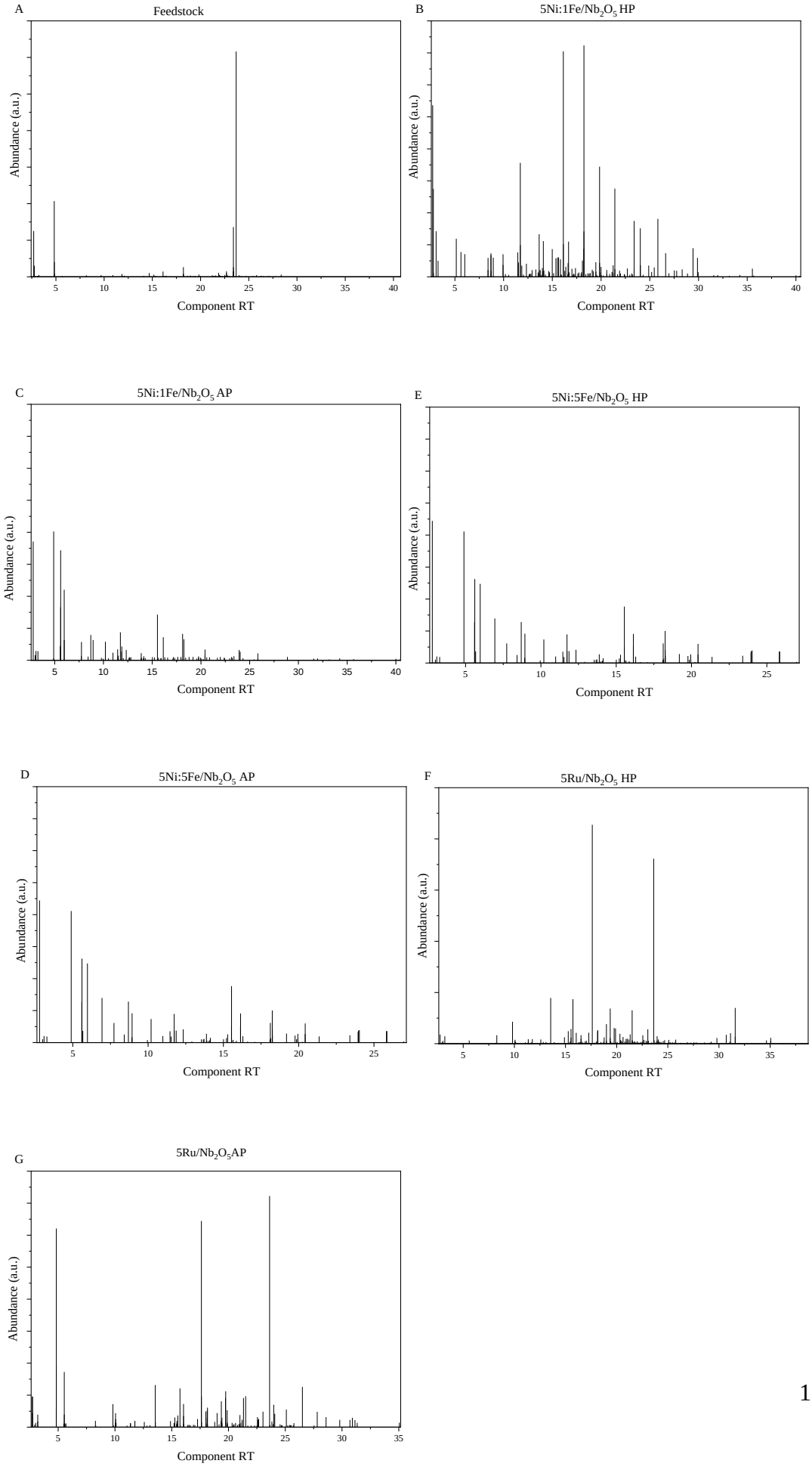
A
Feedstock
B
5Ni:1Fe/Nb2O5 HP
C
5Ni:1Fe/Nb2O5 AP
E
5Ni:5Fe/Nb2O5 HP
D
5Ni:5Fe/Nb2O5 AP
F
5Ru/Nb2O5 HP
G
5Ru/Nb2O5AP
Abundance (a.u.)
Component RT

APPENDIX 3

The UV/VIS spectra of the catalysts

FIGURE 43. DRS-UV–VIS spectra for catalysts supported as a- Nb_2O_5 and b- SiO_2

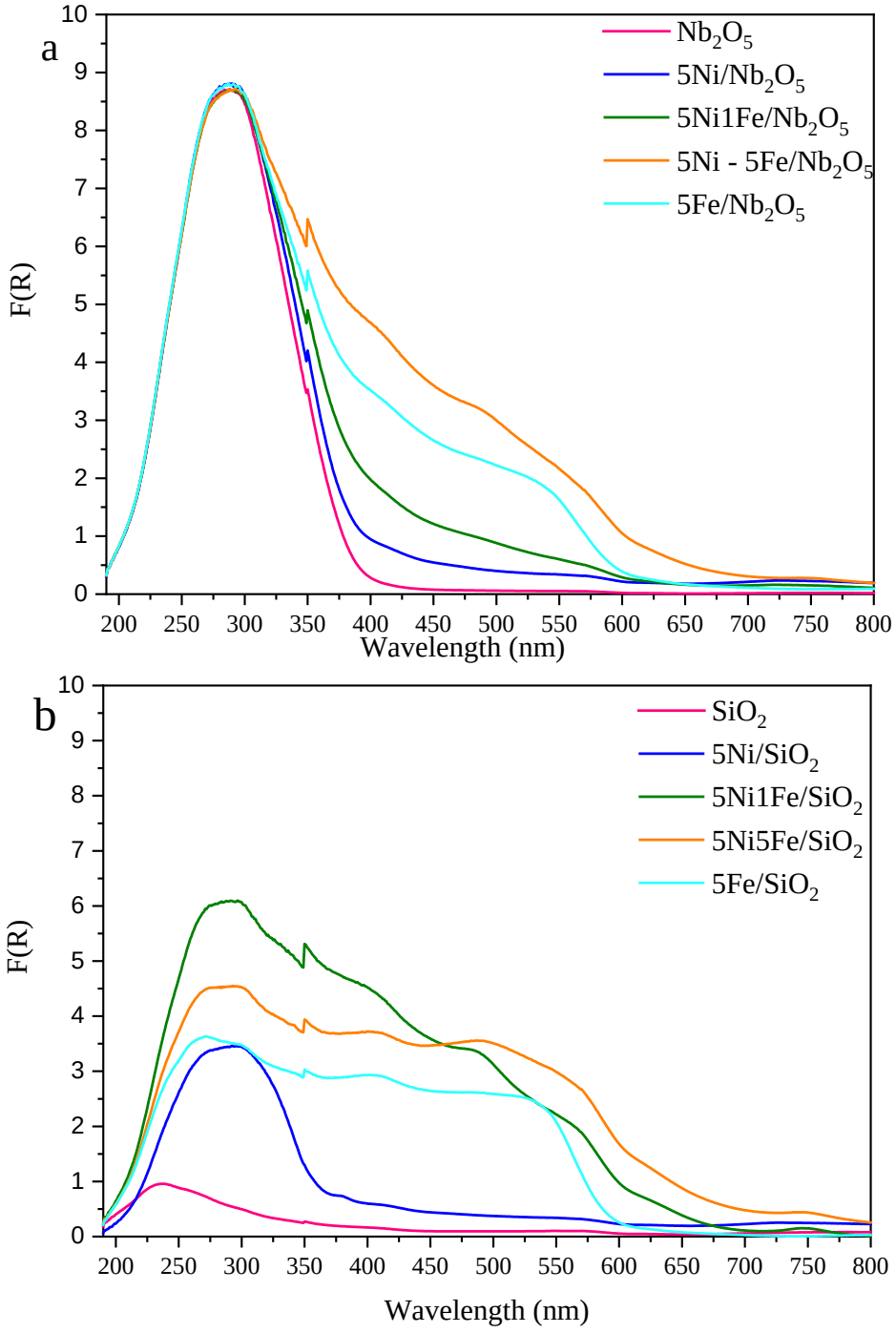

APPENDIX 4

Scientific Contributions Derived from This Thesis

During the development of this doctoral work, the following scientific contributions were made:

Submitted Article

Study of NiFe Catalysts Supported on Nb_2O_5 for Enhanced Hydrodeoxygenation. Submitted to *Topics in Catalysis*.

Conference Presentations and Posters

1- **NAM27 – The 27th North American Catalysis Society Meeting**

Date: 2022 | Location: New York, United States

Presentation: Poster

Title: *Guaiacol Hydrodeoxygenation over Ni-Fe Supported on Nb_2O_5 and SiO_2 Catalysts*

2- **56. Jahrestreffen Deutscher Katalytiker**

Date: 2023 | Location: Weimar, Germany

Presentation: Poster

Title: *Guaiacol Hydrodeoxygenation over Ni-Fe Supported on Nb_2O_5 and SiO_2 Catalysts*

3- **European Biomass Conference and Exhibition – EUBCE**

Date: 2023 | Location: Bologna, Italy

Presentation: Poster

Title: *Performance Evaluation of a Niobium-Based Pellet Catalyst: Hydrodeoxygenation of Bio-Oil in a Trickle Bed Reactor*

4- **NAM28 – The 28th North American Catalysis Society Meeting**

Date: 2023 | Location: Providence, Rhode Island, United States

Presentation: Poster

Title: *Evaluation of Niobium-Based Performance Catalysts in a Continuous Liquid-Phase HDO Reaction*

5- Nordic Symposium on Catalysis (NSC)

Date: 2024 | Location: Sola, Norway

Presentation: Oral

Title: *Niobium Pellets Performance for Scaled-Up Bio-Oil Upgrading*

6- European Biomass Conference and Exhibition – EUBCE

Date: 2024

Presentation: Oral

Title: *Stabilization Step within Hydrotreatment of Fast Pyrolysis Bio-Oil*